FREQUENCY DOMAIN PHOTOCURRENT MEASUREMENT

STUDENT : CHEE CHIANG DERRICK TIEW

STUDENT ID : [redacted]

SUPERVISOR : DR VINEETHA KALAVALLY

CO-SUPERVISOR : A/P YE CHOW KUANG

A thesis submitted for the degree of *Doctor of Philosophy* at

Monash University in 2018

School of Engineering

ABSTRACT

Traditional photocurrent measurement relies on wide-band direct measurement and amplification technique. Such a measurement technique may result in big and complex signal conditioning circuit especially for sensors that produce minute current with high output impedance. The traditional measurement also requires high quality power supply and careful shielding to minimise electromagnetic interference from the surrounding environment. Hence, it becomes costly to perform such measurement for sensors with low charge generation efficiency. In view of this, this research proposes a technique of using the statistical data obtained from the frequency response function (FRF) of a photosensor as an indirect light intensity measurement. The proposed research started with the initial works into the frequency response of the RC photodetector excited by noise utilizing best linear approximation (BLA) measurement methodology. Two excited signals, random phase multisine and Gaussian noise have been applied to activate the measurement circuit. The photocurrent was sourced from miniature solar cell and OPV cells respectively in tandem with different light irradiance from a dimmable LED light bulb. Results show that the standard deviation of the frequency response function (FRF) of the measurement circuit is a monotonic function of the photocurrent. Larger current due to higher light intensity produces wider spread of standard deviations. The correlation is generally valid across all frequency bands but much stronger at certain frequencies. The magnitude of the photocurrent can be deduced with reasonable accuracy by measuring the standard deviation of FRF at selected frequencies without resorting to the use of high-end current measuring instruments. This particular feature may be useful in sensor design because it allows noise sources with stable statistical characteristics to be used in the measurement circuit. The promising result provides hindsight to an indirect method to measure the response of sensors especially those sensors that produce minute electrical signal, thus avoiding environmental interference encountered in wide-band direct current measurement technique. The proposed technique is not limited to optical sensor, the method can be generalized to any sensor that produces electrical signal. The simplicity of the experimental setup and analysis of the proposed BLA measurement circuit suggests that it is possible to miniaturize the measurement circuit such that it can be embedded directly and be built as an integrated part of a particular photosensor. This will provide a complete low-cost solution for light intensity detection, especially for application in "on/off" switch control of electrical appliances.

DECLARATION

This thesis contains no material which has been accepted for the award of any other degree or diploma at any university or equivalent institution and that, to the best of my knowledge and belief. This thesis contains no material previously published or written by another person, except where due reference is made in the text of the thesis.

Signature: 

Print Name: Chee Chiang Derrick Tiew

Date: 1-October-2018

ACKNOWLEDGEMENT

I would like to express my gratitude to all the people who have contributed in one way or another, to make this thesis possible.

First, I would like to thank Dr Vineetha Kalavally for her willingness to take over as my main supervisor half-way through my candidature, and for her unwavering support to guide me through to the completion of my research study.

Second, my sincere thanks and appreciation goes to my supervisor turned co-supervisor, A/P Ye Chow Kuang, for his guidance and technical advice throughout this project. His insightful thoughts have spurred me to always go for extra miles in pursuing my research goals. Without his guidance, the research on this topic wouldn't have reached the current stage.

I would like also to thank many others who in one way or another, have helped me in conducting this research. To Dr Melanie Ooi, thanks for your time in vetting my reports and provided guidance on some of the measurement set-up. To Professor Jussi who helped in formulating my initial research on bacteriorhodopsin photosensors. To Dr Ramakrishnan who facilitated equipment necessary for the fabrication of photosensors. To Mr Hasnan, Mr Suresh and Mr Daniel Wong who arranged the test equipment and laboratory space for me to conduct experiments.

TABLE OF CONTENTS

LIST OF FIGURES

LIST OF TABLES

LIST OF ACRONYMS

CASES

CHAPTER 1 INTRODUCTION

1.1 Background & Motivation

Photocurrent measurement has been important to the design of various light sensing devices. Even though there are numerous light sensing technologies with wide spectrum of different techniques employed, the underlying physical principle of sensing remains the same. The general physical mechanism of light sensing can be summarized as follows: the photon excites certain molecules in the sensing element; in turn, this excitation generates secondary or higher order reaction that creates free flowing electric charges. The movement of the photon-generated electrical charge under an applied electrical field is called photocurrent. The amount of photocurrent is proportionately correlated to the amount of photons or light intensity that the sensing element is exposed to. By measuring and quantifying the photocurrent, the light intensity can be indirectly quantified. Using a spectrally selective sensor, the correlation between photocurrent and the photon intensity can be used to produce a colour sensor [1].

One of the difficulties in measuring the photocurrent is the low conversion efficiency and high output impedance of sensing materials [1], [2], [3]. With the exception of highly optimized solar cells, most photosensitive materials have a relatively low photoelectric conversion efficiency (PCE). The low power density of light and the low PCE generates a very small quantity of free electric charges. Majority of the photosensitive materials are not good conductors; the high impedance removes significant fraction of the free charges before they can be measured by an external measuring circuit. Thus, the amount of photocurrent that can be measured from external circuit is both very small and load dependent. This is an issue because small current measurement is susceptible to exogenous noise. In addition, the high output impedance causes the measurement to be sensitive to minute component drifts in the measurement circuits which significantly affects the overall robustness of the sensor.

Currently, the only solution to overcome this measurement issue is to use material with high PCE. This approach relies on the advancement of material science and nano-fabrication technology, thus making the progress both expensive and highly uncertain. Furthermore, the standard sensor design requires electromagnetic interference (EMI) shielding and low drift, both of which results in a bulky and expensive measurement circuit.

Apart from fine-tuning the sensor layout to minimize the output impedance, there is very little scope of improvement from the engineering design perspective. The effectiveness of layout tuning is also bounded by the choice of sensing material. Therefore, this research aims to develop and propose an engineering solution to the photocurrent measurement problem that is independent of advancement in material science. Instead of drawing photocurrent directly to assess the light intensity, this research proposes to indirectly quantify the light intensity without drawing any significant photocurrent. This will therefore alleviate the problem of low conversion efficiency and high output impedance. The proposed method uses an active excitation signal to probe the sensor. The sensor interacts with the excitation signal through voltage instead of current.

1.2 Research Problem

Traditional photocurrent measurement works on wide-band direct measurement and amplification principle. Such technique may amplify noise coupled into the measurement circuit, require EMI shielding and complex signal conditioning circuitry. This is especially true for sensors with low charge generation capacity and high output impedance. The conventional technique is also costly as it needs top-notch equipment and high quality power supply. Hence, there is a need to find an alternative solution to address the photocurrent measurement problems faced by the optical sensors that produce minute photocurrent. The proposed alternative solution in this research is looking into the frequency domain measurement technique to find a correlation to the direct traditional photocurrent measurement technique. Instead of filtering noise in the measurement, the technique will couple onto an excitation noise source to produce the statistical measurement of nonlinearities present in the measurement circuit as an indirect strength indication of the measured photocurrent.

1.3 Research Objectives

The research aims to develop a frequency domain photocurrent measurement framework, and to prove the feasibility of using the technique as a low-cost solution for detecting light intensity. The research seeks to prove the concept, and the use of such technique in effectively overcoming the problems faced by present measurement technique.

To meet the aims of the research, two objectives are developed as below:

1. To define the frequency domain photocurrent measurement methodology flow
2. To design and construct a measurement circuit board
3. To apply the measurement technique on photocurrent detection

1.4 Research Hypothesis

Photocurrent can be measured using frequency domain statistics based on statistical analysis of any nonlinear systems that can be modelled as Volterra series.. In this case, the standard deviation of frequency response function (FRF) is used as an indirect inference of light intensity. This noise excited measurement is particularly suitable for low power applications and can be generalized to any sensors especially those sensors with high output impedance and produce weak signal. The proposed measurement technique is low cost, does not require high quality power supply and EMI shielding.

1.5 Contributions To Knowledge

The novel measurement technique is based on introduction of noise excitation source to a signal measurement circuit, and statistical computation on the frequency response function (FRF) of the output signal. The proposed research looks into a total solution to the frequency domain photocurrent measurement. The work starts with a three-electrode measurement system where the excitation signal is applied via a different electrode rather than the input electrode for the photocurrent source. The research covers but not limited to the formulation of frequency domain photocurrent methodology flow, the design of the measurement circuit and technique, the statistical signal computation and analysis. The accuracy of the measurement technique is verified through measurement works on few optical sensors, and results compared with those obtained using conventional current amplification method. The standard deviations of FRF are used as an indicator of the strength of the measured physical signal without the needs for high quality dc or ac power supply. This technique allows the examination of sensors with very high output impedance at a fraction of setup cost for expensive equipment.

1.6 Organization of the Report

Chapter 2 contains four sections which form the literature review component of this research. The first section reviews the physics of photocurrent generation. The equivalent circuit models, both static and dynamic models, are discussed in the second section. The photocurrent measurement techniques are then presented in the third section. The fourth section is dedicated to the discussion of nonlinear systems, in particular Volterra systems. This is followed by a section to provide overview of some of the works that have been carried out on Volterra systems over the years. The chapter is wrapped up in final section with a discussion to the various nonlinearity sources present in photocurrent.

Chapter 3 describes the novel methodology framework for frequency domain photocurrent measurement. The chapter starts with the concept of best linear approximation, and the use of this approximation in estimating the variance of photocurrent measurement in frequency domain. The design of the measurement circuit with the use of random phase multisine and Gaussian noise as an excitation source to the measurement circuit is then introduced. A methodology flow chart is presented on the proper procedures to follow for the measurement technique to produce the correct results.

Chapter 4 presents a theoretical investigation into the sources of nonlinearities that give rise to the peaks of standard deviations of frequency response function at certain frequencies. The nonlinearities come from the devices in generating the photocurrent as well as the measurement circuit itself. A Simulink model with the relevant Matlab scripts has been described. This is followed by the presentation of power spectral density plots on the standard deviations based on the simulated frequency response function.

Chapter 5 first describes the experimental set-up of the proposed frequency domain photocurrent. This is followed by the measurement data obtained using miniature photovoltaic cell as a photocurrent source, first with mutltisine and then with Gaussian noise as the excitation signal to the photocurrent. Measurement data with organic photovoltaic cell as the source of photocurrent with Gaussian noise as the excitation signal is then presented. Regression analysis has been carried out on the dominant frequency for each set of experimental data. Analysis on the experimental results were given where necessary to explain the findings.

Chapter 6 is where conclusion is drawn with a summary of works done. Future possible works to be carried out are then briefly highlighted.

Appendix A provides the additional simulation results whereas Appendix B includes additional experimental results not presented in the main body. Appendix C presents the electrical characterisation and fabrication conditions of the fabricated organic photovoltaic devices. Appendix D lists the Matlab scripts for excitation signal generation. Appendix E outlines the various Labview VI programs developed to carry out the experiments and to acquire the experimental data using National Instruments equipment. Matlab scripts to process the experimental data and formatting on the plots are included in Appendix F. Other Matlab scripts for data analysis are shown in Appendix G.

CHAPTER 2 LITERATURE REVIEW

2.1 Background on Photocurrent

Photocurrent is the electric current generated by a photosensitive device such as a photovoltaic cell, photocell, photodiode, etc. upon exposure to light as a result of either photovoltaic, photoconductive or photoemissive effect. The general physical mechanism of light sensing can be summarized as follows: the photon excites certain molecules in the sensing element; in turn, this excitation generates secondary or higher order reaction that creates free flowing electric charges. The movement of the photon-generated electrical charge under an applied electrical field is what constitutes the photocurrent. The photocurrent is directly proportional to intensity of radiation when a suitable radiation is used, and can be further enhanced by internal gain due to the interaction of photons and ions with an applied field. Photocurrent increases with accelerating potential until saturation current is reached at which the generated photocurrent is at maximum and does not increase further with increasing accelerating potential. On the other hand, there is a retarding potential called stopping potential at which no photocurrent is generated for a given frequency of incident light rays as illustrated in Fig. 2-1.

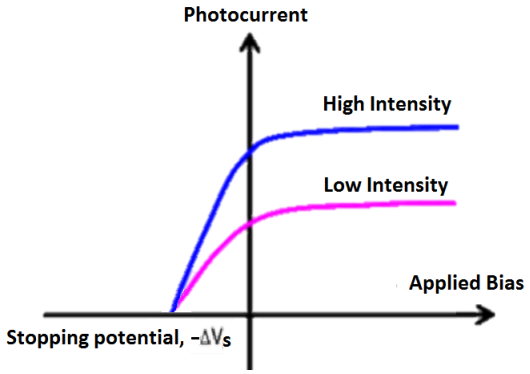

Fig. 2-1. Photocurrent at different applied bias and light intensity

2.1.1 Photovoltaic Effect

For photovoltaic effect to take place, the optical detector must have a region in which majority carriers of the electrical conductivity are holes (i.e. p-type material) in abutment with a region with electrons as the majority carriers (i.e. n-type material) to form a p-n junction. When optical energy strikes the p-n junction, additional electron-hole pairs are thermally generated. The thermally generated holes are then swept to the p-side due to the presence of negatively ionised immobile acceptors at the p-side of space charge region (SCR)

while the thermally generated electrons are swept to the n-side due to the presence of positively ionised immobile donors at the n-side of SCR. These excited carriers subsequently recombine and return to steady state via an external circuit thus producing photocurrent in the return path as illustrated in Fig. 2-2. Photovoltaic current is thus generated as a result of the absorption of photons that creates a voltage difference across a p-n junction, that is the generation of photo voltage.

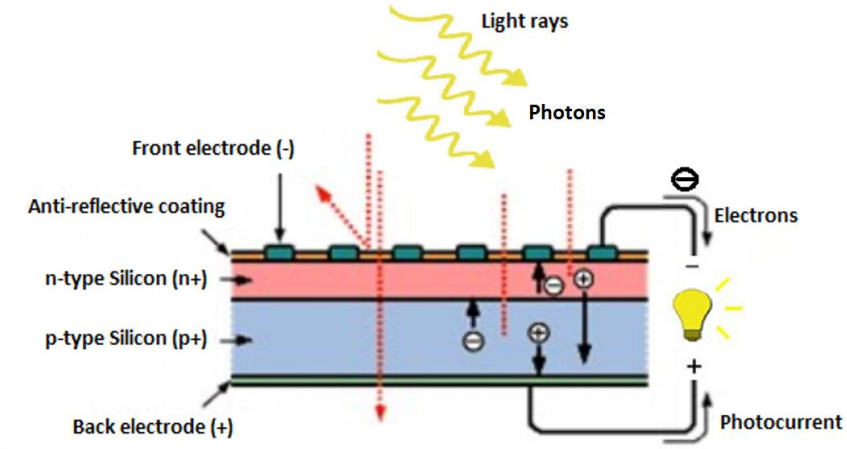

Fig. 2-2. Photocurrent generation via photovoltaic effect

2.1.2 Photoconductive Effect

The electrical conductivity of a photoconductive material changes as a function of the irradiance. Thus, it leads to having increasing electrical conductivity with increasing intensity of the incident light resulting from increasing number of free carriers generated when photons are absorbed as illustrated in Fig. 2-3. An example will be light-dependent resistor (LDR) in which exposure to light reduces / increases the resistance of the material, depending on whether the resistance material is positive or negative correlated with light radiation.

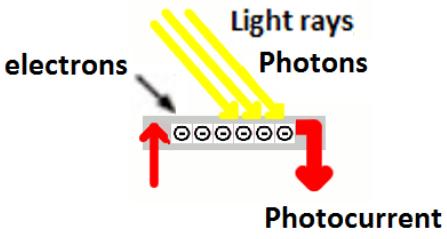

Fig. 2-3. Photocurrent generation via photoconductive effect

2.1.3 Photoemissive Effect

Photoemissive effect occurs when energy supplied by incident light radiation. The incident photons release electrons from the conduction band of usually solid material such as doped silicon as illustrated in Fig. 2-4. A photoemissive cell, sometimes called photocell, emits photoelectrons from its light sensitive surface when photons with sufficient energy are made incident on it.

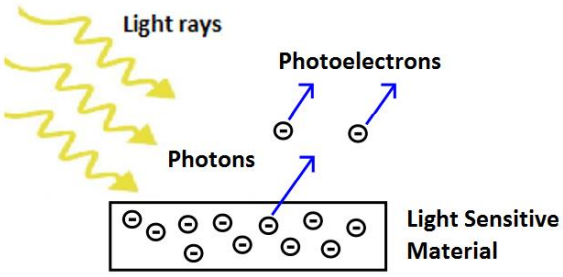

Fig. 2-4. Photocurrent generation via photoemissive effect

2.2 Equivalent Circuit Model of Photovoltaic Cell

2.2.1 Photovoltaic Cell

A photovoltaic (PV) cell is made out of two layers of semiconducting materials which are referred to as the p-type layer and n-type layer. A pn-junction is formed whenever a p-type material is abutted to an n-type material. The doping profile at the junction can take several shapes, with two popular doing profiles being the abrupt junction or linearly graded junction.

2.2.2 Static I-V Characteristics

An equivalent circuit is created for a PV cell to better understand the physical configuration of the elements of the cell as well as the electrical characteristics of each element. Fig. 2-5 shows the conventional static equivalent circuit model without parasitic resistances. Photocurrent source I_{ph} is connected in parallel with the diode. The diode is to model the current-voltage characteristics of the PV cell under dark condition.

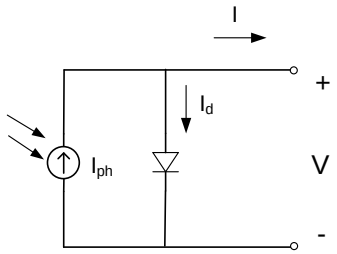

Fig. 2-5. Ideal conventional equivalent circuit model of a PV cell in the absence of parasitic resistances

For this ideal equivalent circuit model, the externally measured current I can be related to photoelectric voltage V through the following expression:

$$I = I_{\text{ph}} - f(V) \tag{2-1}$$

where *f(V)* represents the dark I-V characteristics of PV cell.

$$f(V) = I_d = I_o \cdot (e^{\left(\frac{V}{n \cdot V_T}\right)} - 1) \tag{2-2}$$

where I_o is the diode saturation current, n is the ideality factor, and V_T is the thermal voltage of a PV cell.

Based on this ideal model, short-circuit current I_{sc} is simply equal to I_{ph}, and the open-circuit voltage can be obtained from:

$$f(V_{oc}) = I_{ph} = I_o \cdot (e^{\left(\frac{V_{oc}}{n \cdot V_T}\right)} - 1) \quad \rightarrow \quad V_{oc} = n \cdot V_T \cdot ln(\frac{I_{ph}}{I_o} + 1) \tag{2-3}$$

However, a PV cell is always associated with parasitic resistances. Series resistance R_s accounts for the movement of current through the emitter and base of the PV cell, the contact resistance between the metal contact and the silicon and the resistance of the top and rear metal contacts [2]. On the other hand, shunt resistance R_{sh} is to model the power losses of PV cell due to manufacturing defects. Fig. 2-6 shows the static equivalent circuit model for a PV cell with parasitic series resistance R_s and shunt resistance R_{sh} [3]. Equation (2-2) can then be modified as:

$$I = I_{\text{ph}} - f(V + I \cdot R_s) - \left(\frac{V + I \cdot R_s}{R_{sh}}\right) = I_{\text{ph}} - I_o \cdot (e^{\left(\frac{V + I \cdot R_s}{n \cdot V_T}\right)} - 1) - \left(\frac{V + I \cdot R_s}{R_{sh}}\right) \tag{2-4}$$

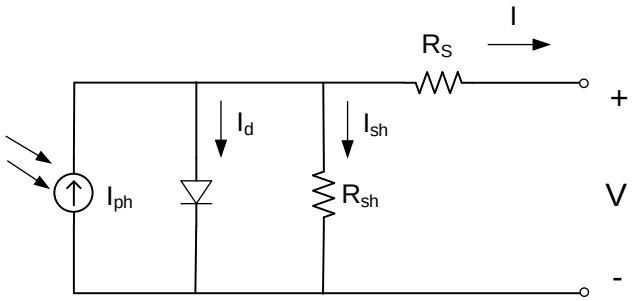

Fig. 2-6. Conventional static equivalent circuit model of a PV cell with a diode, series resistance R_s and shunt resistance R_{sh}

A second diode as shown in Fig. 2-7 can be added to more accurately predicting the performance of the photovoltaic cell at low irradiance levels. Two-diode model is introduced because one-diode model is not able to model the recombination in the junction at lower voltages as the ideality factor *n* approaches close to two [4], [5], [6].

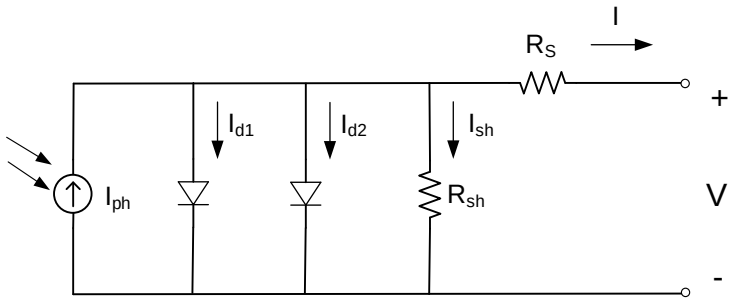

Fig. 2-7. Static equivalent circuit model of a PV cell with two diodes, a series resistance R_s and a shunt resistance R_{sh}

Equation (2-4) can then be modified as:

$$I = I_{\text{ph}} - f'(V + I \cdot R_s) - \left(\frac{V+I\cdot R_s}{R_{sh}}\right) = I_{\text{ph}} - I_d - \left(\frac{V+I\cdot R_s}{R_{sh}}\right) \tag{2-5}$$

where

$$I_d = I_{d1} + I_{d2} = I_{o1} \cdot \left(e^{\left(\frac{V+I\cdot R_s}{n1\cdot V_T}\right)} - 1\right) + I_{o2} \cdot \left(e^{\left(\frac{V+I\cdot R_s}{n2\cdot V_T}\right)} - 1\right) \tag{2-6}$$

and I_{o1} and I_{o2} are the diode saturation current while n_1 and n_2 are the ideality factor for diode 1 and 2 respectively.

2.2.3 Dynamic I-V Characteristics

The conventional equivalent circuit model as shown in Fig. 2-6 and Fig. 2-7 is static in nature that precludes the transient behaviour of the photocurrent produced by the PV cell. The

conventional model has been developed based on the assumption that the photo-generated current I_{ph} is constant for given incident light intensity and is independent of voltage. A dynamic behaviour with the modulation of photocurrent of PV cell as a function of voltage in reverse-biased mode can be attributed to the presence of a nonlinear depletion capacitance around the p-n junction. It has been reported that PV cell under dark condition is capacitive and can be equivalent to a parallel circuit consisting of a diode and its junction capacitance [7], [8], [9]. Based on Kirchhoff's current law, it has been deduced that the ideal dynamic model of the PV cell must be parallel circuit composed of the photocurrent source, the diode and its equivalent capacitance.

The modified equivalent circuit model for photovoltaic cell with dynamic behaviour used in this research is as shown in Fig. 2-8. The capacitive effect is due to the excess of minority carriers stored in the quasi-neutral region of a diode. These effects can be modelled by the use of a voltage and frequency dependent junction capacitance C_j. C_J is made up of two components, namely the diffusion capacitance C_d in forward bias mode, and the depletion capacitance which is also termed as the transition capacitance, C_t in reverse bias mode. Refer to Section 2.6.2 for a more detailed explanation of C_d and C_t. L_s is included to model the inductive effect due to the wiring of the PV cell [3].

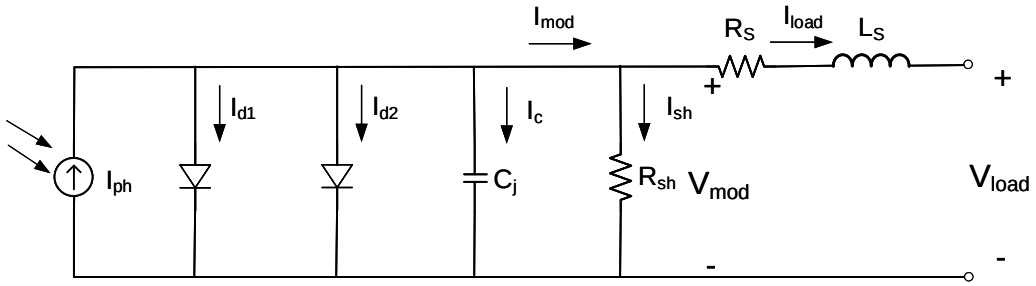

Fig. 2-8. Dynamic equivalent circuit model of a PV cell with junction capacitance C_j

The junction capacitance C_j can be determined by the use of equation (2-7) [10].

$$I_c = C_j \cdot \frac{dV_{mod}}{dt} + V_{mod} \cdot \frac{dC_j}{dt} \quad (2\text{-}7)$$

The capacitive current I_c is the result of modulating excitation source V_{mod} across the pn-junction and dynamic capacitive effect C_j of the pn-junction. The photocurrent I_{mod} is time varying and is modulated by the use of an external excitation source in this case. Hence, the output current I_{load} is a dynamic function of the modulating photocurrent I_{mod}.

2.3 Photocurrent Measurement Techniques

This section presents the various direct current measurement techniques that had been reported in the past with regards to the photoelectrical response measurement of bacteriorhodopsin (bR) based photoreceptors. However, the techniques are not restricted to bR-based photoreceptors alone and can be generally applied to any optical sensors.

When a bR-based photodetector is incorporated into an artificial membrane, illumination by a continuous light will generate a proton gradient across the membrane. This approach is used to measure the DC photoelectric effect of the photodetector. For AC photoelectric effect, a short pulse of light can be used to excite the photodetector to register a fast photoelectric response.

The photoelectric output of bR-based photodetector has been examined as a function of differential light intensity in [5] as the rate of change in imaging light intensity. Fig. 2-9 shows the response profile of photoelectric signals from a bR-based photoreceptor. The photoreceptor was exposed to green light supplied by a 150W Xenon arc lamp in combination with a bandpass filter (transmission > 470nm with peak at 540nm, maximum intensity of 5 – 10 mW/cm^2). The light intensity was changed stepwise during irradiation by the use of neutral density filters. Its pattern as monitored by a photodiode is shown at the bottom of Fig. 2-9. Each step corresponds to an equivalent change in light intensity of ~ 2 mW/cm^2. The response appears differential against light intensity change. The polarity of the photo response changes at the rising and falling edges of the input step signal, which corresponds to the charge displacement inside the bR film. The peak of the differential response varies directly with changes in light intensity provided that saturation does not occur. The magnitude of such response is also dependent upon the wavelength of the incident light.

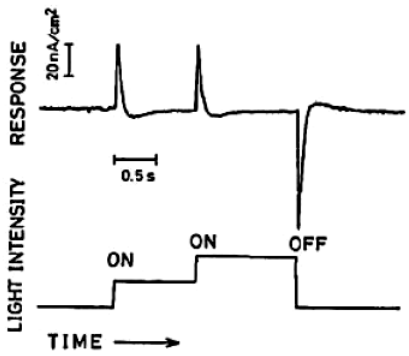

Fig. 2-9. Response profile of photoelectric signals from a bR-based photoreceptor [11]

2.3.1 Current Amplification Technique

In conventional method, photoelectric response of sensors is measured with current detection method. The weak photocurrent is amplified using operational amplifier as shown in Fig. 2-10 [12]. The bR-based photodetector is connected to the inverting input of an op-amp. The load resistance R_f and capacitance C_f are connected on the feedback loop of the op-amp.

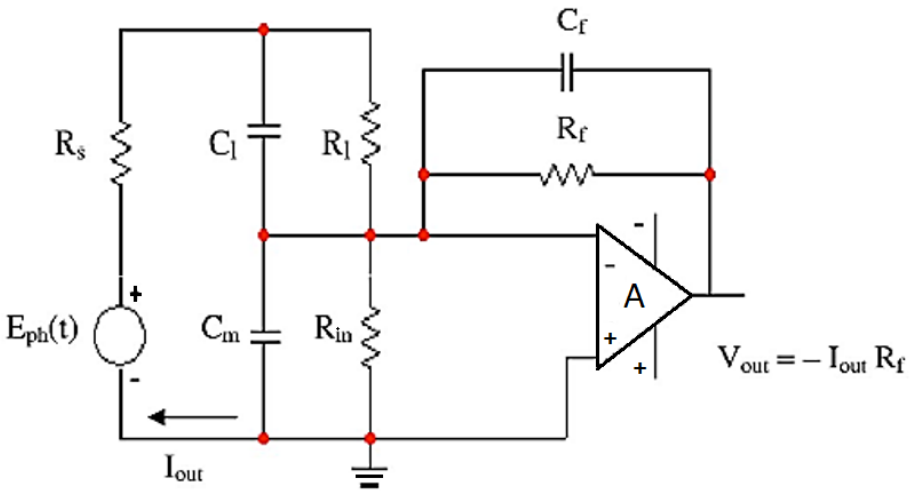

Fig. 2-10. Simplified equivalent circuit of bR-based photodetector measured by photocurrent mode [12]

Another readout circuit to measure the dynamic photoelectric response of the bR-based photodetector is as shown in Fig. 2-11 [13]. The bR-based photodetector goes directly to the non-inverting input of the precision op-amp LMC6061 which has input impedance of about 10 TΩ. The conditioned signals were fed directly into a 2G sampling/s 100 MHz digital oscilloscope (Agilent 54825A). The photodetector together with the processing circuit was placed in a light sealed metal box to avoid environmental electromagnetic interference. A

tunable lamp was used as the light source to excite the photodetector. The measurements were performed at the room temperature.

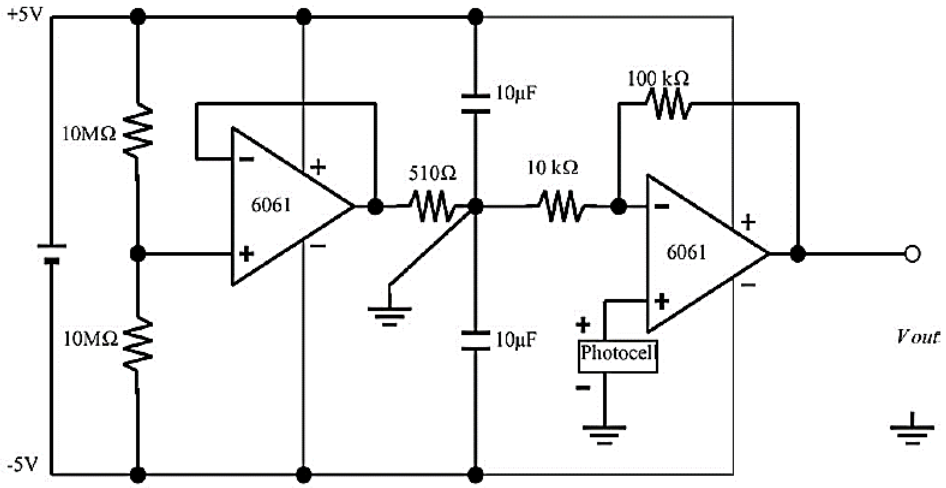

Fig. 2-11. Signal processing circuit to measure the dynamic photoelectric response of bR-based photodetector [13]

Miyasaka and Koyama [11] reported an amplification circuit with the use of dual operational amplifiers. Photocurrents produced at the photoreceptor are converted and amplified in the voltage mode by the two operational amplifiers as shown in Fig. 2-12. The amplified voltage is used to drive a LED for each photosensor for parallel image display. The photo response was found to be non-linear and appears to fit a hyperbola. It wasn't known the mechanism for the non-linear relationship at that stage of investigation.

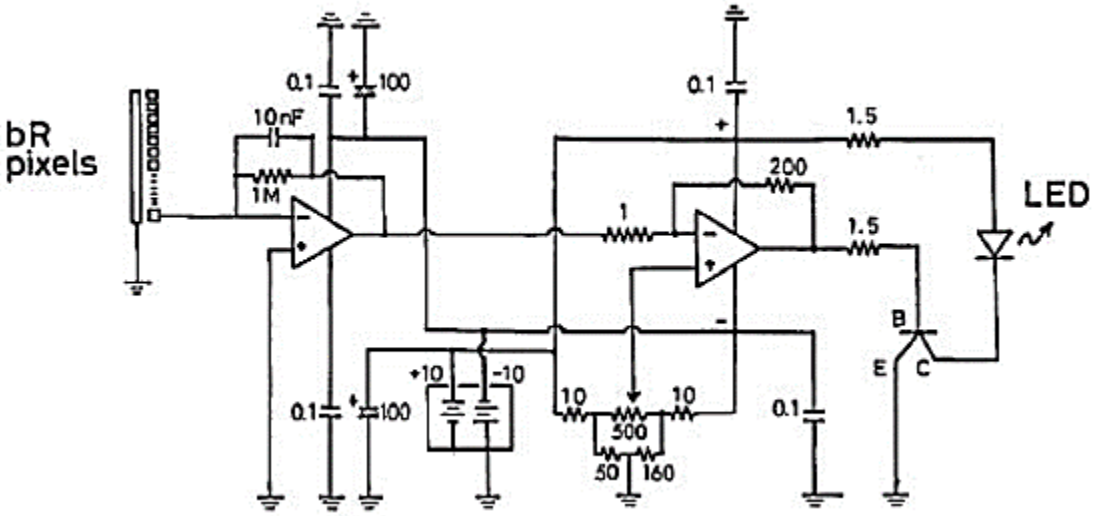

Fig. 2-12. Signal transmission and amplification circuit for image display [11]

2.3.2 Charge Amplification Technique

A charge amplifier is a current integrator which produces an output voltage in proportional to the integrated value of the input current. The circuit acts as a charge-to-voltage converter. While a current amplifier converts current to voltage by the use of a resistor, a charge amplifier converts electric charge to voltage by the use of a capacitor. Fig. 2-13Fig. 2-13 shows the comparison of a current amplifier versus a charge amplifier [14]**.** A charge amplifier has been proposed to measure the photo response of a bR-based photoreceptor with ITO/bR/KCI/Au sandwiched structure.

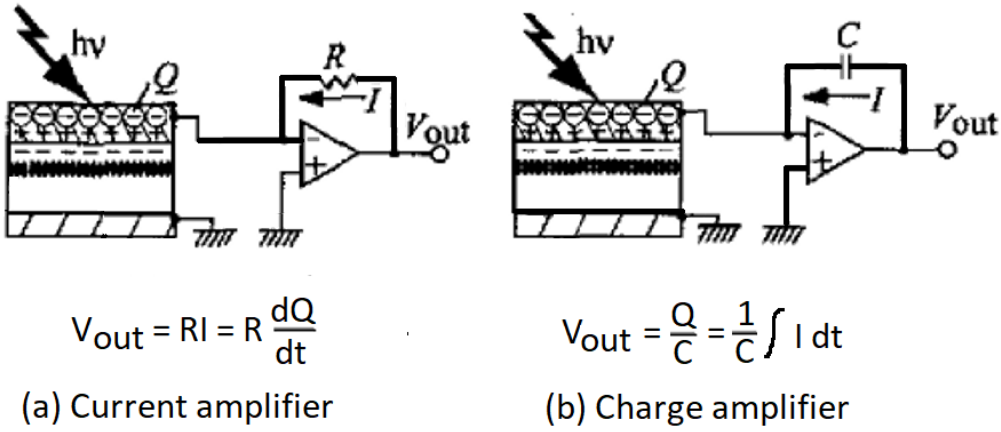

Fig. 2-13. Comparison of current amplifier versus charge amplifier [14]

If the charge generating response is measured by current, a differential waveform is observed as current is defined as I = dq/dt, and the bR photoreceptor generates electric charges in proportional to the incident light intensity. In [14]**,** a halogen lamp was projected on a bR-based photodetector where the light intensity was 3.3 mW/cm^2 for the first 2 seconds and 5.3 mW/cm^2 for the next 2 seconds as shown in Fig. 2-14(a). For the case of current detection, only differential response of the intensity has been obtained as shown in Fig. 2-14(b). In contrast, for the case of charge detection, the proportional response to the light intensity has been observed as shown in Fig. 2-14(c). Hence, the charge detection method is more accurate as the method is able to detect the proportional response of the photodetector in tandem with the light intensity. However, the accuracy of this method is subjected to circuit component variation and environmental noise just like the case for current detection method [11]**.**

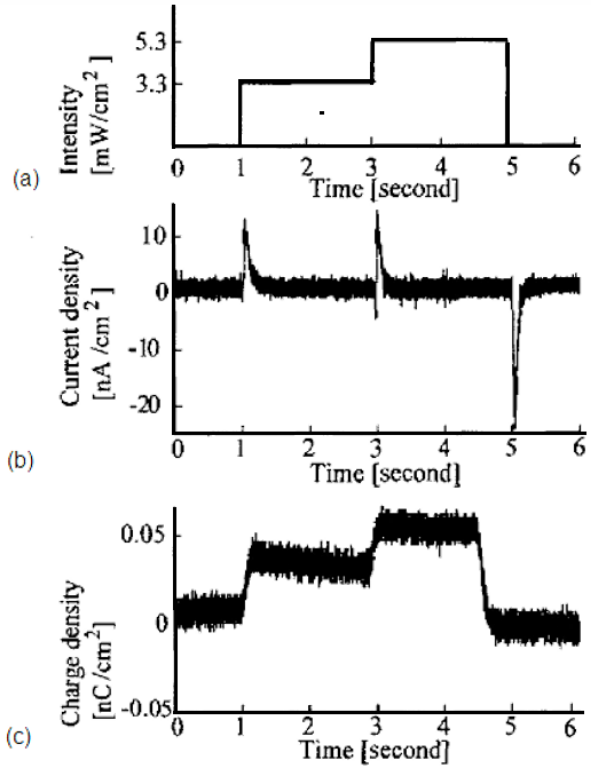

Fig. 2-14. (a) Profile of light intensity, (b) output signal of bR-based photodetector measured with a current amplifier, (c) output signal of bR-based photodetector measured with a charge amplifier [14]

2.3.3 Switched Integration Technique

Based on current approach, bR sensors will be polarised by exposure to light and the state of polarisation is assessed by direct time-domain photocurrent measurement. Wang et al. [15] has proposed the design of using a switched integrator from IVC102 chip as a preamplifier for each sensing element as shown in Fig. 2-15. The three dashed boxes represent the simplified bR equivalent circuit model, switched integrator implemented using IVC102 chip and a sample & hold circuitry. The output of the photoreceptor is connected to the inverting input of the op-amp via a sample switch S_1 while the non-inverting input is grounded, Switch S_2 connected in parallel with the integrating capacitors to provide a discharging path. Amplified signal is connected to a holding capacitor via a readout switch S_3. A PIC12F675 microcontroller is programmed to provide the digital timings for $S_1 – S_3$ switches. To process each of the multiple photoreceptors, a multi-channel readout architecture is used.

As the resistance of a bR element is in the range of $10^{10} – 10^{12}$ Ω, the test performance is highly dependence on the electronic circuitry used to condition and amplify the extremely

small signal. A highly optimized electronic circuit with high input-impedance and low noise amplification is thus desirable.

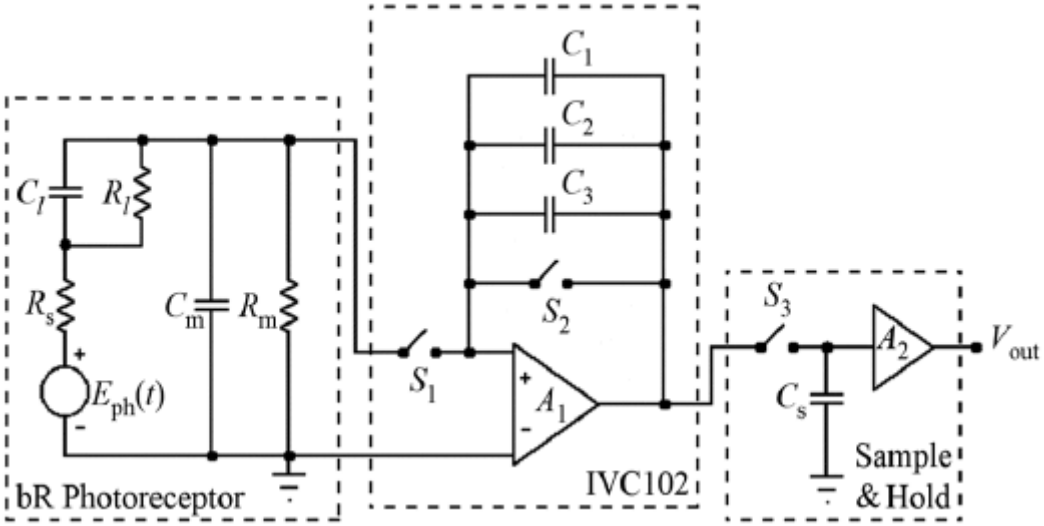

Fig. 2-15. Switching integrator circuitry for measuring the photoelectric response of bR photoreceptor [15]

2.3.4 MOS Transistor Amplification

Jonhyun Shin et. al. [16] demonstrated the integration of bR film with a silicon n-channel Metal Oxide Semiconductor Field Effect Transistor (MOSFET) to form a photordetector as shown in Fig. 2-16. The external resistance R_{ext} is 100 MΩ which matches the resistance of the bR film. The photodetector circuit as shown in Fig. 2-16 has been biased for dc operation of the nMOS transistor with a drain-source voltage, V_{ds} = 0.7 V. The excitation was provided by an unpolarized 594 nm light source from a He-Ne laser (0.8 W/cm^2). The dc bias across the gate-source voltage, V_{gs} = 1.1 V, shifts the operating point of the transistor to the maximum gain. The time varying voltage generated across the bR film due to the pulsed photo-excitation is superimposed on V_{gs}. The circuit converts the photovoltage generated across the bR film into a useful photocurrent with a responsivity of 4.7 mA/W. However, this method requires the optimization of transistor parameters to achieve higher values of responsivity.

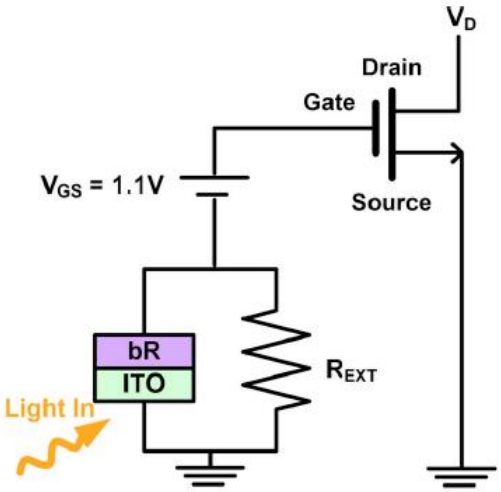

Fig. 2-16. Measuring photoelectric response of bR photoreceptor by incorporating an external resistance and a dc gate-source biasing voltage [16]

2.4 Nonlinear System Modeling with Volterra Series

A nonlinear system is generally any system that does not satisfy the superposition principle. The frequency domain analysis of nonlinear systems is much more complicated than that of linear systems as nonlinear systems usually have very complicated nonlinear behaviors such as super-harmonics, sub-harmonics, intermodulation, and even bifurcation and chaos. The frequency domain theory for linear systems can not directly be extended to nonlinear cases. The analysis of nonlinear systems in frequency domain has been conducted for many years [17], [18] in particular using Volterra series [19], [20]. An important aspect for nonlinear systems in the frequency domain is that there are always very complicated output frequencies appearing as super-harmonics, sub-harmonics, intermodulation and so on in the output spectrum. Using Volterra series to model the nonlinear systems can effectively account for theses super-harmonics and intermodulation in the output spectrum [21], [22]. This section will cover the theoretical basis of Volterra series to model the nonlinear system, its advantages and limitations. The next section will highlight some of the works that have been carried out over recent years using the expansion method of Volterra series in detecting nonlinearities.

A Volterra series is a model for nonlinear behaviour similar to Taylor series except for its ability to capture the memory effects as compared to the Taylor series. Any system behaviour that can be modelled with Taylor series expansion is virtually a Volterra series system. The Taylor series is used to approximate the response of a nonlinear system to a given input if the

output of the system depends strictly on the input at that particular time. In contrast, the nonlinear output of a Volterra series system depends on the input to the system at all other times. Hence, Volterra series system has the ability to capture the memory effect of devices like capacitors and inductors.

In general, Volterra series is a power series with memory. The Volterra series is basically an extension of linear convolution integral. The discrete time case of Volterra series can be expressed by equation (2-8) [23].

$$y(k) = h_0 + \sum_{m_1=1}^{M} h_1(m_1)u(k-m_1) + \sum_{m_1=1}^{M}\sum_{m_2=1}^{M} h_2(m_1,m_2)u(k-m_1)u(k-m_2) + \sum_{m_1=1}^{M}\sum_{m_2=1}^{M}\sum_{m_3=1}^{M} h_3(m_1,m_2,m_3)u(k-m_1)u(k-m_2)u(k-m_3) + \quad (2\text{-}8)$$

where *u(k)* is the measured input, *y(k)* is the measured output, and $h_l(m_1, \ldots, m_l)$ is the order of Volterra kernel which is essentially the order of nonlinear impulse response. Equation (2-8) can be regarded as a generalization of the traditional convolution description, e.g. the impulse response of linear systems. Most of earlier identification algorithms assume the use of Gaussian white noise and correlation methods to identify the first two linear and quadratic Volterra kernel. As the input needs to be white Gaussian noise, this imposes a severe restriction on the application of this model to many real processes.

A systematic approach to the analysis and design of system output frequency response making use of system time domain model parameters is proposed by [24]. The system satisfies the conditions of bounded, smooth and continuous change of bound with respect to the input. In [24], output frequency response function (OFRF) based analysis allows the design and analysis of output frequency response of nonlinear Volterra systems to be conducted as a function of system time domain model parameters with respect to any specific input signal. Lang et al. [25] has proposed a multilevel excitation method required to excite the system under study many times by inputs of the same form but different intensities. By using this method, the estimation of the nonlinear OFRF can be implemented directly using the system input-output data.

The more recent works on Volterra series focus on the conditions of series convergence which is not the focus of this research. The work of system modelling using Volterra series is not new. This work makes use of nonlinear systems that is amenable to the Volterra series

modelling, find the measurable effects and its potential use as a proxy of indirect measurement.

2.4.1 Single-Input Volterra Series

A generalization of input-output relation for linear systems is expressed in equation (2-9).

$$y(t) = \int_{-\infty}^{+\infty} h(t-\tau)x(\tau)d\tau \tag{2-9}$$

where h(t) is the impulse response function, x(t) is the input while y(t) is the output of the system.

Fourier transform *F* of equation (2-9) is given as

$$Y(w) = H(w)X(w) \tag{2-10}$$

where *X(w), H(w) and Y(w)* are the Fourier transforms of x(t), h(t) and y(t) respectively. *H(w)* is called the Frequency Response Function (FRF) of the system which contains all the information about the system.

Extended form of equation (2-9) can be represented by Volterra series [20].

$$y(t) = y_1(t) + y_2(t) + y_3(t) \tag{2-11}$$

where

$$y_1(t) = \int_{-\infty}^{+\infty} h_1(\tau)x(t-\tau)d\tau \tag{2-12}$$

$$y_2(t) = \int_{-\infty}^{+\infty}\int_{-\infty}^{+\infty} h_2(\tau_1,\tau_2)x(t-\tau_1)x(t-\tau_2)d\tau_1\, d\tau_2 \tag{2-13}$$

$$y_3(t) = \int_{-\infty}^{+\infty}\int_{-\infty}^{+\infty}\int_{-\infty}^{+\infty} h_3(\tau_1,\tau_2,\tau_3)x(t-\tau_1)x(t-\tau_2)x(t-\tau_3)d\tau_1\, d\tau_2\, d\tau_3 \tag{2-14}$$

Functions $h_1(\tau)$, $h_2(\tau_1,\tau_2)$, $h_3(\tau_1,\tau_2,\tau_3)$, … , $h_n(\tau_1,\dots,\tau_n)$, … are referred to as Volterra kernels which are generalizations of linear impulse response functions.

[26] shows that Volterra kernels can be treated symmetric without loss of generality, i.e.

$$h_2(\tau_1,\tau_2) = h_2(\tau_2,\tau_1).$$

$$y_2(t) = \int_{-\infty}^{+\infty}\int_{-\infty}^{+\infty} h_2(\tau_1,\tau_2)\prod_2((\tau_1,\tau_2;t)\, d\tau_1\, d\tau_2 \tag{2-15}$$

where

$$\prod_2((\tau_1,\tau_2;t) = x(t-\tau_1)x(t-\tau_2) \tag{2-16}$$

Function $h_2(\tau_1,\tau_2)$ can be canonically decomposed into symmetric and asymmetric parts,

$$h_2(\tau_1,\tau_2) = h_2^{sym}(\tau_1,\tau_2) + h_2^{asym}(\tau_1,\tau_2) \tag{2-17}$$

where

$$h_2^{sym}(\tau_1,\tau_2) = \frac{1}{2}(h_2(\tau_1,\tau_2) + h_2(\tau_2,\tau_1)) \tag{2-18}$$

$$h_2^{asym}(\tau_1,\tau_2) = \frac{1}{2}(h_2(\tau_1,\tau_2) - h_2(\tau_2,\tau_1)) \tag{2-19}$$

Since $h_2^{asym}(\tau_1,\tau_2)\prod_2(\tau_1,\tau_2;t) = -h_2^{asym}(\tau_2,\tau_1)\prod_2(\tau_2,\tau_1;t)$, the overall integral will cancel out each other.

Dual frequency domain representation for non-linear systems for higher order FRFs can be expressed as

$$H_n(w_1,\dots,w_n) = \int_{-\infty}^{+\infty}\dots\int_{-\infty}^{+\infty} h_n(\tau_1,\dots,\tau_n)e^{-i(w_1\tau_1+\dots+w_n\tau_n)}\,d\tau_1\dots d\tau_n \tag{2-20}$$

$$h_n(\tau_1,\dots,\tau_n) = \frac{1}{(2\pi)^{n-1}}\int_{-\infty}^{+\infty}\dots\int_{-\infty}^{+\infty} H_n(w_1,\dots,w_n)e^{i(w_1\tau_1+\dots+w_n\tau_n)}dw_1\dots dw_n \tag{2-21}$$

Dual frequency domain expression for equation (3-5) is given as

$$Y(w) = Y_1(w) + Y_2(w) + Y_3(w) + \cdots \tag{2-22}$$

where

$$Y_1(w) = H_1(w)X(w) \tag{2-23}$$

$$Y_2(w) = \frac{1}{2\pi}\int_{-\infty}^{+\infty} H_2(w_1, w-w_1)X(w_1)X(w-w_1)dw_1 \tag{2-24}$$

$$Y_3(w) = \frac{1}{(2\pi)^2}\int_{-\infty}^{+\infty} H_3(w_1,w_2,w-w_1-w_2)X(w_1)X(w_2)X(w-w_1-w_2)dw_1dw_2 \tag{2-25}$$

2.4.2 Multi-Input Volterra Series

Consider a nonlinear system excited at location *a* and *b* with input $x^{(a)}(t)$ and $x^{(b)}(t)$.

The expression for the response at point *j* is

$$y^{(j)}(t) = y_1^{(j)}(t) + y_2^{(j)}(t) + y_3^{(j)}(t) + \cdots$$

(2-26)

For the two-input case, the components are given by

$$y_n^{(j)}(t) = \int_{-\infty}^{+\infty} \dots \int_{-\infty}^{+\infty} h_n^{(j:aa\dots aa)}(\tau_1, \dots, \tau_n) x^{(a)}(t-\tau_1) \dots x^{(a)}(t-\tau_n) d\tau_1 \dots d\tau_n +$$
$$\cdots + \int_{-\infty}^{+\infty} \dots \int_{-\infty}^{+\infty} h_n^{(j:aa\dots bb)}(\tau_1, \dots, \tau_n) x^{(a)}(t-\tau_1) \dots x^{(b)}(t-\tau_n) d\tau_1 \dots d\tau_n +$$
$$\int_{-\infty}^{+\infty} \dots \int_{-\infty}^{+\infty} h_n^{(j:bb\dots bb)}(\tau_1, \dots, \tau_n) x^{(b)}(t-\tau_1) \dots x^{(b)}(t-\tau_n) d\tau_1 \dots d\tau_n$$

(2-27)

i.e.

$$y_1^{(j)}(t) = \int_{-\infty}^{+\infty} h_1^{(j:a)}(\tau) x^{(a)}(t-\tau) d\tau + \int_{-\infty}^{+\infty} h_1^{(j:b)}(\tau) x^{(b)}(t-\tau) d\tau$$

(2-28)

$$y_2^{(j)}(t) = \int_{-\infty}^{+\infty} \int_{-\infty}^{+\infty} h_2^{(j:aa)}(\tau_1, \tau_2) x^{(a)}(t-\tau_1)\, x^{(a)}(t-\tau_2) d\tau_1 d\tau_2 +$$
$$\int_{-\infty}^{+\infty} \int_{-\infty}^{+\infty} h_2^{(j:ab)}(\tau_1, \tau_2) x^{(a)}(t-\tau_1)\, x^{(b)}(t-\tau_2) d\tau_1 d\tau_2 +$$
$$\int_{-\infty}^{+\infty} \int_{-\infty}^{+\infty} h_2^{(j:ba)}(\tau_1, \tau_2) x^{(b)}(t-\tau_1)\, x^{(a)}(t-\tau_2) d\tau_1 d\tau_2 +$$
$$\int_{-\infty}^{+\infty} \int_{-\infty}^{+\infty} h_2^{(j:bb)}(\tau_1, \tau_2) x^{(b)}(t-\tau_1)\, x^{(b)}(t-\tau_2) d\tau_1 d\tau_2$$

(2-29)

$$\left\{ h_2^{(j:ab)}(\tau_1, \tau_2) + h_2^{(j:ba)}(\tau_2, \tau_1) \right\} \rightarrow 2h_2^{(j:ab)}(\tau_1, \tau_2)$$

(2-30)

Dual frequency representation is given by

$$Y^{(j)}(w) = Y_1^{(j)}(w) + Y_2^{(j)}(w) + Y_3^{(j)}(w) + \cdots$$

(2-31)

$$Y_n^{(j)}(w) = \left(\frac{1}{2\pi}\right)^{n-1} \int_{-\infty}^{+\infty} \dots \int_{-\infty}^{+\infty} H_n^{(j:aa\dots aa)}(w_1, w_2, \dots, w - w_1 - \cdots - w_{n-1}) \cdot$$
$$X^{(a)}(w_1) X^{(a)}(w_2) \dots X^{(a)}(w_{n-1}) X^{(a)}(w - w_1 - \cdots - w_{n-1}) dw_1 \dots dw_{n-1} + \cdots +$$
$$\left(\frac{1}{2\pi}\right)^{n-1} \int_{-\infty}^{+\infty} \dots \int_{-\infty}^{+\infty} H_n^{(j:aa\dots bb)}(w_1, w_2, \dots, w - w_1 - \cdots - w_{n-1}) \cdot$$
$$X^{(a)}(w_1) X^{(a)}(w_2) \dots X^{(b)}(w_{n-1}) X^{(b)}(w - w_1 - \cdots - w_{n-1}) dw_1 \dots dw_{n-1} + \cdots +$$
$$\left(\frac{1}{2\pi}\right)^{n-1} \int_{-\infty}^{+\infty} \dots \int_{-\infty}^{+\infty} H_n^{(j:bb\dots bb)}(w_1, w_2, \dots, w - w_1 - \cdots - w_{n-1}) \cdot$$
$$X^{(b)}(w_1) X^{(b)}(w_2) \dots X^{(b)}(w_{n-1}) X^{(b)}(w - w_1 - \cdots - w_{n-1}) dw_1 \dots dw_{n-1}$$

(2-32)

Consider the object $y_3^{(j:aab)}$ for the third order component of the output

$$y_3^{(j:aaab)} = \int_{-\infty}^{+\infty} \int_{-\infty}^{+\infty} \int_{-\infty}^{+\infty} h_3^{(j:aab)}(\tau_1, \tau_2, \tau_3) \prod_3^{(j:aab)}(\tau_1, \tau_2, \tau_3; t)\ d\tau_1 d\tau_2 d\tau_3$$

(2-33)

where

$$\prod_3^{(j:aab)}(\tau_1,\tau_2,\tau_3;t) = x^{(a)}(t-\tau_1)\,x^{(a)}(t-\tau_2)x^{(b)}(t-\tau_3)$$

(2-34)

Volterra series expansion is a very useful and convenient modelling technique used in the analysis of a very wide class of both deterministic and stochastic nonlinear systems [20], [27]. With the existence of Volterra series expansion, the study of nonlinear systems in the frequency domain was initiated by the introduction of the concept of Generalized Frequency Response Functions (GFRFs) [28] as defined in equation (2-20). The GFRFs can be obtained by using the Harmonic probing method presented in section 2.4.3.

2.4.3 Harmonic Probing Method

Harmonic probing is a method based on Volterra series to determine the analytical form of the kernel transforms which was introduced by [29] for systems with continuous-time equations of motion, and by [30] for discrete-time systems.

Periodic excitation of a single harmonic is given by

$$x(t) = e^{i\Omega t}$$

(2-35)

Based on equation (3-5),

$$y(t) = H_1(\Omega)e^{i\Omega t} + H_2(\Omega,\Omega)e^{i2\Omega t} + H_3(\Omega,\Omega,\Omega)e^{i3\Omega t} + \cdots$$

(2-36)

For multi-frequency excitations with "two-tone" input

$$x(t) = e^{i\Omega_1 t} + e^{i\Omega_2 t}$$

(2-37)

then

$$y(t) = H_1(\Omega_1)e^{i\Omega_1 t} + H_1(\Omega_2)e^{i\Omega_2 t} + H_2(\Omega_1,\Omega_1)e^{i2\Omega_1 t} + 2H_2(\Omega_1,\Omega_2)e^{i(\Omega_1+\Omega_2)t} + H_2(\Omega_2,\Omega_2)e^{i2\Omega_2 t} + H_3(\Omega_1,\Omega_1,\Omega_1)e^{i3\Omega_1 t} + 3H_3(\Omega_1,\Omega_1,\Omega_2)e^{i(2\Omega_1+\Omega_2)t} + 3H_3(\Omega_1,\Omega_2,\Omega_2)e^{i(\Omega_1+2\Omega_2)t} + H_3(\Omega_2,\Omega_2,\Omega_2)e^{i3\Omega_2 t} + \cdots$$

(2-38)

For a more general periodic excitation,

$$x(t) = e^{i\Omega_1 t} + e^{i\Omega_2 t} \ldots + e^{i\Omega_{n-1} t} + e^{i\Omega_n t}$$

(2-39)

The amplitude of the output component at frequency $(\Omega_1 + \Omega_2 + \cdots + \Omega_{n-1} + \Omega_n)$ is $n!\,H_n(\Omega_1 + \Omega_2 + \cdots + \Omega_{n-1} + \Omega_n)$ which forms the basis of harmonic probing algorithm.

2.4.4 Advantages of Volterra Series

Volterra series is not an iterative method, hence it is capable of providing a closed form presentation of the distortion. Volterra series is a mathematically elegant method for a considerably large class of nonlinear systems frequently encountered in different fields, not restricting to a specific nonlinear unit or single nonlinear component. It basically holds for any bounded deterministic or stochastic input signals. With Volterra series expansion, the resulting GFRFs of nonlinear systems are similar to transfer functions of linear systems. The system characteristic parameters including model parameters and input magnitude, can be related to system output frequency response. The GFRFs can be recursively computed in terms of model parameters which greatly facilitate the nonlinear system analysis. Strong nonlinear behaviour such as chaos or bifurcation can also be investigated with the Volterra series based methods.

2.4.5 Limitations of Volterra Series

Volterra series is only applicable to "weakly nonlinear" systems whereby the infinite sum nonlinearities will converge rapidly. Volterra series is impractical in strongly nonlinear systems whereby the sum of "strongly nonlinearities" will diverge to render Volterra series expansion invalid. This is because the series relies on the polynomial models which may not cover all operating regimes with a reasonable number of terms. However, provided the polynomial model is locally modelled around the bias point with large signal amplitude range, it can still be very accurate.

2.5 Output Spectrum of Volterra Systems

Different nonlinearities can interact with each other such that the output harmonics become complicated due to crossing effects of different nonlinearities. However, the mechanism about what the crossing effect is and how the different output harmonics interact with each other is not explicitly studied and seldom reported. [31] has studied details of the interaction mechanism of super-harmonics and intermodulation in the output frequencies of Volterra systems due to different input nonlinearities under the assumption that the nonlinearities only exist in system input. The work has revealed explicitly in a general and analytical form to provide insight into the nonlinear behavior in the output spectrum of Volterra systems such as the periodicity and opposite property of the output super-harmonics and intermodulation

frequencies. When considering more complicated cases involving different nonlinearities existing in the input and output of the system, the periodicity of the output frequencies can still be observed but the interaction due to crossing effects at some frequencies between different output harmonics usually produce very complicated output spectrum.

Different nonlinearities may have quite different effects on the system output spectrum and there will be many crossing effects at the same frequency from different nonlinearities. Nonlinearities of $u(t)^3$ and $u(t)u(t)^2$ are both input nonlinearity with nonlinear degree of three (3), can produce the same output frequencies according to [32]. However, the effect from different nonlinearities at the same frequency generation period may counteract with each other such that the output spectrum may be suppressed over some periods and enhanced in some others as shown in Fig. 2-17.

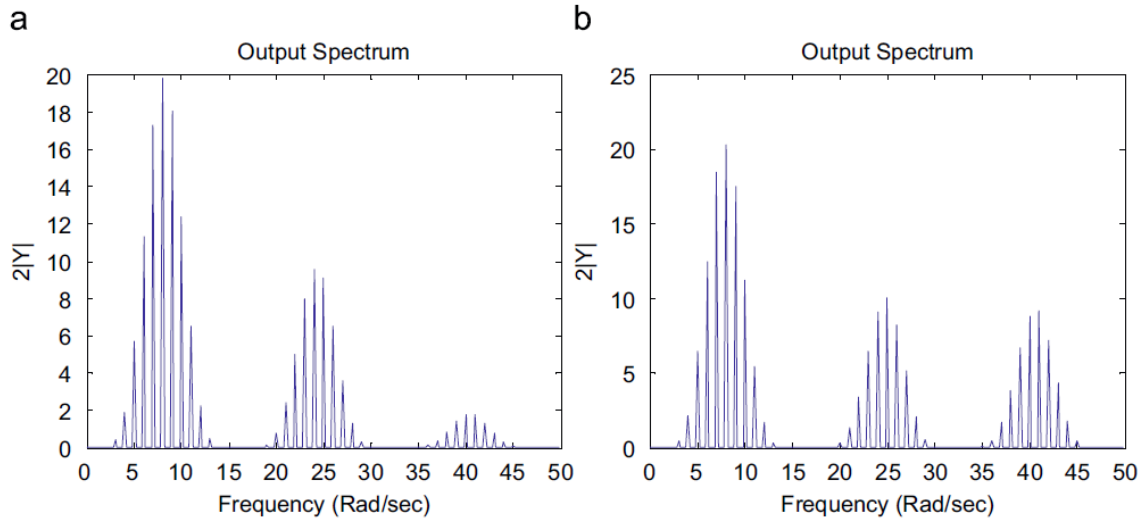

Fig. 2-17. Output spectrum with input nonlinearity $au(t)^5$ and $bu(t)^3u(t)^2$ when (a) $a = 1.3, b = 0$ and (b) $a = 0, b = 0.1$ [31]

Reference [33] has provided a survey of the numerous nonlinear system techniques, such as but limited to test on superposition and homogeneity principles; distortion check on overlaid bode plot, Nyquist plot, Carpet plot; statistical checks on coherence function, correlation function, Hilbert transform, harmonic detection function, etc. The work has made use of a "quarter car" measurement setup of Fig. 2-18 which is a simplified representation of the suspension of one wheel of a car to investigate the existence and level of nonlinear distortions present in the system by employing those detection techniques under investigation. Of particular interest is the detection carried out using random phase multisine excitation [34], [35] with equation (2-40). The multisine excitation is a very fast nonlinear detection

technique that provides a detailed information of the FRF of the investigated system, absolute values of the amount, and the frequency localization of the even and odd nonlinear distortions in the entire output spectrum under investigation in one clear picture as shown in Fig. 2-19.

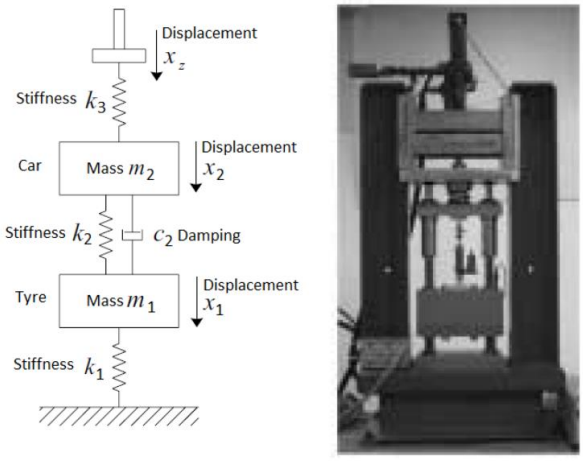

Fig. 2-18. Schematic diagram of a "quarter car" [33]

$$x(t) = \left(\frac{1}{\sqrt{N}}\right)\left(\sum_{k=-N}^{N} X_k \cdot e^{j2\pi\left(\frac{f_{max}}{N}\right)kt}\right) \tag{2-40}$$

with $X_k = X_{-k}^* = X(k) \cdot e^{j\varphi_k}$, f_{max} the maximum frequency of the excitation signal, $N \in$ the number of frequency components and the phases φ_k are a realization of an independent uniformly distributed random process on [0, 2π].

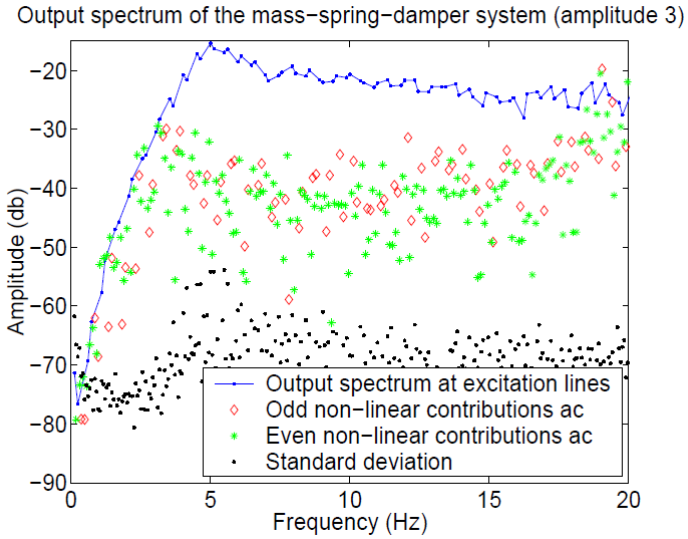

Fig. 2-19. Output spectrum of the system with even and odd nonlinear contributions at the intermediate lines obtained with a special odd multisine after compensation [33]

The main principle of this particular technique lies on only a well-chosen set of frequency lines are excited. This implies that some frequency lines are consciously not excited and be used instead as detection lines to qualify and quantify the nonlinear distortions on the neighbouring excited lines (called measurement lines). The even nonlinear disturbances are determined at the even frequency lines while the odd nonlinear distortions are determined at the unexcited odd frequency lines

In [36] is proposed a method for estimating non-parametrically the dynamic part of the time-variant FRF from known input and noisy output observations. The non-parametric representation of the dynamics of the time-variant FRF is obtained in two steps. The time-variant FRF is first expanded in series with respect to time in accordance with equation (2-41).

$$G(jw,t) = \sum_{r=0}^{\infty} G_r\,(\mathrm{jw}) \cdot f_r(t), \quad t \in [0,T] \tag{2-41}$$

with $f_r(t)$, $r = 0, 1, \ldots$, a complete set of basis functions and T the experiment time. $G_r(jw)$, $r = 0, 1, \ldots$, are the complex coefficients of the series expansion which can be interpreted as FRFs of linear time-invariant systems.

In second step, the infinite sum of equation (2-41) is approximated by a finite sum given by equation (2-42).

$$G(jw,t) = \sum_{r=0}^{N_b} G_r\,(\mathrm{jw}) \cdot f_r(t), \quad t \in [0,T] \tag{2-42}$$

Representation given by equation (2-42) is parametric in the time variation as the basis functions $f_r(t)$ are known, and non-parametric in the unknown FRFs $G_r(jw)$, $r = 0, 1, \ldots, N_b$.

The experimental set-up is a time-variant second order bandpass filter as shown in Fig. 2-20. The circuit consists of a high gain operational amplifier (CA741CE), a JFET transistor (BF245B) with gate voltage $p(t)$, three resistors ($R_1 = R_2 = 10\ k\Omega$ and $R_3 = 470\ k\Omega$), and two capacitors ($C_1 = C_2 = 10\ nF$). It is excited by a random phase multisine given by equation (2-43) with $F = 33387$ harmonically related sine waves in the band $[200\ Hz, 40\ kHz]$ where $f_o = \frac{f_s}{N_o}$, $N_o = 2^{17}$, $f_s = 156.25\ kHz$, $k_1 = 168$ and $k_2 = 33554$.

The amplitudes A_k, $k = k_1, k_1 + 1, \ldots, k_2$ are constant and chosen such that rms value of $u(t)$ is 93 mV while the phases φ_k, $k = k_1, k_1 + 1, \ldots, k_2$ are randomly selected to a uniform [0, 2π) distribution.

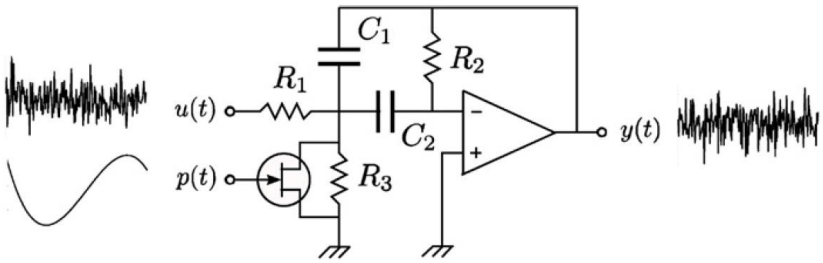

Fig. 2-20. Schematic diagram of second-order bandpass filter with time-varying resonance frequency and damping ratio [36]

$$u(t) = \sum_{k=k_1}^{k_2} A_k \sin(2\pi k f_o t + \varphi_k) \tag{2-43}$$

consisting of $F = k_2 - k_1 + 1$ harmonically related sine waves with user defined deterministic amplitudes A_k, and randomly selected phases φ_k such that $E\left[e^{j\varphi_k}\right] = 0$.

Only $N = \frac{7}{8} N_o$ data points of the input $u(t)$ and the noisy output response $y(t)$ are used for estimating non-parametrically the time-variant FRF given by equation (2-42) over the measurement time $T = N \cdot T_s$ with $T_s = \frac{1}{f_s}$. The gate voltage varies between -1.54 V and -2.14 V. Fig. 2-21 shows the plots of estimated FRFs and their variance based on the proposed indirect model.

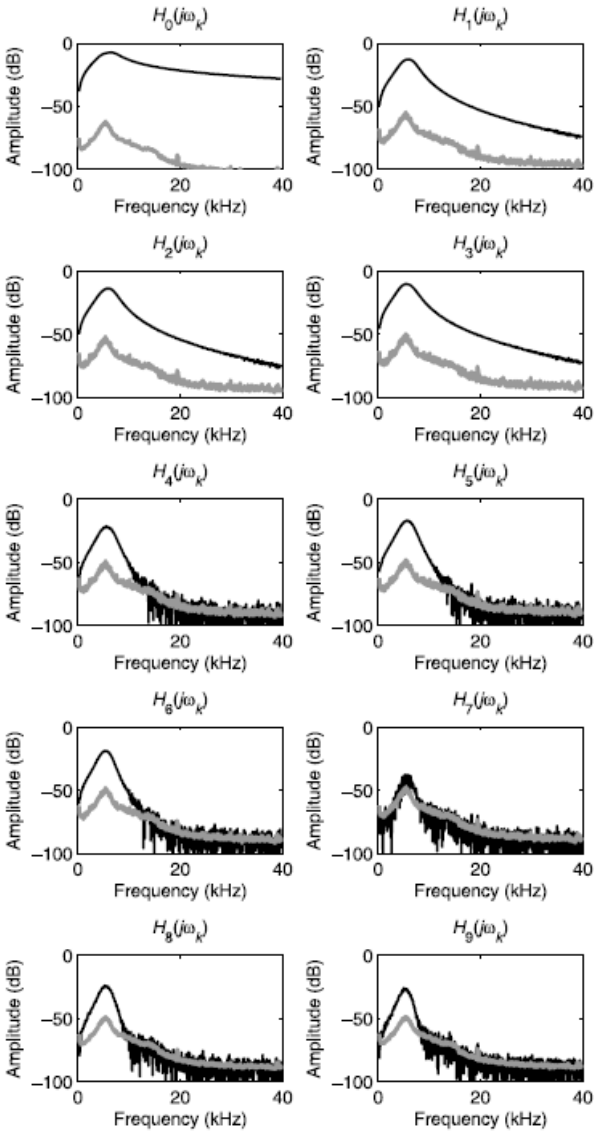

Fig. 2-21. Estimated FRFs $H_r(jw_k)$ (black) and their variance (grey) of the time-varying second-order bandpass filter based on indirect method [36]

2.6 Nonlinearities of Photocurrent

2.6.1 Exponential Linearity

The diode used in the equivalent circuit is to perform the dynamic resistance characteristics across a pn-junction [10]. The exponential diode equation as given by equation (2-2) is voltage dependent and has an exponential relationship between the current and the voltage across the pn-junction. The equation can be further expressed as a voltage-dependent current generator by a Taylor's series expansion [37]:

$$I_d = K(V_{mod}) = K_1 V_{mod} + K_2 V_{mod}^2 + K_3 V_{mod}^3 \tag{2-44}$$

The Taylor's series coefficients are given as

$$K_1 = \frac{1}{R_r} \tag{2-45}$$

$$K_2 = \frac{1}{2 I_d R_r^2} \tag{2-46}$$

$$K_3 = \frac{1}{2 I_d^2 R_r^3} \tag{2-47}$$

where

R_r is the reverse bias resistance across the pn-junction.

2.6.2 PN-Junction Capacitance Nonlinearity

The pn-junction capacitance C_j is a nonlinear function of the applied bias voltage across the pn-junction. C_j is made up of two components, namely the diffusion capacitance C_d, and the depletion capacitance (which is also termed as the transition capacitance) C_t.

The diffusion capacitance C_d is due to the build-up of minority carriers charge around the metallurgical junction as the result of forward biasing the pn-junction. C_d is given by the change in the value of the stored charge ΔQ due to a change in either the forward current or forward voltage ΔV as given by equation (2-48) [38], [39].

$$C_d = \frac{\Delta Q}{\Delta V} = K_d \cdot I_{df} = K_d \cdot I_{s0} \cdot e^{\left(\frac{V_s}{n_d \cdot V_t}\right)} \tag{2-48}$$

where

K_d is the constant at a given temperature

$I_{df} = I_{s0} \cdot e^{(\frac{V_s}{n_d \cdot V_t})}$ is the forward-biased diode current

I_s is the reverse saturation current or leakage current

$n_d \approx 1 - 2$ is the diode Ideality Factor

V_s is the bias voltage of the pn-junction; $V_s = V_{mod}$ in this case

$V_t = \frac{k \cdot T}{q}$ is the thermal voltage

k is the Boltzmann's constant

T is the junction temperature in Kelvin

q is the electronic charge

Fig. 2-22 shows the plot of diffusion capacitance as a function of biasing voltage from -0.6 V to 1 V across the pn-junction. The plot is generated with I_s = 0.1 fF, n_d = 2, K_d = 1000 µF/A at room temperature T at 300 K.

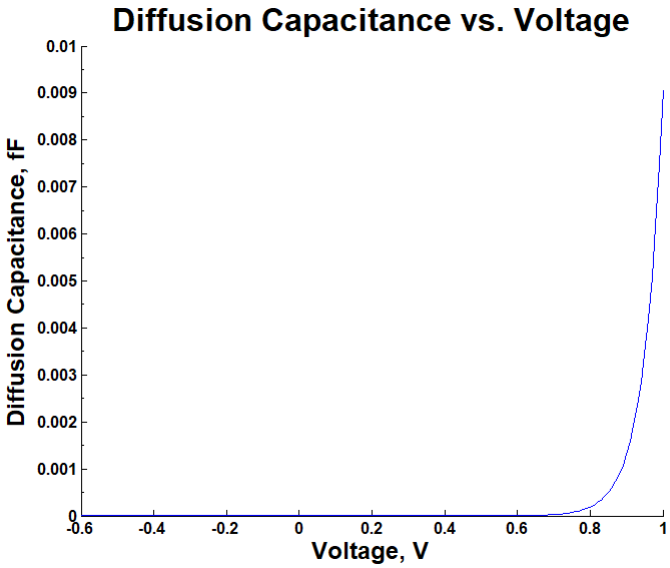

Fig. 2-22. Diffusion capacitance as a function of biasing voltage across the pn-junction

When a reverse bias is applied, mobile charge carriers move away from the metallurgical junction leaving behind immobile ions (negative ions in the p-region and positive ions in the n-region). This gives rise to space charge separation across the junction. In depletion region, the electric charges due to immobile positive and negative ions do not move from one place to another place. Instead, they exert electric field or electric force resulting in charge stored at the depletion region in the form of electric field. Thus, there exists a capacitance at the depletion region. C_t can be generally expressed as [38], [39]:

$$C_t = \frac{C_{j0}}{(1-\frac{V_s}{V_{bi}})^m} \tag{2-49}$$

$$V_{bi} = V_t \cdot \ln(\frac{N_A \cdot N_D}{n_i}) \tag{2-50}$$

where

C_{j0} is the zero-bias zero-biased junction capacitance when $V_s = 0$

m is the junction gradient coefficient; $\frac{1}{3} \leq m \leq \frac{1}{2}$, $m = \frac{1}{3}$ for linearly graded junction; $m = \frac{1}{2}$ for step junction

V_s is the bias voltage of the pn-junction; $V_s = V_{mod}$ in this case

V_{bi} is the built-in contact potential barrier across the pn-junction

$V_t = \frac{k \cdot T}{q}$ is the thermal voltage

N_A is the acceptor concentration

N_D is the donor concentration

n_i is the intrinsic carrier concentration

To account for the discontinuity when $V_s = V_{bi}$, P. Van Halen [40] derived an expression for the depletion capacitance as shown in (2-51) which this work will be based on.

$$C_t = \frac{C_{j0}}{[1-\frac{V_s}{V_{bi}}+\frac{V_t}{2 \cdot V_{bi}} \cdot e^{\left(\frac{V_s - V_{bi}}{V_t}\right)}]^m} \tag{2-51}$$

Fig. 2-23 shows the plot of depletion capacitance as a function of biasing voltage from -10 V to 0.6 V across the pn-junction. The plot is generated with C_{j0} = 0.1 fF, V_{bi} = 0.65 V, $m = \frac{1}{3}$ (for linearly graded junction) at room temperature T at 300 K.

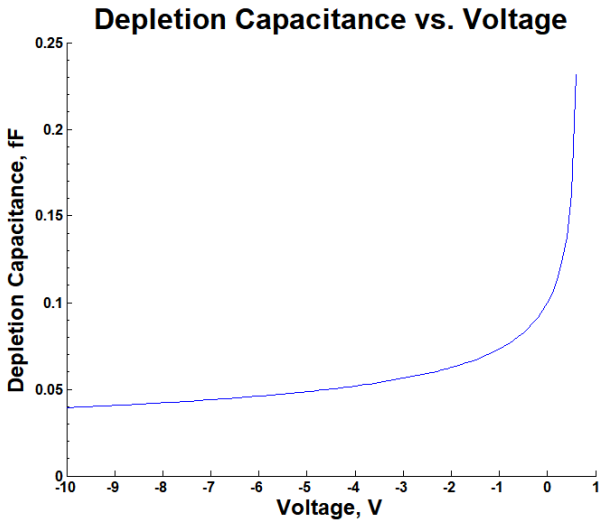

Fig. 2-23. Depletion capacitance as a function of biasing voltage across the pn-junction

C_t increases with the area of pn-junction but decreases with the depth of depletion layer. Hence, photo devices with smaller active area are inherently having faster response time due to smaller junction capacitance. As depth of depletion layer increases with the applied reverse bias, the junction capacitance is commonly specified at zero external bias. Excessive reverse bias to photodiodes may cause device breakdown and degraded performance. Any applied reverse bias must be kept lower than the maximum rated value.

When the pn-junction is in forward bias mode, C_d is much larger than C_t. Hence, diffusion capacitance is only considered in forward biased diode. On the other hand, in the reverse biased mode, C_t is the dominant component as for the case of normal lighting sensing mode of photo devices.

2.6.3 Wire Inductive Nonlinearity

Wires are used to make contact with the photovoltaic cell and the measurement circuit. The inductive effect produces current which is a nonlinear function of voltage and frequency dependent. The current generator can be represented as $g(V_{load}, V_{load} - V_{mod})$ which is derived as follows:

$$I_{load} = \frac{V_{mod} - V_{load}}{R_s + R_p + sL_s}$$

$$= \left(\frac{(R_s + R_p) - sL_s}{(R_s + R_p)^2 + L_s^2}\right)(V_{mod} - V_{load}) \quad (2\text{-}52)$$

CHAPTER 3 PROPOSED MEASUREMENT METHODOLOGY

3.1 Proposed Approach

Best linear approximation (BLA) is introduced as the technique to approximate the behaviour of the nonlinear system. A system that can be represented by a Volterra series expansion will have average spectrum given by BLA if the excitation is Gaussian or any equivalent random excitation of sufficiently long excitation. Fig. 3-1 illustrates the concept of introducing noise as an excitation source to a nonlinear system to estimate the BLA of its transfer function. The BLA of the nonlinear system resembles the behavior of a linear system with the nonlinearities represented by an additive noise source. Fast Fourier Transform (FFT) is performed on the input and output signals in order to determine the frequency response function function (FRF). The residues or errors in the approximation is quantified by the use of standard deviation statistic.

Fig. 3-1. Illustration of noise excited BLA of nonlinear system

The aim of this work is not on using BLA technique for the purpose of system identification of nonlinear system. Rather, the BLA technique is adopted in a way to sort out the noise components of the system response. The output noise is then quantified by measuring the dispersion of the BLA values as outlined in Fig. 3-2. The measured standard deviation can then be used as an indirect gauge of the relative strength of the output signal.

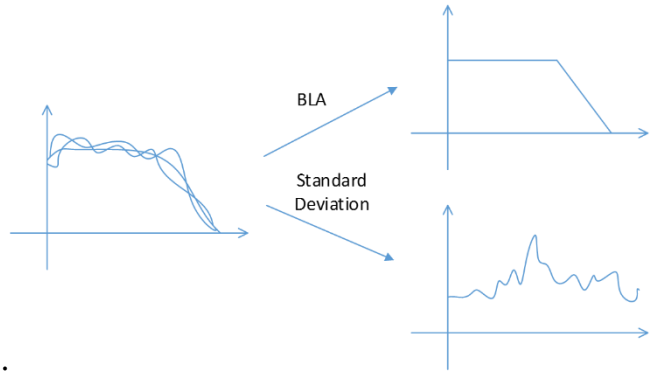

.

Fig. 3-2. Separation of system's BLA and its dispersion

The BLA is obtained by averaging 1000 points of FRF values in this research. The equivalent moving average is in fact a simple low pass Finite Impulse Response (FIR) filter. The

illustration is using the transfer function of a low pass filter function. In fact, transfer functions of any other discrete filters can be used for the illustration. Fig. 3-3 shows the frequency response function of a 1000-point moving average filter as compared to different types of low pass Infinite Impulse Response (IIR) filters, namely 5-order Butterworth, 5-order Chebyshev Type I & II, and Elliptic filter. Table 3-1. Characteristics of low pass filters for comparisonTable 3-1 provides the characteristics of those filters used for the comparison in this case.

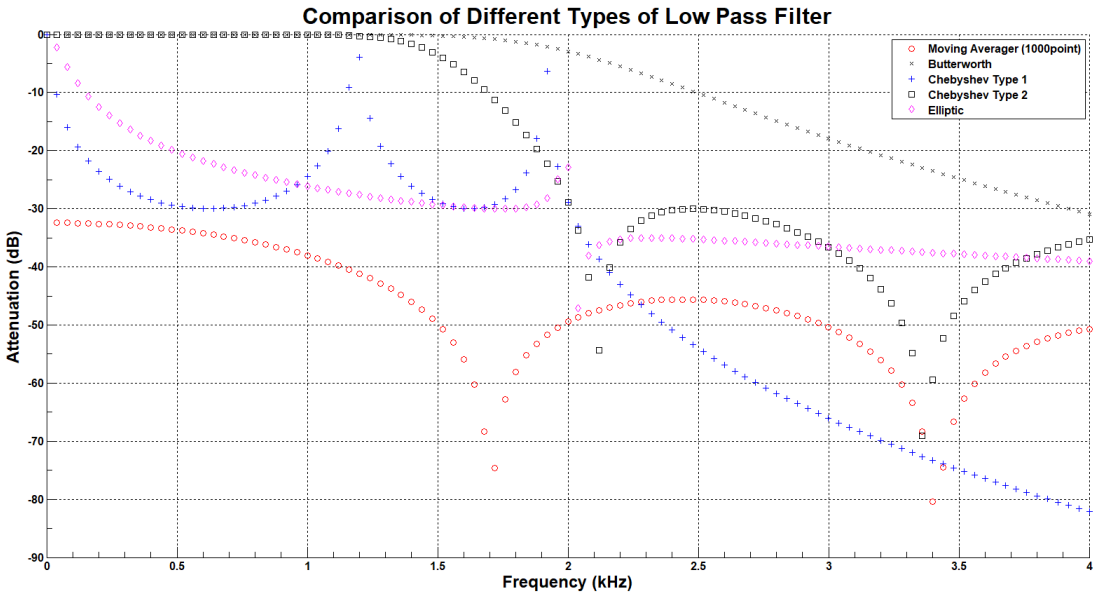

Fig. 3-3. Frequency plots of different types of low pass filters

Table 3-1. Characteristics of low pass filters for comparison

Type of Low Pass Filter	Order	Cut-off Frequency (Hz)	Passband Ripple (dB)	Stopband Attenuation (dB)
Moving Averager	1000-point	-	-	-
Butterworth	5	2010	30	-
Chebyshev Type I	5	2010	30	-
Chebyshev Type II	5	2010	-	30
Elliptic	5	2010	30	35

The idea here is that there are errors associated with the nonlinear system which can't be completely modelled by the ideal transfer function as for the case of linear system. These errors are being exploited in this research as a gauge to the strength of the sensor's signal under investigation. In this work, either random phase multisine with constant amplitude but

random phase or white Gaussian noise is used as the excitation signal source to the nonlinear system under study.

3.2 Best Linear Approximation

3.2.1 Linear Approximation

Linear models have been successfully applied to a wide range of modeling problems albeit with restrictive assumptions. Linear approximation offers the advantages of useful models that enable the application of many existing design techniques, and provide users with intuitive insights into the problem made mostly difficult and complicated with nonlinear modeling. For these reasons, linear approximation can be applied to a nonlinear system by choosing the operating range close to a particular approximating point as shown in Fig. 3-4 where *L(x)* is the linear approximation to the nonlinear function *f(x)* at approximating point *a* in simple Mathematical expression. x_1 is an input point close to the approximating point *a*. Based on this concept, a generalized linear framework can thus be developed for use in a nonlinear environment by sorting out non-linear distortions.

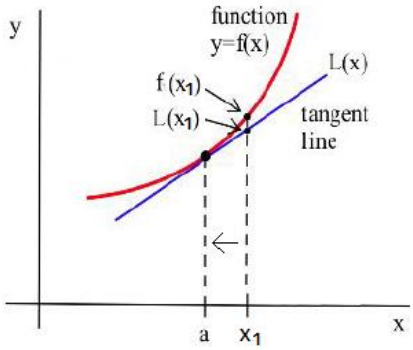

Fig. 3-4. Graphical illustration of linear approximation

3.2.2 Best Linear Approximation

Best Linear Approximation (BLA) is a framework to deal with non-linear distortions in a linear modeling framework. BLA minimizes the mean square error between the measured output and the modelled output for a particular class of inputs as given by equation (3-1).

$$G_{BLA} = \min E[y(t) - G(a) \cdot u(t)]^2 \tag{3-1}$$

where *y(t)* and *u(t)* are the measured output and input respectively, *G(a)* is the linear transfer function model and *a* is the shift operator.

Equation (3-1) is in fact equivalent to the classical FRF measurement based on cross-power and auto-power spectra measurements [41] as given by equation (3-2).

$$G_{BLA}(\Omega) = \frac{S_{YU}(\Omega)}{S_{UU}(\Omega)} \tag{3-2}$$

where $S_{YU}(\Omega)$ is the cross-power spectrum between the output y and the input u, $S_{UU}(\Omega)$ is the auto-spectrum of the input u, and Ω stands for discrete ($\Omega = e^{-\frac{jw}{fs}} = e^{-\frac{j2\pi f}{fs}}$) or continuous time $\Omega = j\omega = j2\pi f$ frequency.

A nonlinear system can thus always be represented by its best linear approximation G_{BLA} followed by a noise source representing the nonlinear contributions of the system as shown in Fig. 3-5 [42].

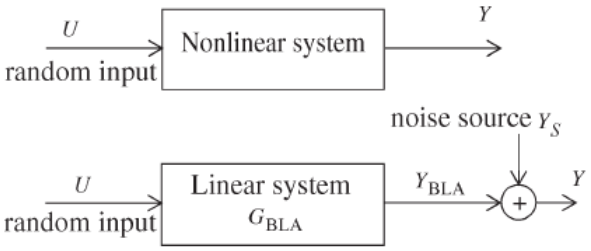

Fig. 3-5. Representation of a non-linear system by a linear system for a random input [43]

Signal $Y_{BLA}(t)$ in Fig. 3-5 captures the part of $y(t)$ that can be described by the best linear approximation G_{BLA} as shown in equation (3-2). The nonlinear noise source with power spectrum $S_{Ys}(\Omega)$ captures all the remaining errors (a.k.a. "stochastic nonlinearities") as shown in equation (3-3).

$$Y(\Omega) = Y_{BLA}(\Omega) + Y_S(\Omega) = G_{BLA}(\Omega) \cdot U(\Omega) + Y_S(\Omega) \tag{3-3}$$

Y_{BLA} is not correlated with Y_S although it is no independent of Y_s. The nonlinear contributions depend on the particular realization of the input signal $U(\Omega)$, and exhibit stochastic behaviour if the input signal $U(\Omega)$ is a random process. $G_{BLA}(\Omega)$ can be estimated by averaging the measured FRFs for different input excitations. For Gaussian noise excitation, $G_{BLA}(\Omega)$ and $S_{Ys}(\Omega)$ are completely determined by the auto-power spectrum of the input $S_{UU}(\Omega)$.

3.2.3 Classification of Random Signals

BLA depends upon the time domain characteristic (power distribution, e.g., normally, binary or uniformly distributed) and frequency domain characteristic (amplitude spectrum) of the excitation signals. To measure the linear system, we would normally apply an excitation source and determine the response of the system to the excitation. The excitation source can be as dedicated as multisine source with random phase to excite the system at certain user-specified frequencies, or as simple as a normally distributed noise source.

3.2.3.1 Random Phase Multisine

A random phase multisine is a periodic broadband signal comprising of a sum of cosines with harmonically related frequencies, each with either constant or random amplitude A_k but a random phase ϕ_k as indicated by (3-4).

$$u(t) = \sum_{k=1}^{N} A_k \cos\left(2\pi \frac{f}{N} kt + \phi_k\right) \tag{3-4}$$

Period of the signal is given by $T = 1/f$. Amplitudes, A_k, of the (co-)sines and the base frequency $f_o = \frac{f}{N}$ can be chosen arbitrarily while phases ϕ_k are usually selected to minimize the crest factor. The phases ϕ_k are independent random variables such that $E\{e^{j\phi_k}\} = 0$. This condition is satisfied when ϕ_k is uniformly distributed over [0, 2π). Theoretically, the number of frequencies N should approach infinity in order for a random multisine to become Gaussian. However, in practice, N > 20 is sufficient for smoothly varying amplitude distributions A_k [42], [43].

In [42] is shown that the classification of the nonlinearities into odd and even order is possible by carefully selecting the grid of excitation signals. If odd multisine is used to excite only odd lines, even nonlinearities will always transfer power to the even frequency bins while odd nonlinearities transfer power to the odd frequency bins according to:

$$f_{x,odd} + f_{y,odd} = f_{x+y,even} \tag{3-5}$$

$$f_{x,odd} + f_{y,odd} + f_{z,odd} = f_{x+y+z,odd} \tag{3-6}$$

In the generation of random phase multisine for this work, the excitation frequency is varied from 10 Hz to 2010 Hz with a step size of 80 Hz and number of frequencies N set to 25. Fig. 3-6 shows the simulated normalised time-domain plot and spectrum of a random phase multi-sine with constant amplitude excitation signal using equation (3-4) in Matlab.

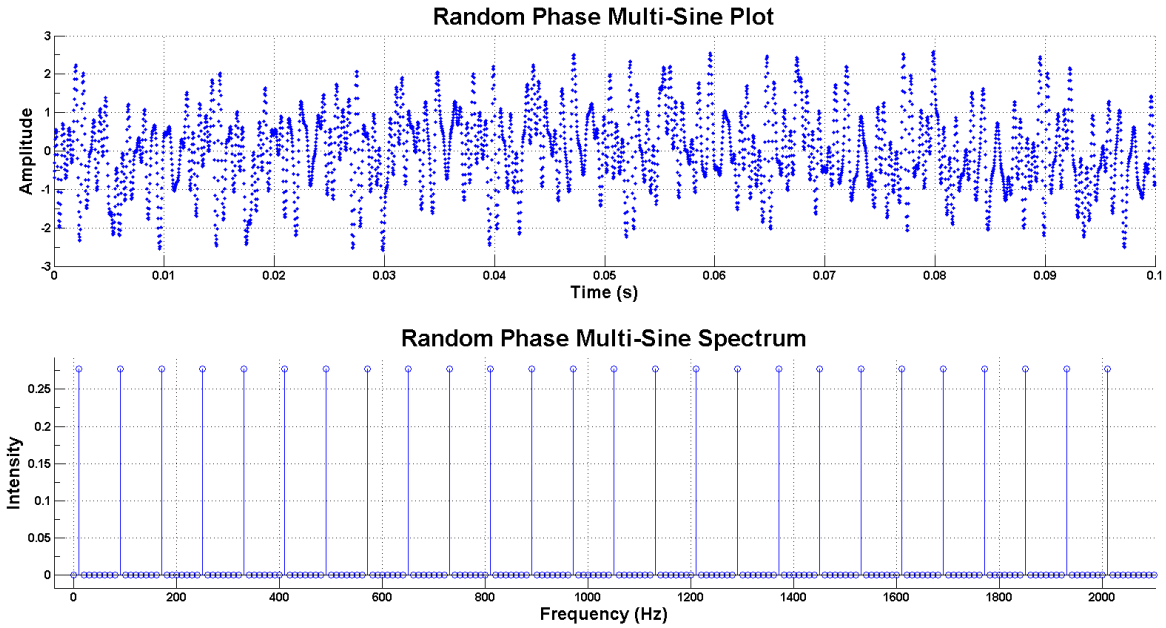

Fig. 3-6. Time domain and spectrum of random phase multisine excitation signal

A lower variance is obtained for BLA without affecting its value when using random odd multisines as the excitation signals. This is because even nonlinearities result in stochastic contribution on both the even and odd frequency lines which disappear in the averaging process as shown in equation (3-5). The impact of even nonlinearities on FRF measurements is merely a disturbing noise when odd lines of FRFs are measured.

3.2.3.2 Gaussian Noise

Gaussian noise is a statistical noise with a probability density function (PDF) equal to that of a normal distribution, also known as the Gaussian distribution. A Gaussian noise *u(t)* can be generated using a pseudo-random number generator as shown in (3-7).

$$u(t) = Offset + \sum_{k=1}^{N} A_k \cdot r_k \tag{3-7}$$

where r_k is a pseudo random number between 0 and 1, and A_k is the signal's amplitude. *Offset* is the dc offset from 0 V. Fig. 3-7 shows the simulated normalised time-domain plot and spectrum of Gaussian excitation signal in frequency domain using equation (3-7) in Matlab.

As can be seen from Fig. 3-7(b), an ideal Gaussian noise source has a flat spectrum in frequency domain where every frequency band is equally excited with excitation strength distributed according to the Gaussian distribution.

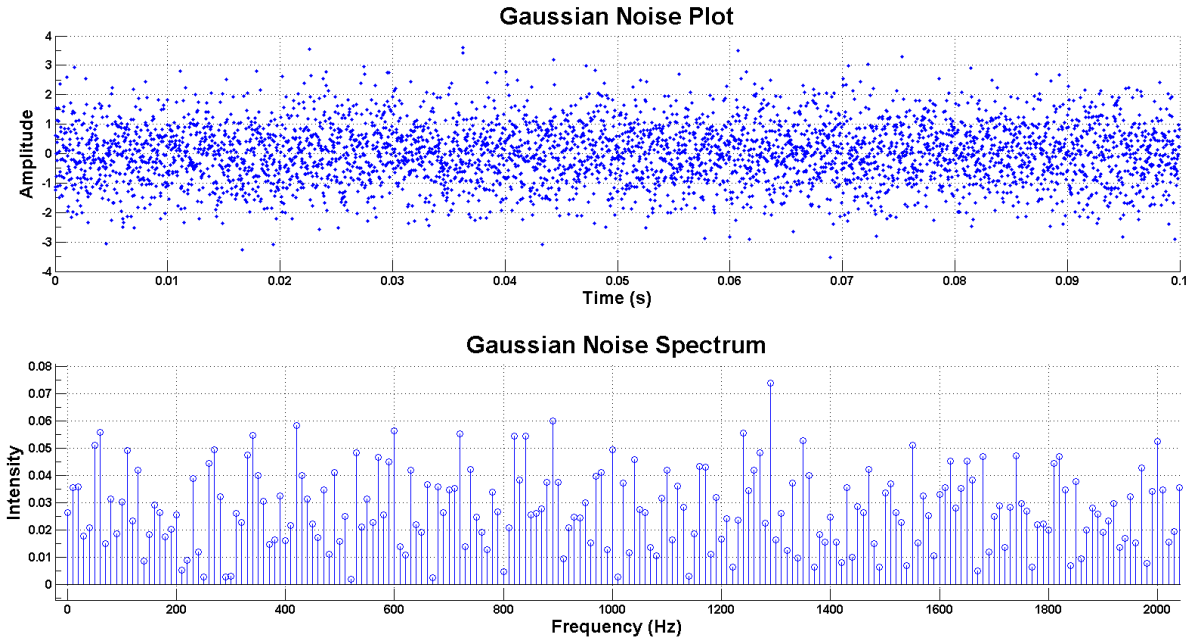

Fig. 3-7. Time domain and spectrum of Gaussian noise excitation signal

3.2.4 Measuring the Best Linear Approximation

In [42], the BLA has been carried out with normally distributed signals with a user-specified amplitude spectrum. There is no restriction of the generality of the approach. It is no problem at all to generate random multi-sines with a user-specified amplitude distribution and amplitude spectrum [44].

A straightforward approach to measure the linear system would be to apply a normally distributed noise excitation with a user specified power spectrum and to average this result over a large number of realizations of the input signal using the classical correlation methods [41] as shown in equation (3-8).

$$G(j\omega_k) = \frac{S_{YU}(j\omega_k)}{S_{UU}(j\omega_k)} \tag{3-8}$$

Although this approach converges to the best linear approximation, it is very time consuming [44], [45]. In this research, an alternative approach is performed using the following rules:

Rule 1: Use random phase multisine: As compared to random noise excitations, dips in the amplitude spectrum of the excitation are avoided and the desired amplitude spectrum is obtained in each realization of the signal [46].

Rule 2: Use odd signals that excite only the odd frequencies. This excludes the impact of even nonlinear distortions. These do not disturb the odd frequencies that are used to measure the linear approximation.

For periodic excitations such as random phase multisine, the frequency response function (FRF, $G(j\omega_k)$) is obtained by simple division of the output by the input spectrum [25] as shown in (3-9). However, in this research, the same measurement technique also applies to Gaussian noise excitation as a comparison to the case of using random phase multisine excitation.

$$G(j\omega_k) = \frac{Y(j\omega_k)}{U(j\omega_k)} \tag{3-9}$$

3.2.5 Measurement Circuit

The measurement circuit is basically comprised of a simple RC photodetector connected to an optical current source, e.g. a photovoltaic cell, as outlined in Fig. 3-8.

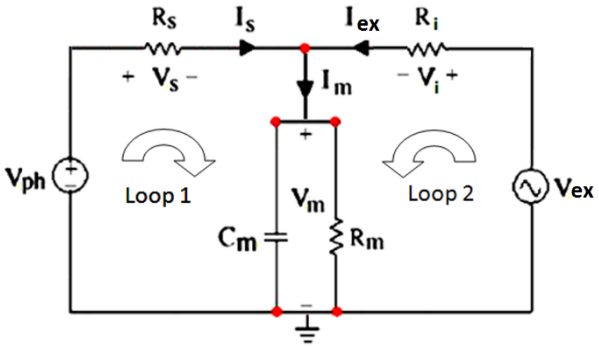

Fig. 3-8. BLA measurement circuit

V_{ph} represents the equivalent voltage generated by optical current source due to illumination. V_{ph} can be obtained from the optical current I_{ph} and the source resistance R_s by applying

source transformation. An excitation voltage source V_{ex} is connected across the output terminals of the circuit to provide either random phase multisine or Gaussian noise excitation signal to the circuit. I_{ex} is the current from the excitation voltage source, I_m is the output current of the RC network.

By applying KVL at loop 1 & 2, and KCL at the output node of the circuit, it can be shown that the output voltage of the circuit, V_m is governed by the differential equation as given by equation (3-10).

. $$A \cdot \frac{dV_m}{dV_t} + B \cdot V_m - C = 0 \tag{3-10}$$

where

$$A = R_i \cdot R_s \cdot R_m \cdot C_m$$

$$B = R_m \cdot (R_i + R_s) + R_i \cdot R_s$$

$$C = R_m \cdot (R_i \cdot V_{ph} + R_s \cdot V_{ex})$$

The BLA of the transfer function can be obtained non-parametrically by performing classical FRF measurement of the measurement circuit, i.e. the frequency domain of the output voltage I_m over the frequency domain of input excitation voltage V_{ex}.as a function of the photocurrent I_{ph}. In this case, the non-linear circuit can always be modelled by a linear system followed by a noise source representing the non-linear contributions. By construction, the noise source is uncorrelated but not independent of the excitation signal V_{ex}.

3.3 Methodology Flow

Fig. 3-9 shows the methodology flow chart in which BLA technique is applied to measure photocurrent in frequency domain.

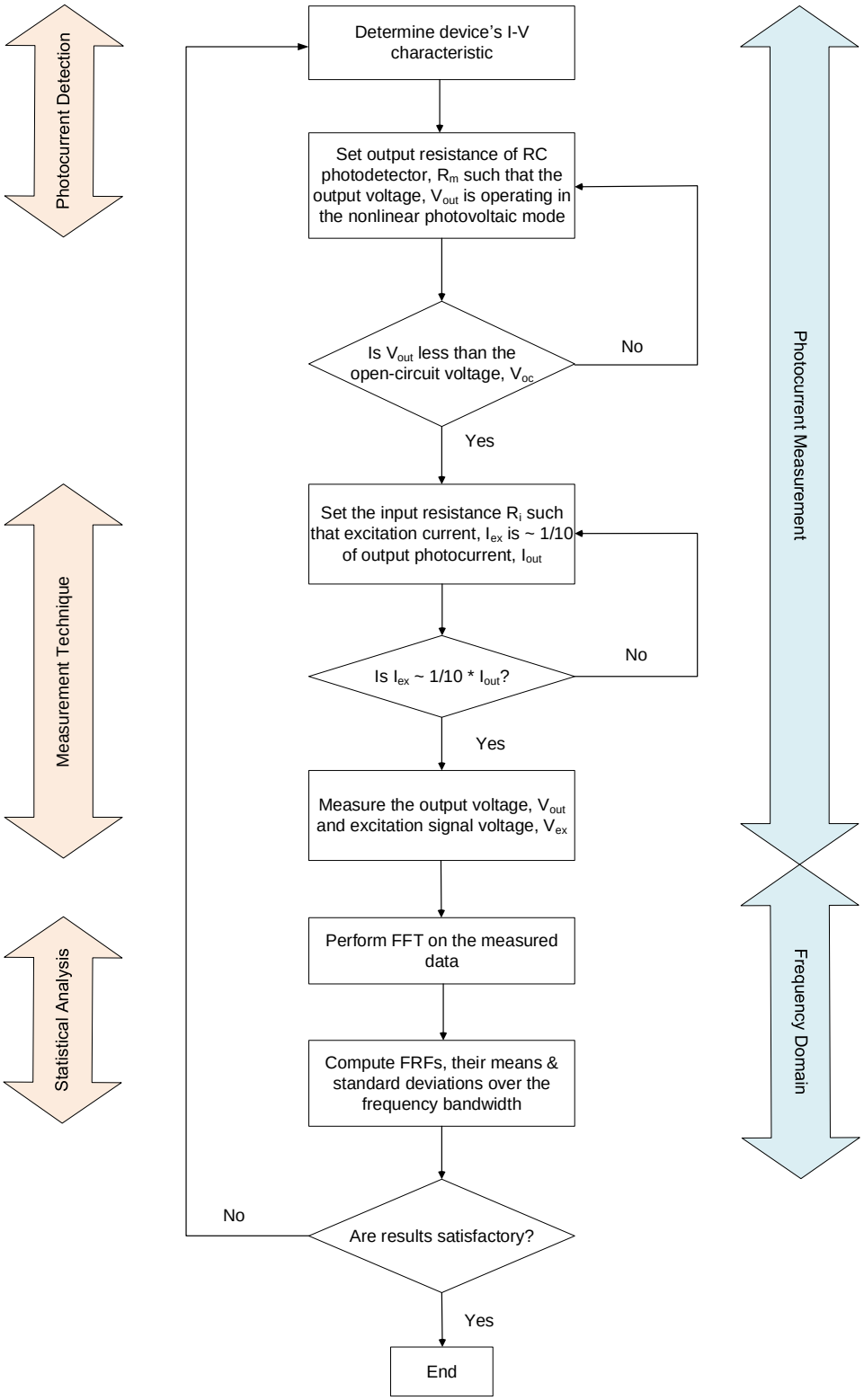

Fig. 3-9. Frequency domain photocurrent measurement methodology flowchart

The first step to the measurement technique is to determine the current-voltage (I-V) curve for the photocurrent device. Based on the expected range of the photocurrent generated by the device, e.g. a PV cell, the output resistance, R_m needs to be set accordingly such that the output voltage, V_{out}, is operating in the photovoltaic mode, i.e. below the open-circuit voltage, V_{oc}, which is the maximum voltage from a PV cell when the photocurrent generated by the PV cell is zero. This means to select an output voltage which is close to the PV cell's maximum power point as shown in Fig. 3-10. In this region, the I-V characteristic is exponentially nonlinear and yet it is below V_{oc}.

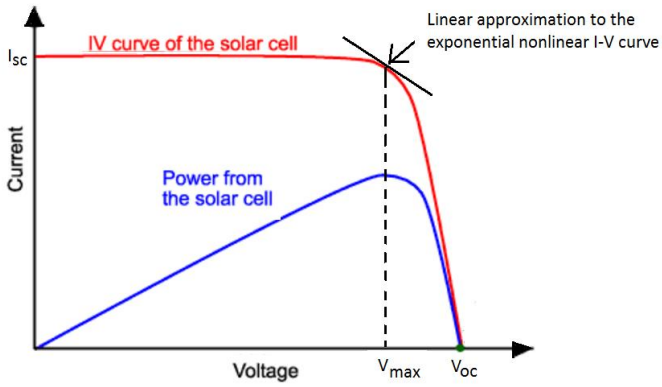

Fig. 3-10. Operation of the PV cell near the maximum power point

The input resistance of the RC photodetector, R_i needs to be set such that I_{ex} is scaled down to only ~ $\frac{1}{10}$ the strength of the output photocurrent, I_{out}. I_{ex} needs to be weak as compared to I_{out} so that the irradiance effect on the photocurrent will not be masked by the relatively stronger I_{ex}.

Output voltage of RC photodector V_{out} is measured over a number of iterations, e.g. 1000 times. The measured values are then converted to frequency domain for spectral analysis using FFT.

Results of FRF means and standard deviation across the targeted frequency range are plotted and checked for consistency. If results are not satisfactory, then the whole process is repeated starting with the determination of R_m.

CHAPTER 4 THEORETICAL VALIDATION OF EXPERIMENTAL RESULTS

4.1 Introduction

This chapter serves to explain the development of a simulation model to simulate the measurement circuit. The chapter starts with the section to introduce the modelling of the measurement circuit with the sources of nonlinearities for the measurement circuit. This is followed by the presentation of the simulation results.

4.2 Modelling of Measurement Circuit

Fig. 4-1 shows the proposed equivalent circuit model for the photovoltaic cell coupled with a configurable RC photodetector. This is the complete overall outline of the circuit used in this work for the frequency domain photocurrent measurement.

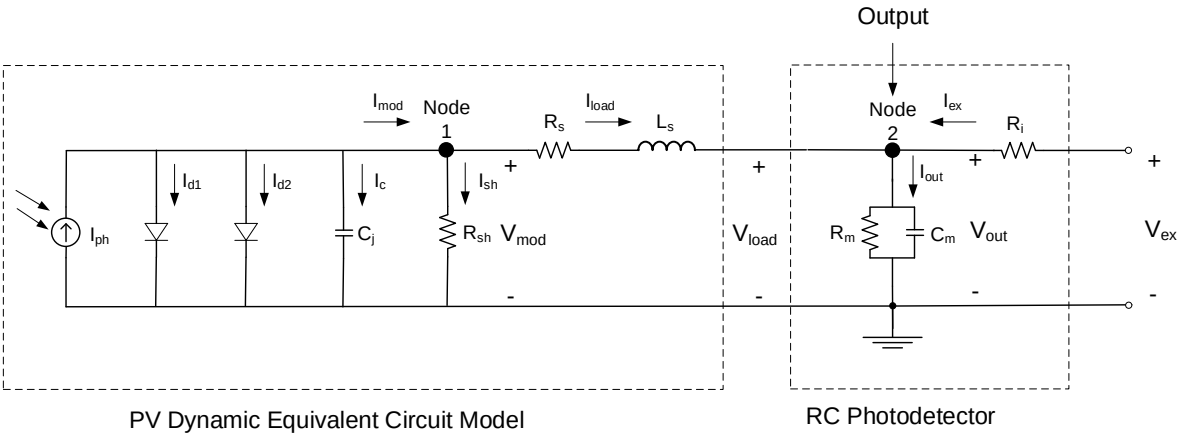

Fig. 4-1. Measurement circuit for frequency domain photocurrent measurement

The measurement circuit has two nodes, namely Node 1 and Node 2 as shown in Fig. 4-1. The nodal voltage is given as $V_1 = V_{mod}$ and $V_2 = V_{out}$ respectively. There are three nonlinearities associated with this measurement circuit, namely exponential nonlinearity between the diode current and the voltage across it, junction capacitance nonlinearity and the nonlinearity due to wiring of photovoltaic cell. These nonlinearities are highlighted in Section 2.6.

4.3 Matlab / Simulink Simulation Model of Measurement Circuit

The equivalent circuit model of PV cell has been created in Simulink using components from Simscape toolbox. A custom Simscape component as shown in Appendix E.1**Error! Reference source not found.** has been created to model the diffusion capacitance arising from the build-up of minority carriers charge surrounding the forward bias pn-junction. The formula for the diffusion capacitance is as given by equation (2-48). Another custom Simscape component as shown in Appendix E.2**Error! Reference source not found.** has been created to model the junction capacitance arising from the space charge region surrounding the reverse bias pn-junction. The formula for the depletion capacitance is as given by equation (2-49). Fig. 4-2 shows the I-V characteristics while Fig. 4-3 shows the corresponding P-V characteristics of the pn-junction making use of the custom Simscape model for the diffusion and depletion capacitance.

In this work, as a first cut approach, the C_{j0} is assigned a value of 0.1 fF. The junction of the PV cell is assumed to be linearly graded with m assigned to 0.33. Fig. 4-4 shows the complete simulation model of the measurement circuit with the junction capacitance C_j added to it. The parameters for the model are set via a Matlab script file as shown in Appendix E.3**Error! Reference source not found.**. The parallel resistance R_{sh} is set to 10 kΩ while the series resistance R_s is set to 10 Ω. The components of RC photodetector are set to same values as used on the bench set-up with source resistance R_p = 1 Ω, output resistance R_m = 4.7 kΩ and output capacitance C_m = 1 µF. The current is set to 20 µA to simulate the case of the measurement circuit with a Gaussian noise excitation and an irradiance conditions that produces short-circuit current of 20 µA from the OPV cell.

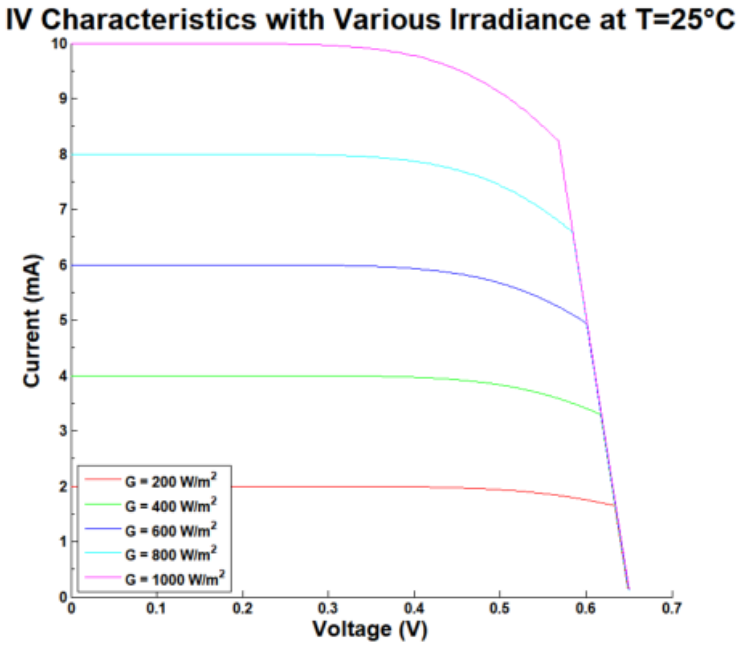

Fig. 4-2. IV characteristics of the pn-junction using the custom Simscape models for diffusion and depletion capacitance

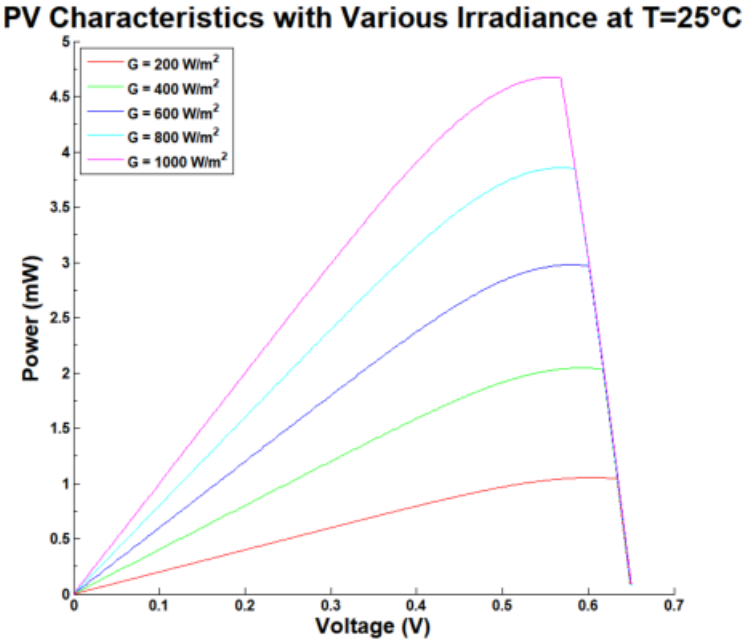

Fig. 4-3. PV characteristics of the pn-junction using the custom Simscape models for diffusion and depletion capacitance

Filename: .\Monash\Research\Test\Simulation\Matlab\Circuit Analysis\pv_nonlinearity_sim_new.slx

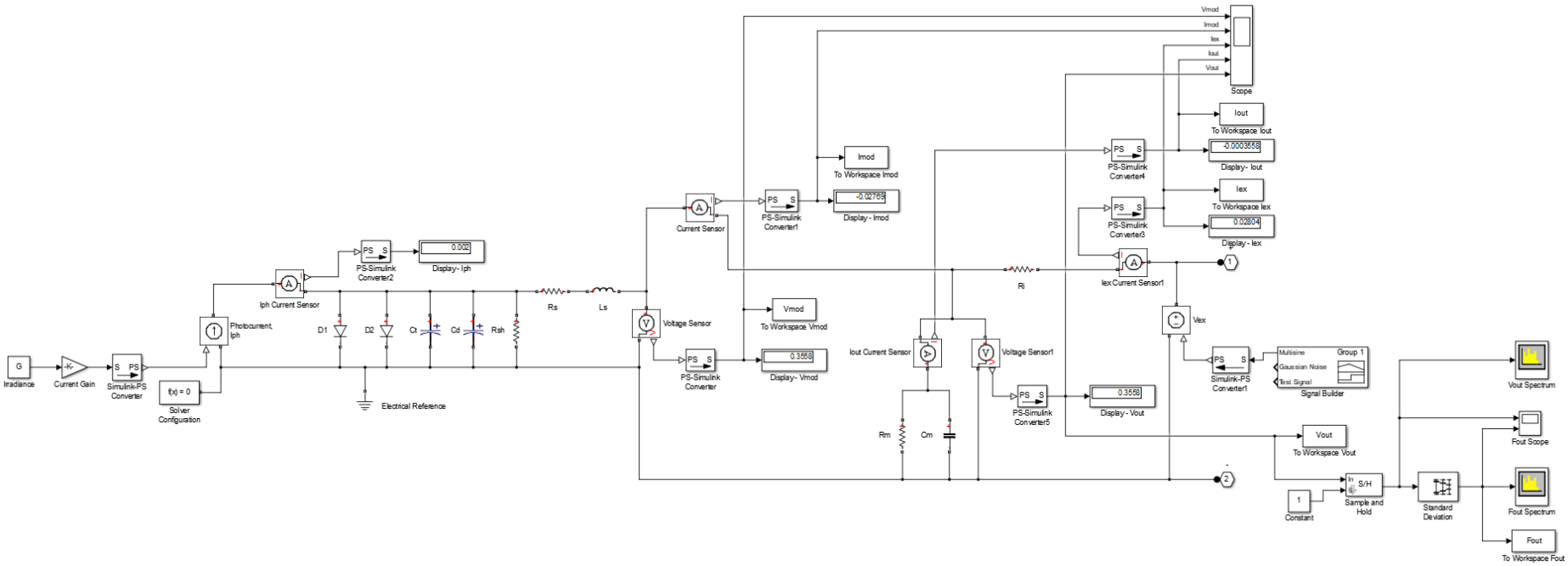

Fig. 4-4. Simulink simulation model of the PV equivalent circuit with RC photodetector for measuring the photocurrent in frequency domain

The junction capacitance C_j which comprises of both the diffusion capacitance C_d and depletion capacitance C_t can be seen to form a parallel-series RLC resonant circuit with the shunt resistance R_{sh}, the series combination of series resistance R_s, wire inductance L_s, resistance R_m and capacitance C_m of the RC photodetector as shown in Fig. 4-5.

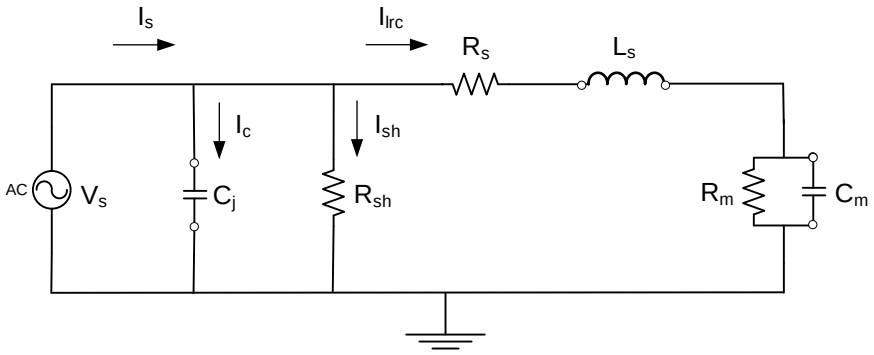

Fig. 4-5. Generic equivalent circuit model of a parallel-series RLC circuit

With an ac voltage source V_s connected to the RLC circuit, the current response I_s of the circuit can be determined as

$$\begin{aligned} I_s &= I_c + I_{sh} + I_{lrc} \\ &= \frac{V_s}{X_{C_j}} + \frac{V_s}{R_{sh}} + \frac{V_s}{R_s + X_{L_s} + X_{C_m} // R_m} \\ &= V_s \cdot Y \end{aligned}$$

where

$$\begin{aligned} \text{Admittance, } Y &= \frac{1}{X_{C_j}} + \frac{1}{R_{sh}} + \frac{1}{R_s + X_{L_s} + X_{C_m} // R_m} \\ &= jwC_j + \frac{1}{R_{sh}} + \frac{1}{R_s + jwL_s + \frac{1}{jwC_m} // R_m} \end{aligned} \tag{4-1}$$

When the frequency of the ac voltage source is low (close to dc, $\omega \to 0$), reactance due to the junction capacitance $\frac{1}{jwC_j}$ and the capacitance $\frac{1}{jwC_m}$ of the RC photodetector can be considered large while reactance of the wire inductance $j\omega L_s$ is almost zero (i.e. short-circuit). We have an equivalent circuit as shown in Fig. 4-6.

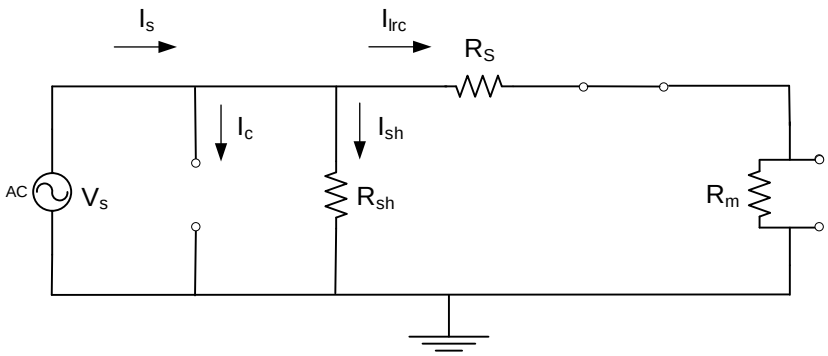

Fig. 4-6. Equivalent circuit model of a parallel-series RLC circuit at low frequency (close to dc)

On the other hand, when the frequency of the ac voltage source is high (close to infinity, $\omega \rightarrow \infty$), reactance due to the junction capacitance $\frac{1}{jwC_j}$ and the capacitance $\frac{1}{jwC_m}$ of the RC photodetector can be considered to be almost zero (i.e. short-circuit) while reactance of the wire inductance $j\omega L_s$ is considered large (i.e. open-circuit). We have an equivalent circuit as shown in Fig. 4-7. In this case, almost zero current will flow from the ac voltage source to the output of the photo device.

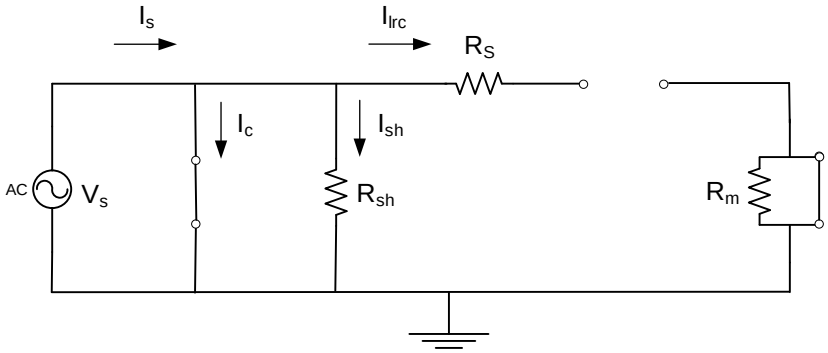

Fig. 4-7. Equivalent circuit model of a parallel-series RLC circuit at high frequency (close to infinity, $\omega \rightarrow \infty$)

4.4 Modelling Simulation Results

Fig. 4-8 shows the simulation results based on the Matlab / Simulink model as shown in Fig. 4-4. In this case, the short-ciruit photocurrent I_{ph} was set to 2 mA. For the RC photodetector, $R_m = 1\ k\Omega$ and $C_m = 1\ \mu F$. The plot shows that there is a dominant power spectral density (PSD) peak at around 1143 Hz within the frequency spectrum of 1 Hz to 2010 Hz. Other peaks occur at 999 Hz and 843 Hz in this case. This indicates that the simulation model which mimics the actual measurement circuit does indeed capture the presumed inherent

circuit nonlinearities and exhibits similar behaviours that help explain the observed trends in the plots of mean and standard deviation of FRF values computed based on measurement data.

Fig. 4-9 shows the simulation results based on the same Matlab / Simulink model and conditions but with Gaussian noise excitation. The plot shows that there is a dominant PSD peak at around 32 Hz within the frequency spectrum of 1 Hz to 2010 Hz. Other peaks happen at 73 Hz and 1576 Hz in this case.

For other simulated PSD plots with different combination values of R_m and C_m for the RC photodetector, refer to figures in Appendix A.1 for those with random phase multisine excitation and Appendix A.2 for those with Gaussian noise excitation. Table 4-1 summarizes the results for simulated plots of FRF standard deviations using the Matlab / Simulink model as shown in Fig. 4-4.

Table 4-1. Summary of results for simulated plots of FRF standard deviations

Excitation Signal	RC Photodetector		Dominant Frequency (Hz)	Other Peak Frequencies (Hz)	Comments
	R_m (Ω)	C_m (F)			
Random Phase Multisine	1k	1µ	1143	999, 843	Fig. 4-11
	10k		694	1583, 1261	Fig. A-1
	100k		1862	1595, 958	Fig. A-2
	1k	1n	883	1781, 1190	Fig. A-3
Gaussian Noise	1k	1µ	32	84, 1578	Fig. 4-12
	10k		42	9	Fig. A-4
	100k		25	55	Fig. A-5
	1k	1n	1342	710, 1183, 486	Fig. A-6

The peaks at different frequencies can be attributed to the interaction of nonlinearities present in the device and measurement circuit with the type of excitation source and RC photodetector, the parameter values used to model the resistances and capacitances associated with the photocurrent device and measurement circuit.

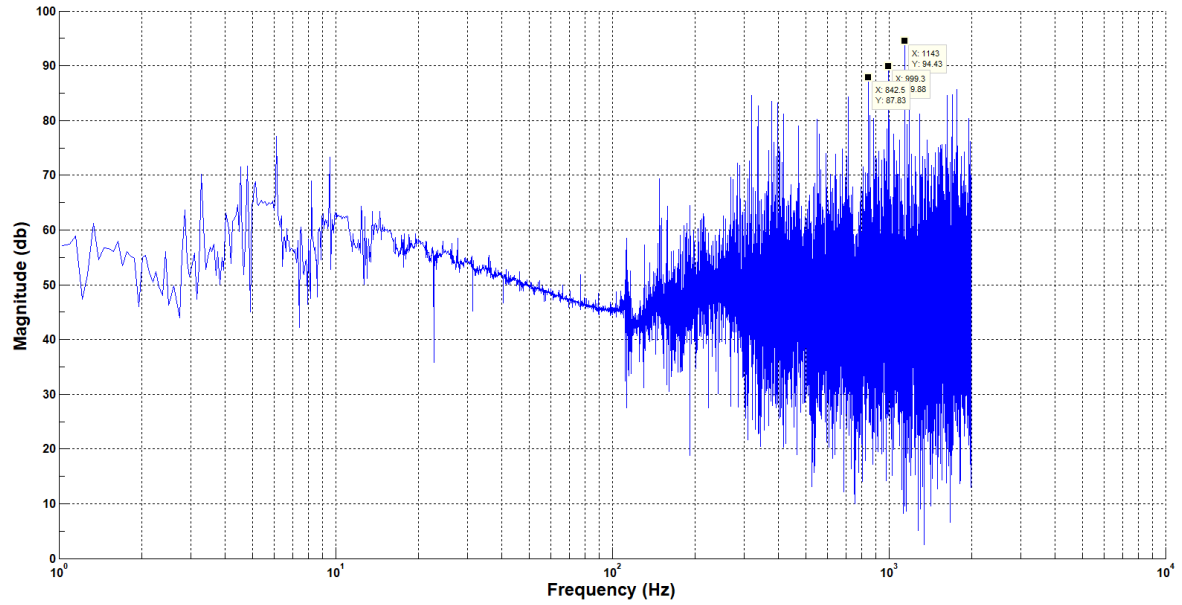

Fig. 4-8. Simulation results of Matlab / Simulink model for $I_{ph} = 2\ mA$ with random phase multisine excitation ($R_m = 1\ k\Omega$ and $C_m = 1\ \mu F$)

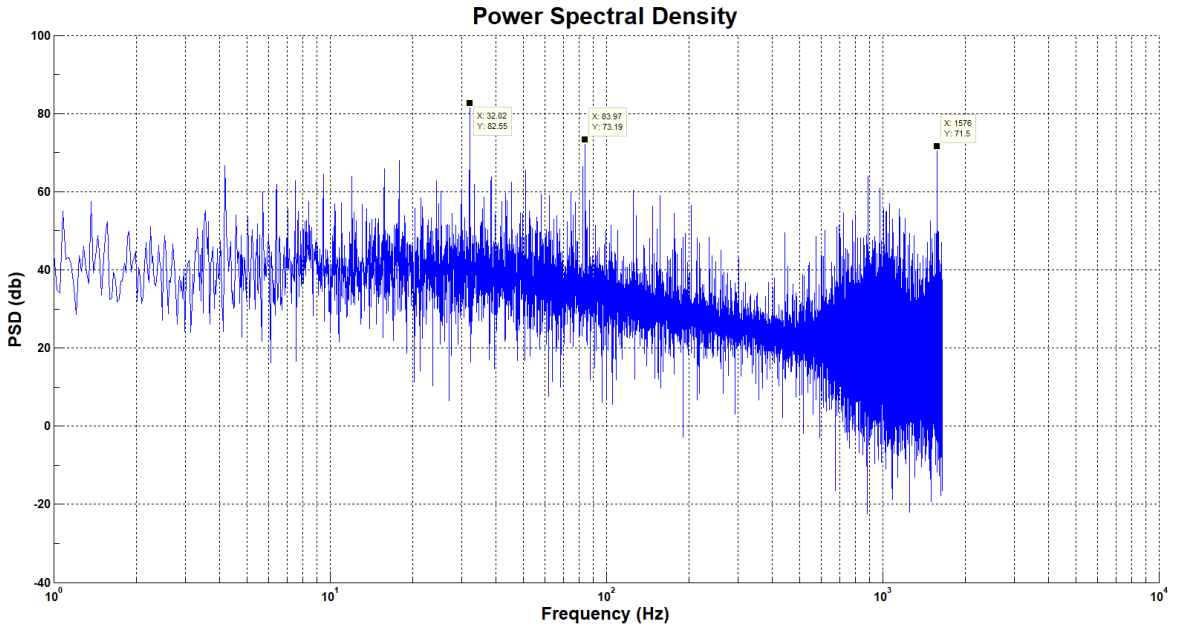

Fig. 4-9. Simulation results of Matlab / Simulink model for $I_{ph} = 2\ mA$ with Gaussian noise excitation ($R_m = 1\ k\Omega$ and $C_m = 1\ \mu F$)

CHAPTER 5 EXPERIMENTAL RESULTS & ANALYSIS

5.1 Experimental Set-up

The validity of the proposed method is independent of the physics of the photocurrent generation. An off-the-shelf solar cell has been used to simulate the behaviour of a generic photosensor. Referring to Fig. 3-8, an excitation voltage source V_{supply} is connected across the output terminals of the circuit to provide an excitation signal to the circuit. I_{out}, is the current supply by the excitation source. I_{out} will interact with E_{ph} (or I_s) through I_m, the current passing through the RC load. The RC load is placed across the sensor to prevent excessive voltage build up across the terminals. R_m is designed to have large resistance value so that it does not create excessive loading condition on the sensor. This measurement configuration allows V_{supply} to excite the sensor while the effective output terminal voltage of the sensor is being measured. Nonlinear response of the sensor with respect to V_{supply} will be reflected indirectly through the measurement of V_m. The current sourcing capability of the sensor becomes a secondary factor under this setup.

The BLA can be obtained non-parametrically by performing classical FRF measurement of the system. FRF is basically the spectrum of the output voltage V_m divided by the spectrum of input excitation voltage V_{ex}. The excitation frequency was varied from 10 Hz to 2.01 kHz with a step size of 20 Hz. The sampling frequency is 40.96 kHz with a record length of 4096 samples.

A test circuit has been constructed as shown in Fig. 5-1 where a photocurrent device in the form of a miniature solar cell, photodiode, etc., has been used to provide photo-generated current I_{ph} when illuminated by LED light bulbs. The test circuit was shielded in a black metal box as shown in Fig. 5-2. The measurements have been carried out using National Instruments PXI-5412 100 MS/s, 14-Bit Arbitrary Waveform Generator (niFgen), and PXI-5112 100 MHz Digital Oscilloscope (niScope). VI programs were developed to generate the excitation signal using PXI-5412. Another VI program was developed to measure the output voltage V_m and excitation voltage V_{supply}. The measurement is averaged across 1000 independent realizations to estimate BLA and associated statistics.

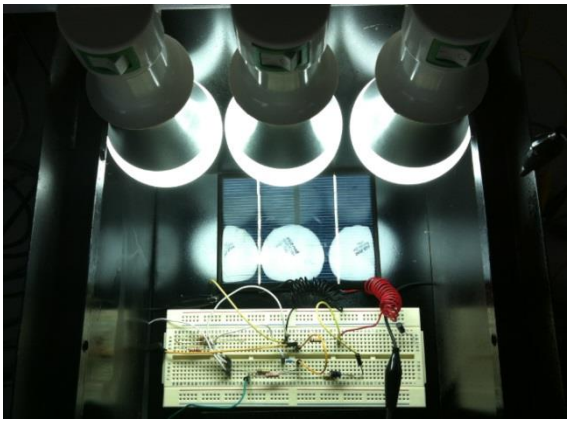

Fig. 5-1. Test circuit for the FRF measurement

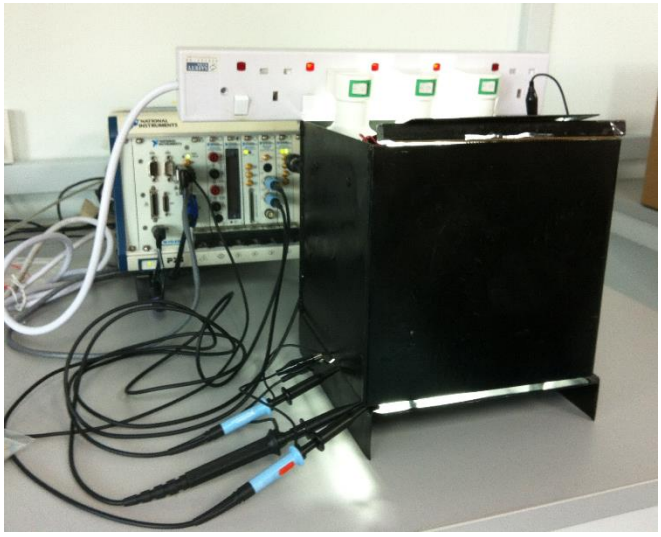

Fig. 5-2. EMI shielding metal box for the FRF measurement

The irradiance I_r for the experiments has been set indirectly by measuring the short-circuit current I_{ph} of the photocurrent device under test conveniently and accurately using a digital multimeter. I_{ph} can be adjusted by controlling the current source coming from the dimmable LED light bulb via a rotary switch. A separate measurement was then carried out using Solarmeter® Digital PV Radiometer to provide the irradiance in $\frac{W}{m^2}$ for each setting of I_{ph} in mA for miniature inorganic photovoltaic cell (Fig. 5-3) and in µA for OPV cell (Fig. 5-4).

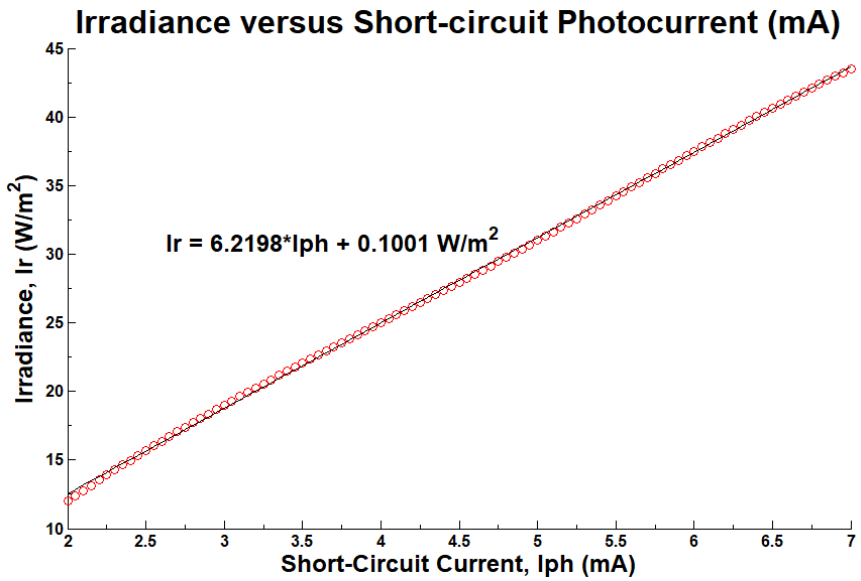

Fig. 5-3. Irradiance I_r as a function of short-circuit current I_{ph} of miniature photovoltaic cell

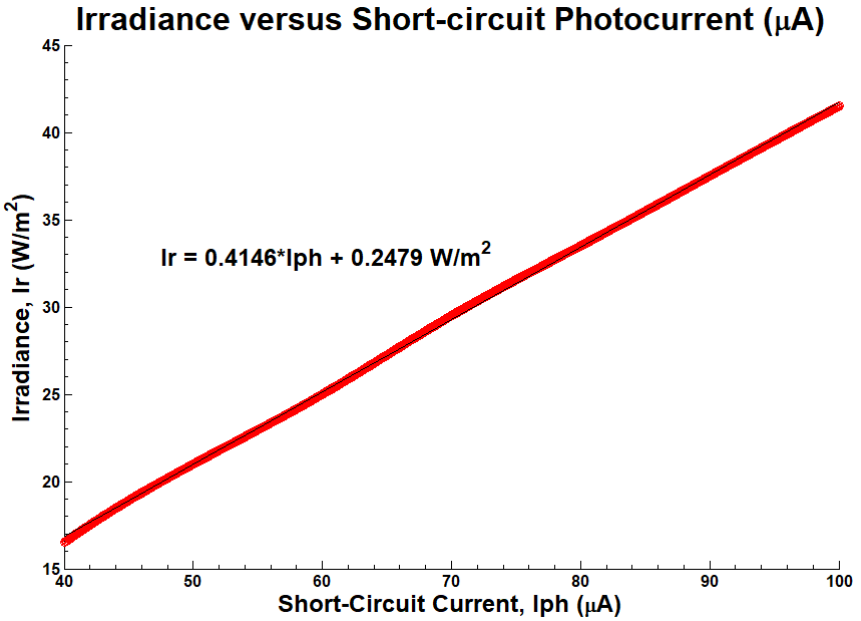

Fig. 5-4. Irradiance I_r as a function of short-circuit current I_{ph} of OPV cell

Fig. 5-3 yields a curve fitted linear equation as in equation (5-1) while Fig. 5-4 yields a curve fitted linear equation as shown in equation (5-1).

$$I_r = 6.2198 \cdot I_{ph} + 0.1001 \ \frac{W}{m^2} \tag{5-1}$$

where I_{ph} in mA

$$I_r = 0.4146 \cdot I_{ph} + 0.2479 \ \frac{W}{m^2} \tag{5-2}$$

where I_{ph} in µA

Based on equation (5-1), a look-up Table 5-1 has been created to provide the corresponding I_r value in $\frac{W}{m^2}$ for each setting of I_{ph}. Similarly, based on equation (5-2), a look-up Table 5-2 has been created to provide the corresponding I_r value in $\frac{W}{m^2}$ for each setting of I_{ph} for OPV cell.

Table 5-1. Look-up Table for I_{ph} versus I_r for miniature photovoltaic cell

Short-circuit Current, I_{ph} (mA)	Irradiance, I_r (W/m^2)
2	12.5
3	18.8
4	25.0
5	31.2
6	37.4
7	43.6
8	49.9
9	56.1
10	62.3

Table 5-2. Look-up Table for I_{ph} versus I_r for OPV cell

Short-circuit Current, I_{ph} (µA)	Irradiance, I_r (W/m^2)
20	8.5
30	12.7
40	16.8
50	21.0
60	25.1
70	29.3
80	33.4
90	37.6

5.2 Miniature Inorganic Photovoltaic Cell

5.2.1 I-V Characteristic

A miniature inorganic photovoltaic cell is used as one of the photocurrent devices under the BLA experiments. Fig. 5-5 shows the I-V plot for the miniature inorganic photovoltaic cell with the terminal voltages biased from -5 V to 2 V. The measurement was carried out using Keithley Model 2450 Source Measurement Unit. The photocurrent device has an open-circuit

voltage V_{oc} ~= 1.5 V and is capable of producing few tens to hundreds milliampere of photocurrent depending on the irradiance of light.

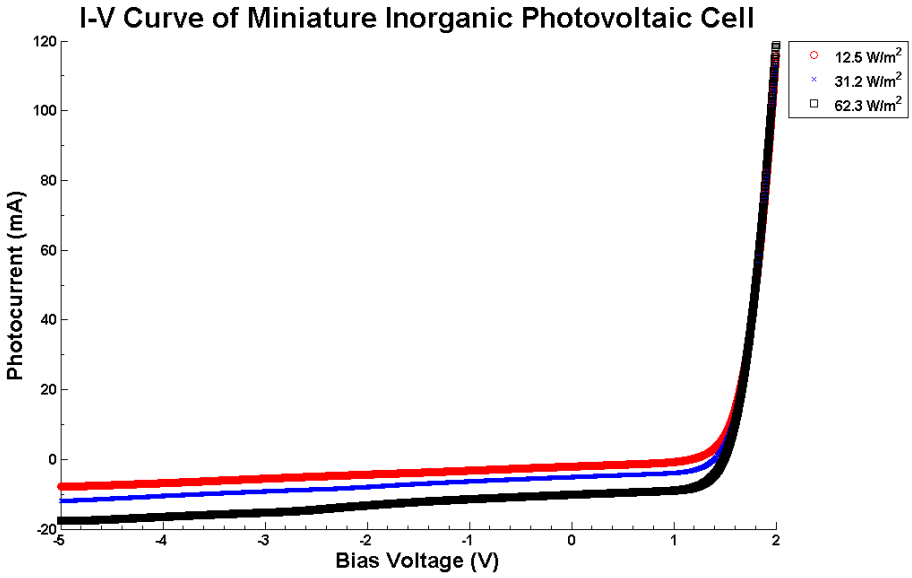

Fig. 5-5. I-V plot for miniature inorganic photovoltaic cell

5.2.2 Random Phase Multisine Excitation Signal

Fig. 5-6 and Fig. 5-7 show the BLA and standard deviation of the FRF respectively from random phase multisine excitation signal applied to the test set-up with miniature photovoltaic cell mounted. Results presented in Fig. 5-6 and Fig. 5-7 are measured at $R_m = 1\ k\Omega$ and $C_m = 1\ \mu F$. Both BLA (Fig. 5-6) and its uncertainty (Fig. 5-7) change with respect to the magnitude of photocurrent. However, the trend is more clearly distinguishable from the uncertainty measurement compared to the BLA measurement.

In Fig. 5-6, significant fluctuation of BLA has been observed at excited frequency of 330 Hz (dominant) and 650 Hz respectively. This corresponds to the large uncertainty of FRF observed at the same excited frequencies as shown in Fig. 5-7. The FRF uncertainty as shown in Fig. 5-7 changes in tandem with the photo-generated currents. The stronger the current, the larger will be the value of the standard deviation. The changes of standard deviation values saturate at high current values.

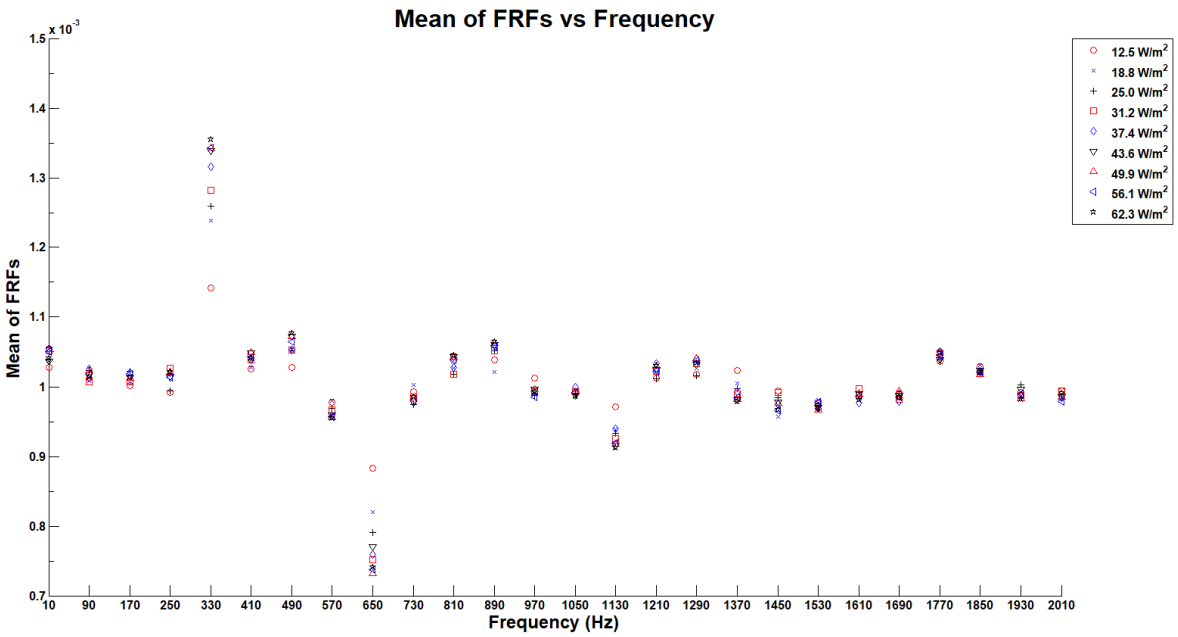

Fig. 5-6. FRF mean plot with random phase multisine excitation signal for miniature inorganic photovoltaic cell ($R_m = 1\ k\Omega$ and $C_m = 1\ \mu F$)

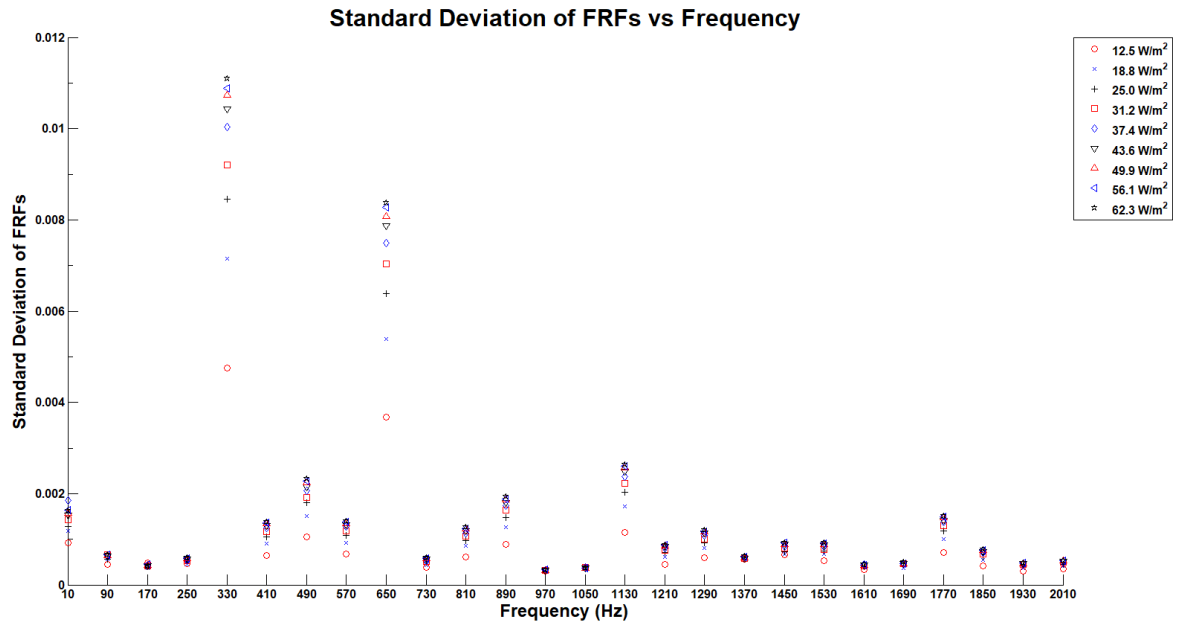

Fig. 5-7. FRF standard deviation plot with random phase multisine excitation signal for miniature inorganic photovoltaic cell ($R_m = 1\ k\Omega$ and $C_m = 1\ \mu F$)

The same trends albeit different fluctuation peaks at excited frequency of 1710 Hz (dominant frequency) and 1550 Hz respectively have been observed for another repeated set of random phase multisine excited measurements on miniature inorganic photovoltaic cell with $R_m = 1\ k\Omega$ but $C_m = 1\ nF$ (Fig. B-5 and Fig. B-6 in APPENDIX B.1). These empirical

measurements demonstrate that the measurement of FRF statistics can be used as an indirect method of measuring photocurrent.

5.2.3 Gaussian Noise Excitation Signal

The measurements were repeated with Gaussian noise excitation signal. Fig. 5-8 and Fig. 5-9 show the plots of mean and standard deviation values of FRF of the circuit with Gaussian noise excitation signal for $R_m = 1\ k\Omega$ and $C_m = 1\ \mu F$. The Gaussian noise excited FRF is a wideband noise that excites every frequency band. Therefore, it has higher spectral resolution compared to multisine excitation. In this case, significant fluctuation of FRF mean values were observed at excited frequency of 730 Hz (dominant), 1050 Hz, and 1770 Hz respectively. The same trends albeit different fluctuation peaks at excited frequency of 490 Hz (dominant), 1990 Hz, 1650 Hz and 410 Hz respectively have been observed for another repeated set of Gaussian noise excited measurements on miniature inorganic photovoltaic cell with $R_m = 1\ k\Omega$ but $C_m = 1\ nF$ (Fig. B-11 and Fig. B-12 in APPENDIX B.2).

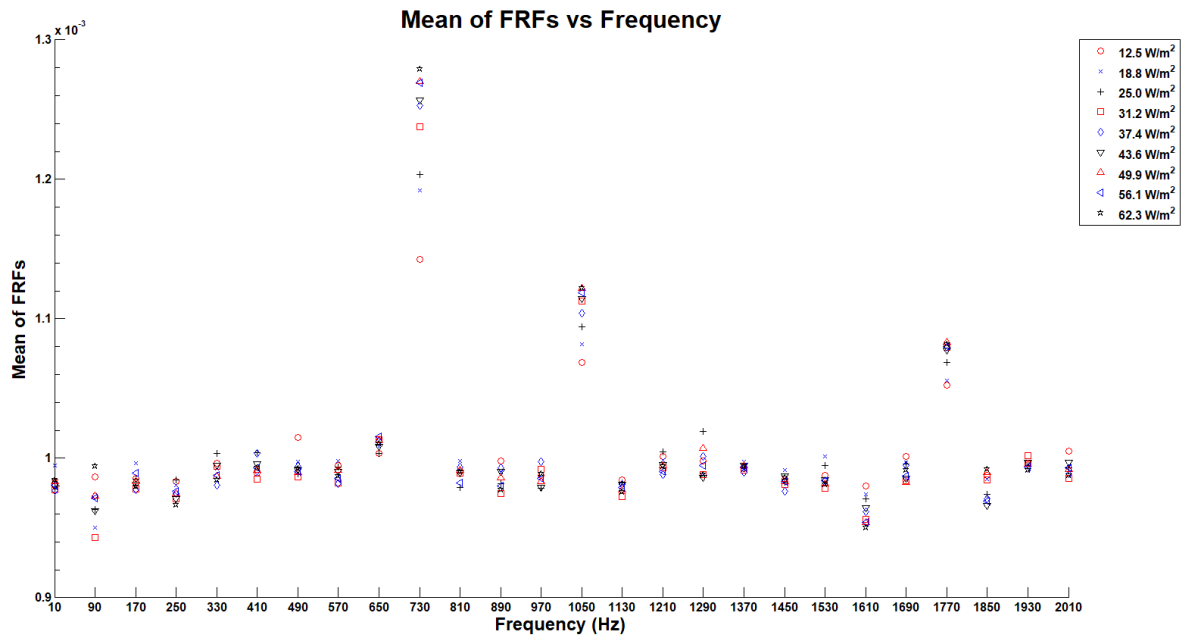

Fig. 5-8. FRF mean plot with Gaussian noise excitation signal for miniature inorganic photovoltaic cell ($R_m = 1\ k\Omega$ and $C_m = 1\ \mu F$)

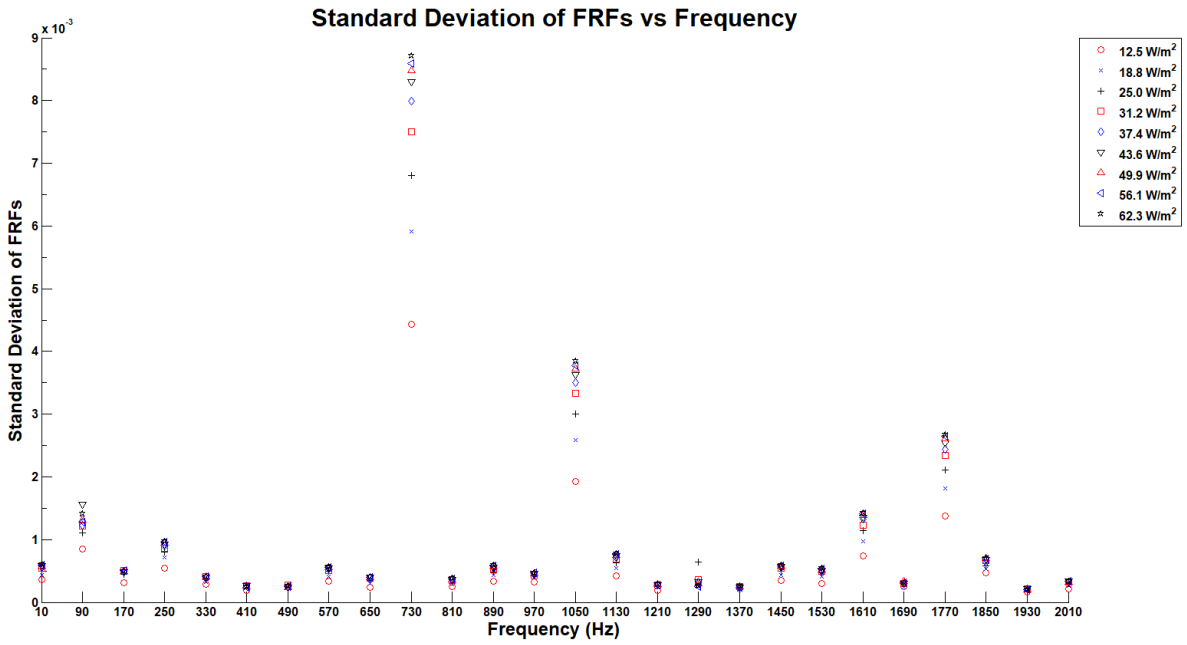

Fig. 5-9. FRF standard deviation plot with Gaussian noise excitation signal for miniature inorganic photovoltaic cell ($R_m = 1\ k\Omega$ and $C_m = 1\ \mu F$)

The FRF uncertainty values change in tandem with the photo-generated currents, as the stronger the current, the larger will be the value of the standard deviation. Even without modeling the physical process involved in detail, the proposed FRF indirect photocurrent measurement technique seems to work well.

The nonlinear photo-response of the photo device is first quantified by FRF measurements. The relationship between the FRF measurements and the magnitude of light irradiance can then be deduced through the regression analysis to obtain the photocurrent and then apply either equation (5-1) or (5-2) to obtain the irradiance of light in $\frac{W}{m^2}$. The proposed method is inherently empirical in nature because the nonlinearity of the sensor under investigation is often poorly understood. Without a good model of nonlinearity, it is impossible to simulate the BLA and its associated uncertainty.

5.2.4 Regression Analysis

Fig. 5-10 shows the plots for photocurrent versus the standard deviation of FRFs on miniature inorganic photovoltaic cell with random phase multisine excitation signal at 330 Hz using linear, quadratic, cubic and an exponential function to fit the data. Equation of the curve fit is shown on the plots. σ represents the FRF standard deviation and I represents the photocurrent

of the photo device. The residuals of the curve fittings are plotted in Fig. 5-11 while the fitness of curve fittings is tabulated in Table 5-3. Refer to Fig. 5-12, Fig. 5-13 and Table 5-4 for regression plots and fitness data on miniature inorganic photovoltaic cell with Gaussian noise excitation source at 730 Hz.

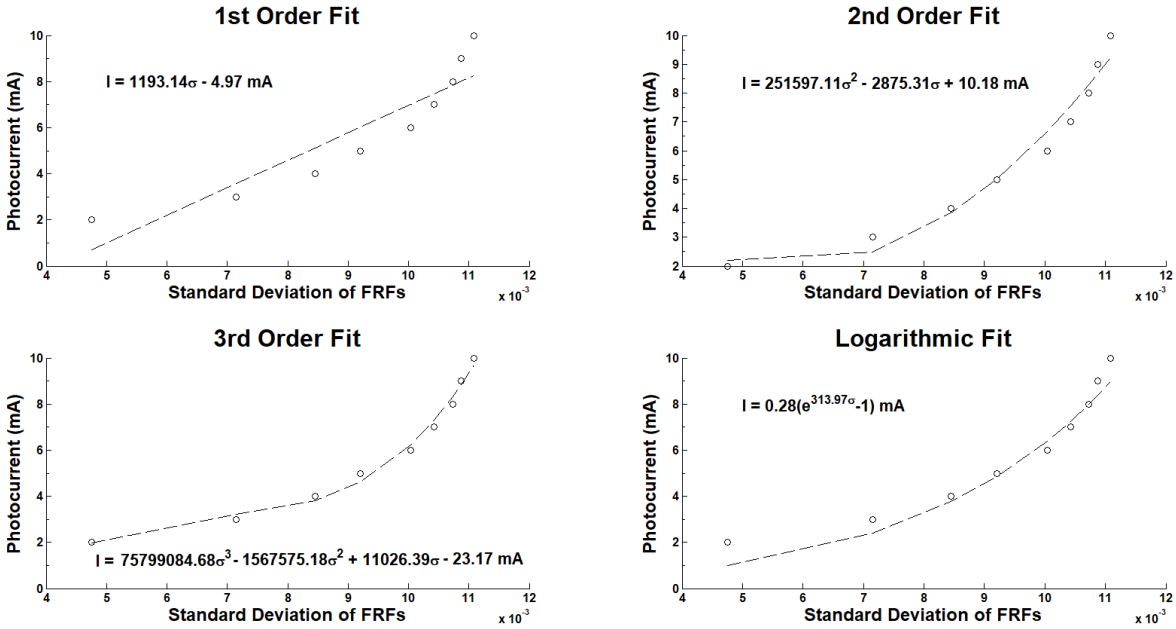

Fig. 5-10. Regression plots of standard deviation of FRFs for miniature inorganic photovoltaic cell with random phase multisine excitation signal at 330 Hz ($R_m = 1\ k\Omega$ and $C_m = 1\ \mu F$)

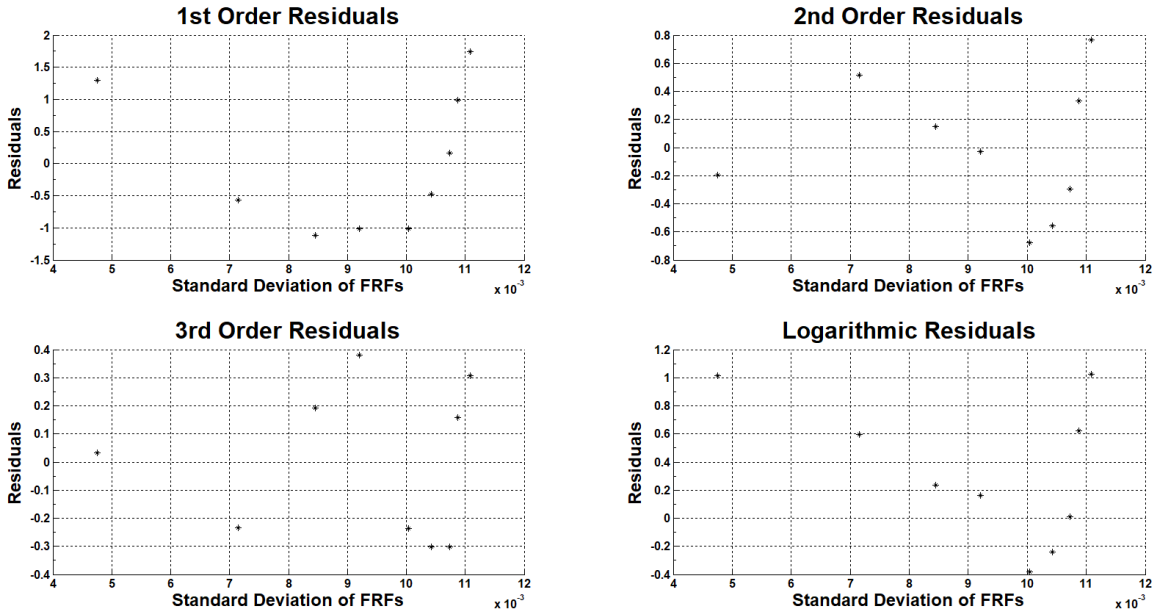

Fig. 5-11. Residuals of regression plots for miniature inorganic photovoltaic cell with random phase multisine excitation signal at 330 Hz ($R_m = 1\ k\Omega$ and $C_m = 1\ \mu F$)

Table 5-3. Fitness of curve fittings for miniature inorganic photovoltaic cell with random phase multisine excitation signal at 330 Hz ($R_m = 1\ k\Omega$ and $C_m = 1\ \mu F$)

Excitation Source	RC Photodetector R_m (Ω)	RC Photodetector C_m (F)	Dominant Frequency (Hz)	Type of Fit	SSE	R-square	Adjusted R-square
Random Phase Multisine	1k	1µ	330	Linear	9.5424	0.8410	0.8182
				Quadratic	1.8852	0.9686	0.9581
				Cubic	0.5949	0.9901	0.9841
				Exponential	3.1128	0.9481	N. A.

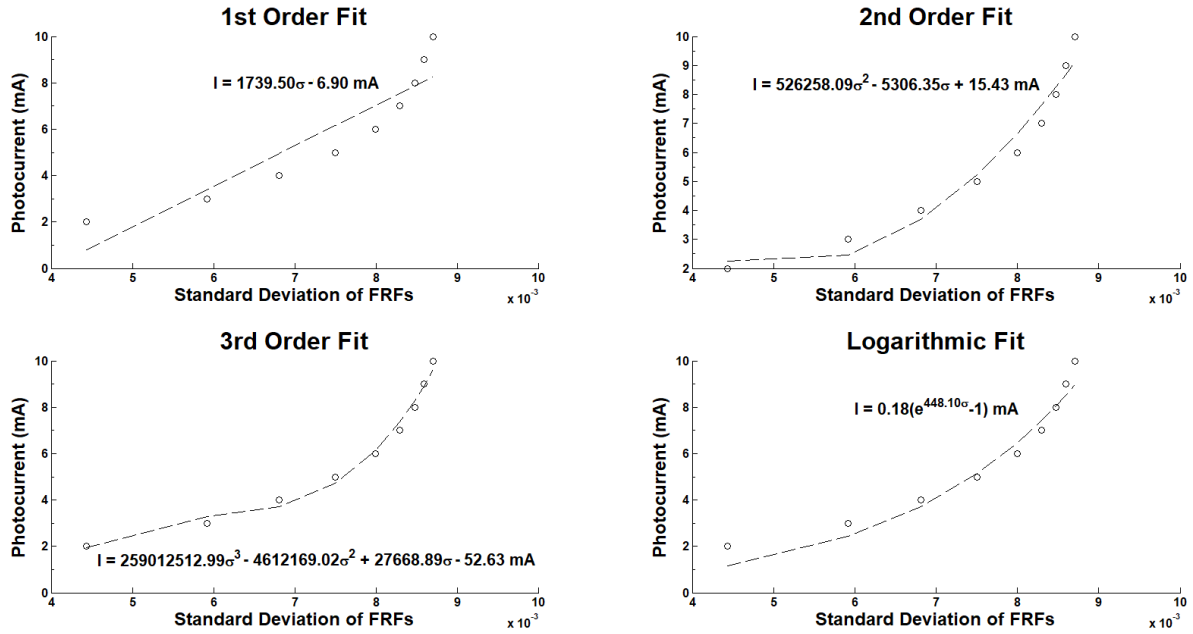

Fig. 5-12. Regression plots of standard deviation of FRFs for miniature inorganic photovoltaic cell with Gaussian noise excitation signal at 730 Hz ($R_m = 1\ k\Omega$ and $C_m = 1\ \mu F$)

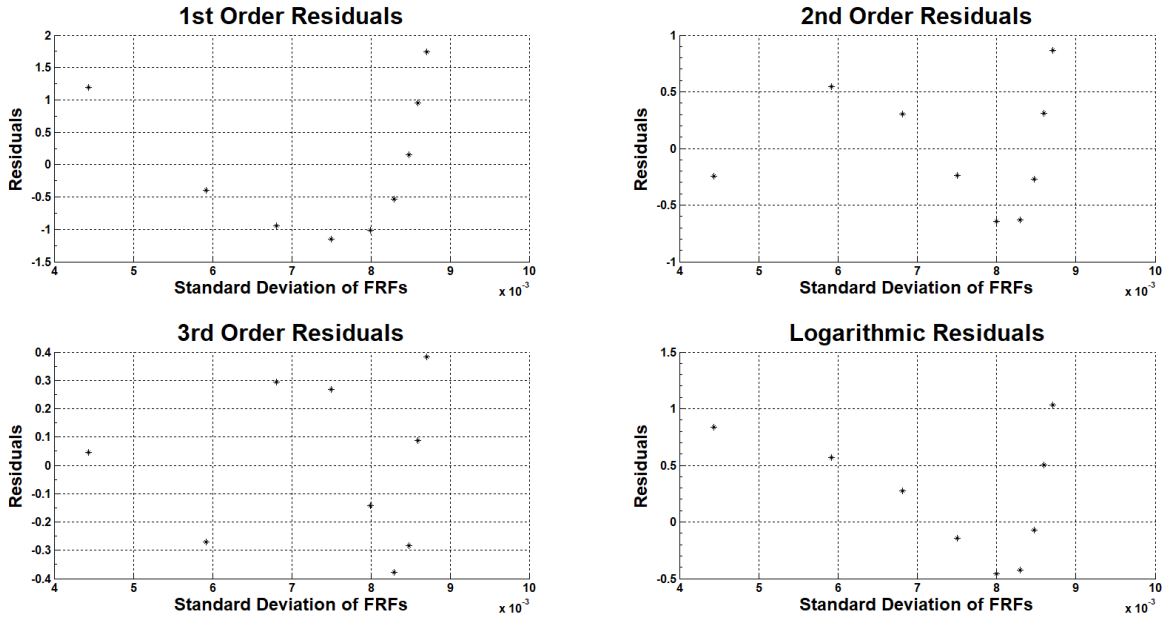

Fig. 5-13. Residuals of regression plots for miniature inorganic photovoltaic cell with Gaussian noise excitation signal at 730 Hz ($R_m = 1\ k\Omega$ and $C_m = 1\ \mu F$)

Table 5-4. Fitness of curve fittings for miniature inorganic photovoltaic cell with Gaussian noise excitation signal at 730 Hz ($R_m = 1\ k\Omega$ and $C_m = 1\ \mu F$)

Excitation Source	RC Photodetector		Dominant Frequency (Hz)	Type of Fit	SSE	R-square	Adjusted R-square
	R_m (Ω)	C_m (F)					
Gaussian Noise	1k	1µ	730	Linear	9.0859	0.8486	0.8269
				Quadratic	2.2397	0.9627	0.9502
				Cubic	0.6320	0.9895	0.9831
				Exponential	2.8351	0.9527	N. A.

Based on the regression analysis, either a quadratic or cubic linear regression will provide a good fit depending on the trade-off between matching accuracy and number of coefficients for the fitted equation. A cubic linear regression plot in general will provide the best fit. The obtained regression function thus enables one-to-one mapping between the standard deviation σ and photocurrent I. The obtained photocurrent I can then subsequently applied to equation (5-1) to obtain the irradiance of light in $\frac{W}{m^2}$.

5.3 Miniature Organic Photovoltaic Cell

5.3.1 I-V Characteristic

Few organic photovoltaic (OPV) cells were ordered and fabricated by Ossila Ltd in their Kroto Innovation Centre at The University of Sheffield. APPENDIX C presents the electrical characterisation and fabrication conditions of those samples.

In this works, an OPV sample was selected from the batch of samples to act as the photocurrent source to the RC photodetector as an alternative light source to miniature inorganic solar cell. The sample was clipped with testing legs before inserting to the test board as shown in Fig. 5-14.

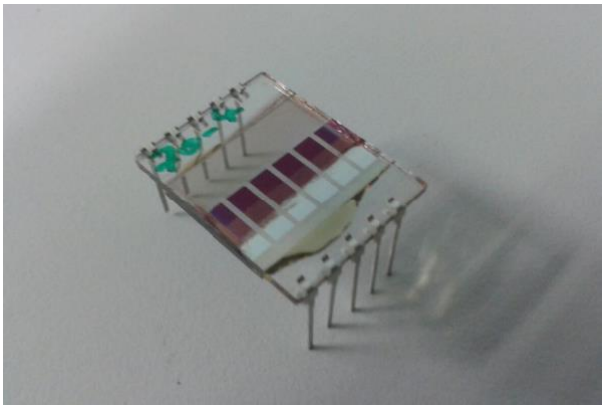

Fig. 5-14. OPV cell with test legs

Fig. 5-15 shows the J-V curves of three slight different process treatment of OPV cells with the terminal voltages biased from -1 V to 1 V under 100 $\frac{mW}{cm^2}$ (1 sun) AM1.5 test conditions. The photocurrent devices have an open-circuit voltage V_{oc} ~= 0.83 - 0.89 V and are capable of producing few tens to hundreds microampere of photocurrent depending on the irradiance of light.

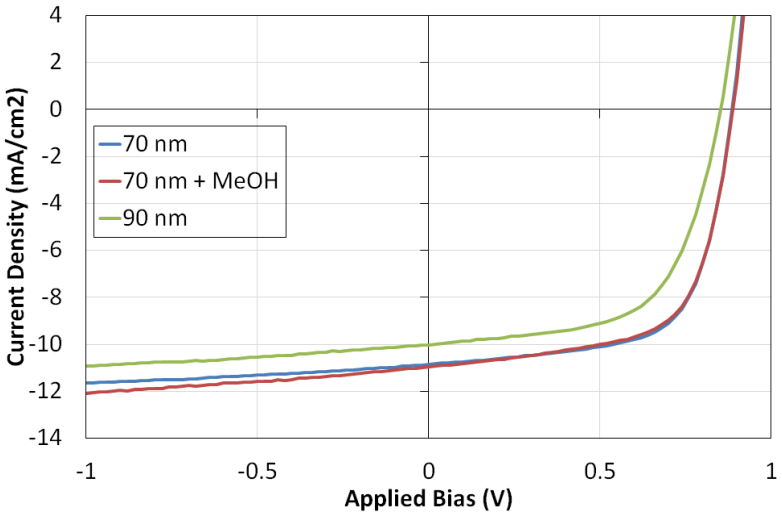

Fig. 5-15. J-V curves of OPV cell

5.3.2 Gaussian Noise Excitation Signal

For the experiments carried out on OPV cell, Gaussian noise was chosen as the excitation signal as the Gaussian noise excited FRF is a wideband noise that excites every frequency band. Therefore, it has higher spectral resolution compared to multisine excitation and has proven to work in previous experiments using miniature inorganic solar cell.

As a single OPV cell provides the photocurrent in microampere range with the dimmer control, the input resistance of the RC photodetector was increased from 1 $k\Omega$ to 100 $k\Omega$ such that current due to the excitation signal is not too strong to interact with the photocurrent from the OPV cell. The output capacitance C_m is fixed at 1 µF as in the previous experiments.

In Fig. 5-16, significant fluctuation of BLA has been observed at excited frequency of 450 Hz and 1370 Hz respectively. This corresponds to the large uncertainty of FRF observed at the same excited frequencies as shown in Fig. 5-17. However, in this case, the FRF uncertainty changes in reverse order with the photo-generated currents, as weaker current shows larger value of the standard deviation.

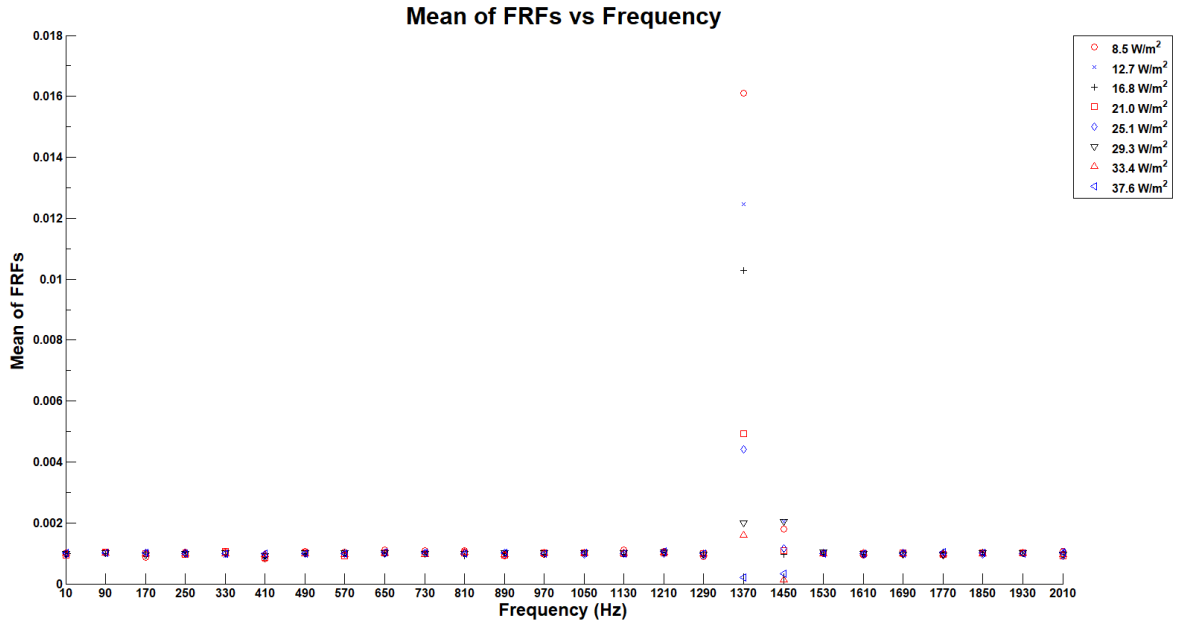

Fig. 5-16. FRF mean plot with Gaussian noise excitation signal for OPV cell ($R_m = 1\ k\Omega$ and $C_m = 1\ \mu F$)

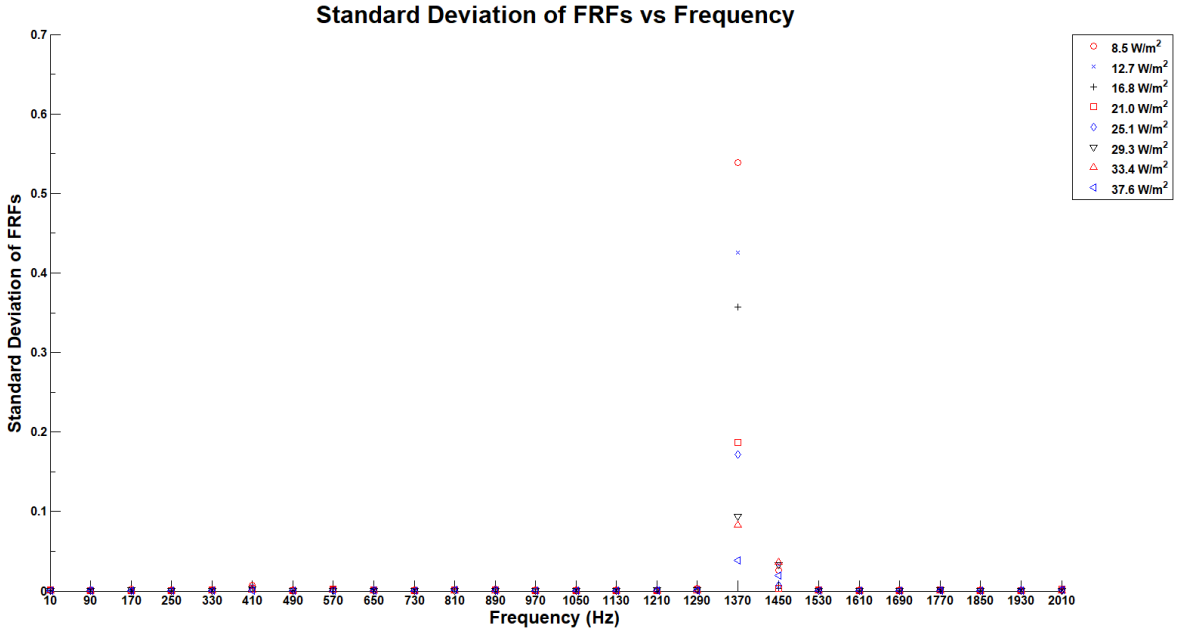

Fig. 5-17. FRF standard deviation plot with Gaussian noise excitation signal for OPV cell ($R_m = 1\ k\Omega$ and $C_m = 1\ \mu F$)

Upon further investigation with higher resistance at the output, i.e. $R_m = 4.7\ k\Omega$ instead of $1\ k\Omega$, it has been found that the trend reverses at the excited frequency of 890 Hz as shown in Fig. 5-18 and Fig. 5-19. Subsequent BLA measurements with larger $R_m = 10\ k\Omega$ as shown in Fig. 5-20 and Fig. 5-21 show consistent results that the FRF uncertainty values changes in tandem with the photo-generated currents, as the stronger the current, the larger will be the

value of the standard deviation (refer to Fig. B-13 and Fig. B-14 in APPENDIX B.3 for the FRF mean and standard deviation plots with $R_m = 100\ k\Omega$).

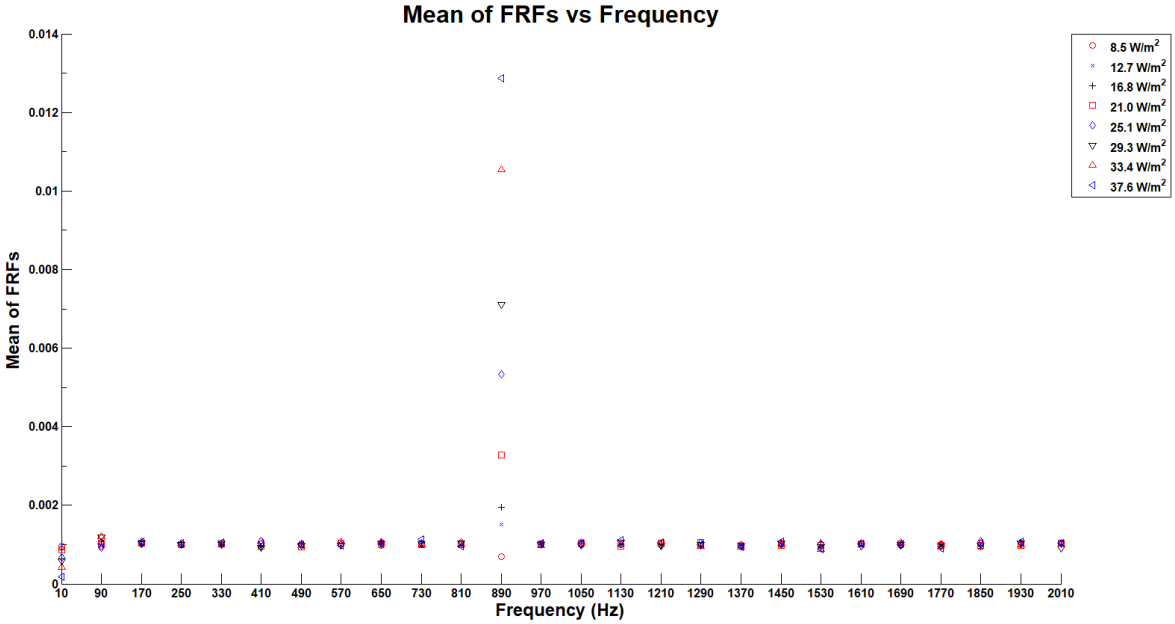

Fig. 5-18. FRF mean plot with Gaussian noise excitation signal for OPV cell ($R_m = 4.7\ k\Omega$ and $C_m = 1\ \mu F$)

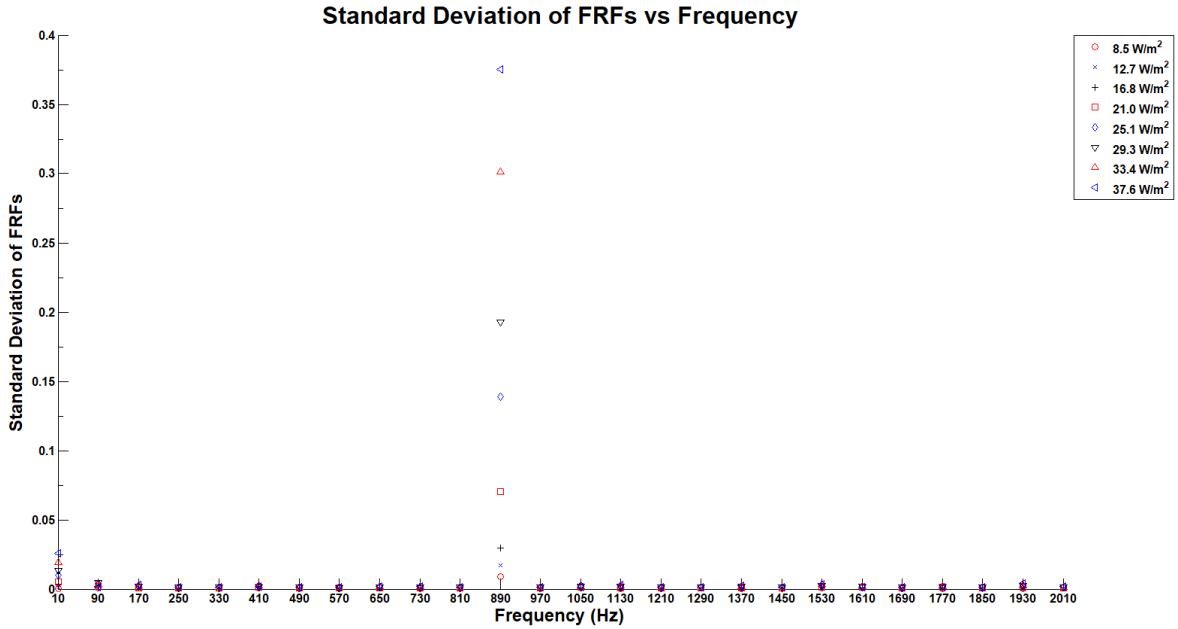

Fig. 5-19. FRF standard deviation plot with Gaussian noise excitation signal for OPV cell ($R_m = 4.7\ k\Omega$ and $C_m = 1\ \mu F$)

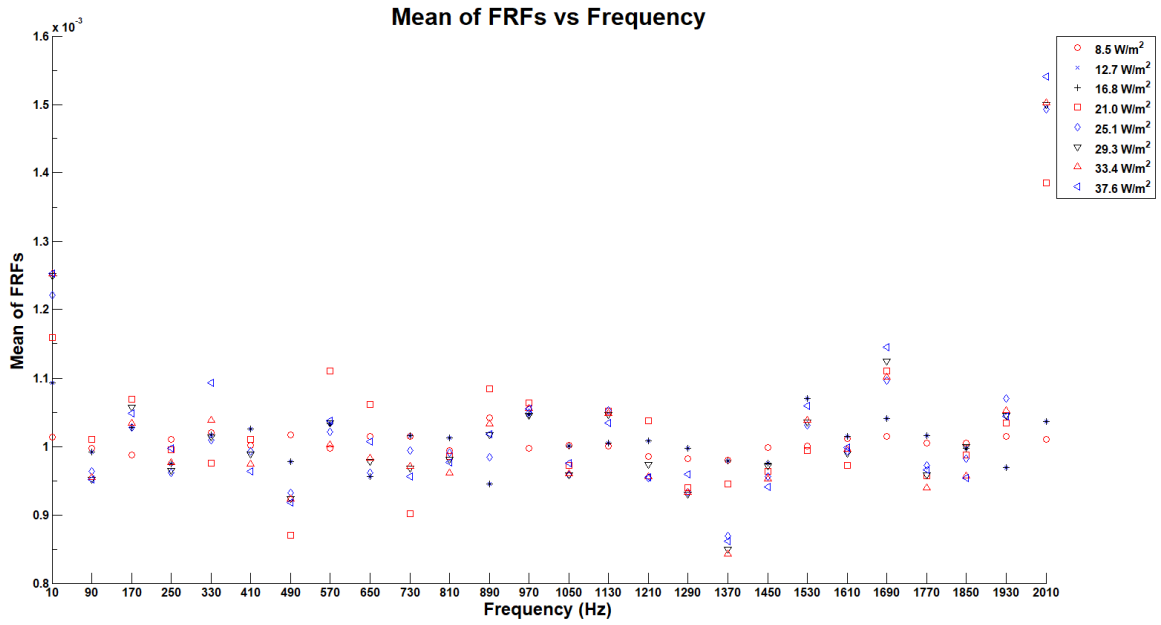

Fig. 5-20. FRF mean plot with Gaussian noise excitation signal for OPV cell ($R_m = 10\ k\Omega$ and $C_m = 1\ \mu F$)

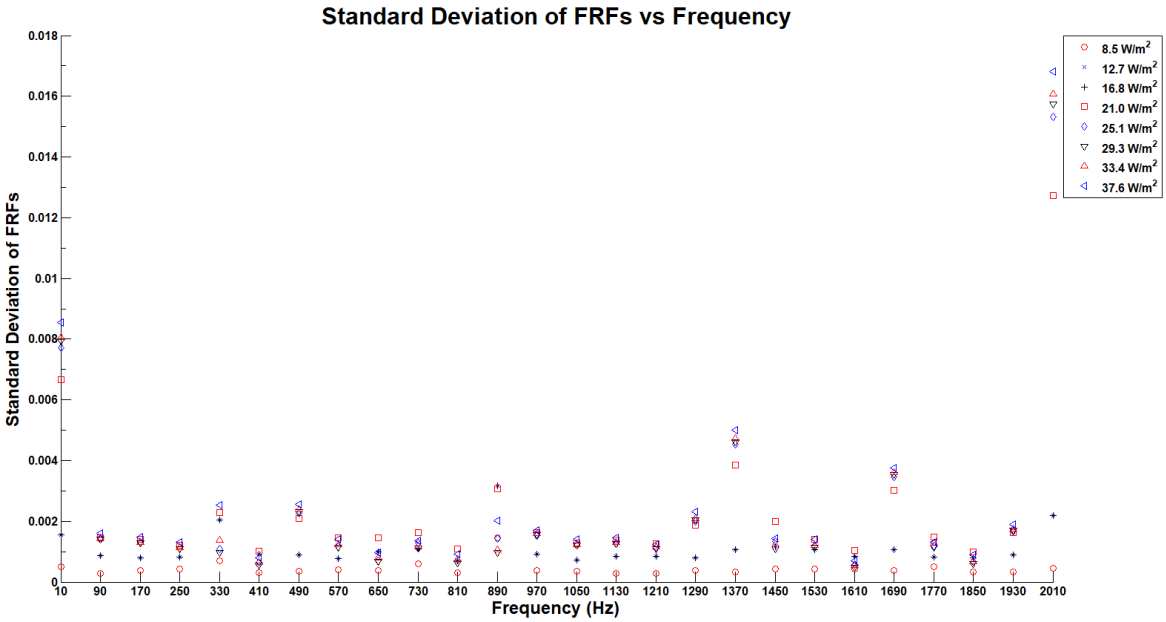

Fig. 5-21. FRF standard deviation plot with Gaussian noise excitation signal for OPV cell ($R_m = 10\ k\Omega$ and $C_m = 1\ \mu F$)

It is postulated that the reversal of trend is due to loading effect in which the current of OPV cell lies on the rather flat portion of the I-V curve as shown in Fig. 5-15 in reverse bias mode instead of the nonlinear exponential region in forward bias mode when the output resistance R_m is smaller than 4.7 $k\Omega$. The transit of reverse to forward bias mode can happen when the voltage across the OPV cell is beyond its open-circuit V_{oc} ~= 0.83 - 0.89 V as shown in Fig.

5-15. Nevertheless, the proposed FRF indirect photocurrent measurement technique proves to work even with OPV cell which produces current of few hundred magnitude order lower than that of the miniature inorganic photovoltaic cell reported in Section 5.1.

5.3.3 Regression Analysis

Fig. 5-22 shows the plots for photocurrent versus the standard deviation of FRFs on OPV cell with Gaussian noise excitation signal at 2010 Hz using linear, quadratic, cubic and an exponential function to fit the data. Equation of the curve fit is shown on the plots. σ represents the FRF standard deviation and I represents the photocurrent of the photo device. The residuals of the curve fittings are plotted in Fig. 5-23 while the fitness of curve fittings is tabulated as in Table 5-5.

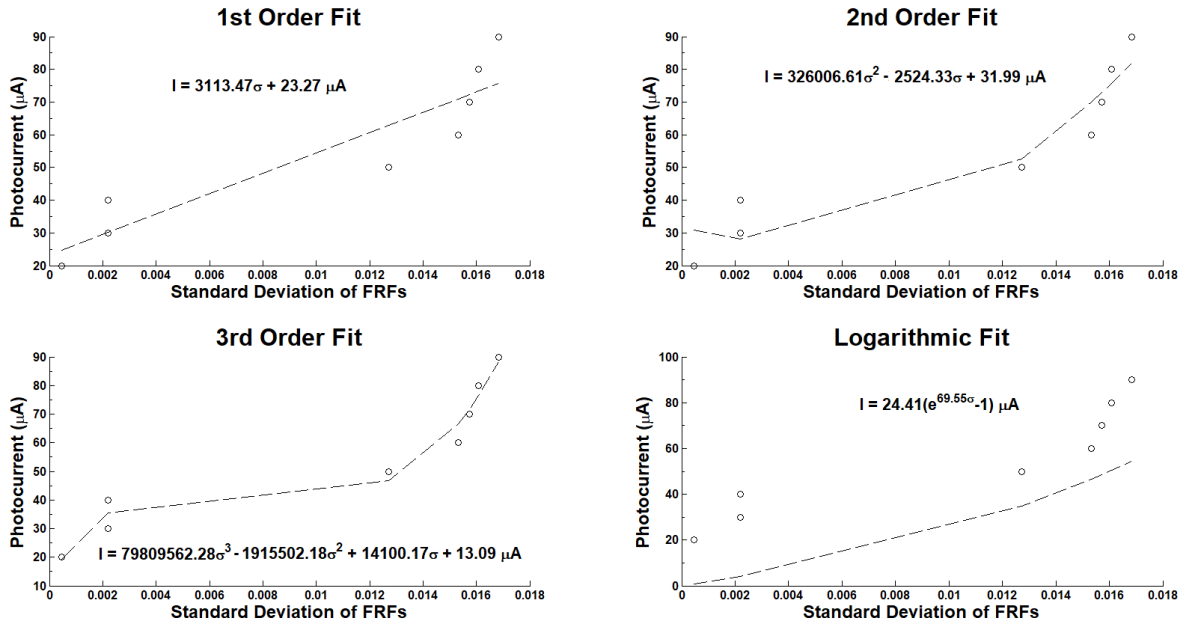

Fig. 5-22. Regression plots of standard deviation of FRFs for OPV cell with Gaussian noise excitation signal at 2010 Hz ($R_m = 10\ k\Omega$ and $C_m = 1\ \mu F$)

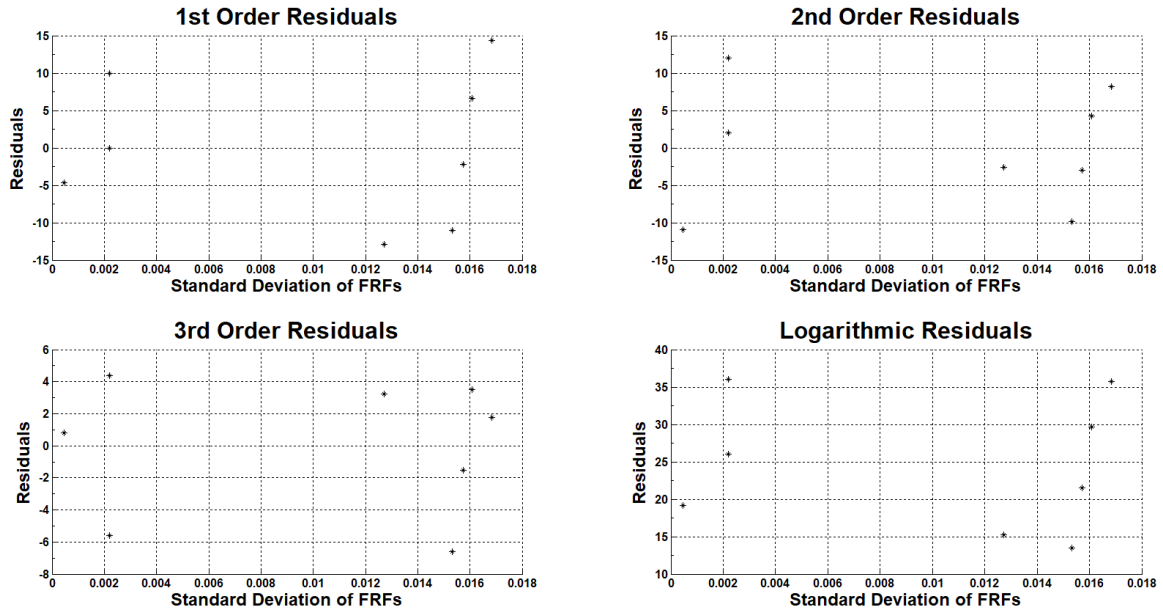

Fig. 5-23. Residuals of regression plots for OPV cell with Gaussian noise excitation signal at 2010 Hz ($R_m = 10\ k\Omega$ and $C_m = 1\ \mu F$)

Table 5-5. Fitness of curve fittings for OPV cell with Gaussian noise excitation signal at 2010 Hz ($R_m = 10\ k\Omega$ and $C_m = 1\ \mu F$)

Excitation Source	RC Photodetector		Dominant Frequency (Hz)	Type of Fit	SSE	R-square	Adjusted R-square
	R_m (Ω)	C_m (F)					
Gaussian Noise	10k	1µ	2010	Linear	661.5845	0.8425	0.8162
				Quadratic	464.2545	0.8895	0.8452
				Cubic	123.0740	0.9707	0.9487
				Exponential	5374.1000	-0.2795	N. A.

As for the case of miniature inorganic photovoltaic cell, either a quadratic or cubic linear regression will provide a good fit depending on the trade-off between matching accuracy and number of coefficients for the fitted equation. A cubic linear regression plot in general will provide the best fit. The obtained regression function thus enables one-to-one mapping between the standard deviation σ and photocurrent I. The obtained photocurrent I can then subsequently applied to equation (5-2) to obtain the irradiance of light in $\frac{W}{m^2}$.

5.4 Correlation Test

Correlation tests were carried out to find the correlation coefficients which indicate the relationship between the photocurrent and the computed standard deviations of FRFs, and to

what extent the two variables move together. Table 5-6 shows the comparison of statistical parameters of Pearson and Kendall tau rank correlation tests. Pearson correlation test is a measure of the strength and direction of the linear relationship between two data sets, and is regarded as the best measure of correlation. Kendall tau rank is a measure of the portion of ranks that match between two data sets.

All the three samples under study have Pearson product-moment correlation coefficient, *rho*, close to 1 indicating a high positive correlation between the photocurrent and the standard deviations of FRFs. The corresponding *p-val* is less than the significance level of 0.05. This indicates the rejection of the hypothesis that no correlation exists between the two variables.

For Kendall's tau correlation test, the obtained *tau* coefficients are 1 or close to 1 indicating that the rankings of the photocurrent and the standard deviations of FRFs are the same.

Table 5-6. Comparison of Statistical Parameters of Correlation Tests

Sample	Excitation Source	Peak Frequency (Hz)	Pearson		Kendall
			rho	*p-val*	*tau*
Miniature Inorganic Photovoltaic Cell	Random Phase Multisine	330	0.9170	0.0005	1.0000
Miniature Inorganic Photovoltaic Cell	Gaussian Noise	730	0.9212	0.0004	1.0000
Organic Photovoltaic (OPV) Cell	Gaussian Noise	2010	0.9179	0.0013	0.9820

5.5 Summary of Experimental Results

Whenever a photosensor is excited with an excitation signal, there always exists a dominant frequency in which the spread of standard deviation of FRFs is the largest. The existent of this dominant frequency depends on the interaction of the type of photosensor under test, the resistance and capacitance of the RC photodetector, and the type of excitation signal applied in the measurement circuit. Table 5-7 compares the dominant frequencies with the largest spread of standard deviation of FRFs across different combinations for the parameters of the measurement circuit. The table shows that different medium of photocurrent generation will produce different characteristics of the dominant frequency. The dominant frequency will vary with the output resistance R_m and capacitance C_m of the RC photodetector as well as the type of signal used for the excitation.

Table 5-7. Comparison of dominant frequencies in Frequency Domain Photocurrent Measurement

Photocurrent Device	Excitation Signal	RC Photodetector		Dominant Frequency (Hz)	Other Peak Frequencies (Hz)	Comments
		R_m (Ω)	C_m (F)			
Miniature Inorganic Photovoltaic Cell	Random Phase Multisine	1k	1µ	330	650	Fig. 5-6, 5-7
		10k		330	650	Fig. B-1, B-2
		100k		330	650	Fig. B-3, B-4
	Gaussian Noise	1k		730	1050, 1770	Fig. 5-8, 5-9
		10k		730	1050, 1770	Fig. B-7, B-8
		100k		730	1050, 1770	Fig. B-9, B-10
	Random Phase Multisine	1k	1n	1370	810, 1450, 570	Fig. B-5, B-6
	Gaussian Noise			490	410, 2010	Fig. B-11, B-12
Organic Photovoltaic (OPV) Cell	Gaussian Noise	4.7k	1µ	890	NIL	Fig. 5-18, 5-19
		10k		2010	1370, 1690	Fig. 5-20, 5-21
		100k		490	570	Fig. B-13, B-14

CHAPTER 6 CONCLUSION & FURTHER WORK

6.1 Conclusion

The proposed research presents the technique of using the FRF statistics of a photosensor to perform indirect light intensity measurement. The proposed method is different from the conventional method of wide-band direct photocurrent measurement. The method is potentially applicable to any sensor that are sensitive to output current loading.

The proposed research started with the initial works into the frequency response of the RC photodetector excited by noise utilizing BLA measurement methodology. Two excited signals, random phase multisine and Gaussian noise have been applied to activate the measurement circuit. The photocurrent was sourced from miniature solar cell and OPV cells respectively. In both cases, the standard deviations of FRFs of output signal show a strong correlation with the incident light intensity. The correlation is generally valid across all frequency bands but much stronger at certain frequencies.

The magnitude of the photocurrent can be deduced with reasonable accuracy by measuring the standard deviation of FRF at selected frequencies without resorting to the use of high-end current measuring instruments. This particular feature may be useful in sensor design because it allows noise sources with stable statistical characteristics to be used in the measurement circuit. The promising result provides hindsight to an indirect method to measure the response of sensors especially those sensors that produce minute electrical signal, thus avoiding environmental interference encountered in wide-band direct current measurement technique. The simplicity of the experimental setup and analysis suggests that it is possible to miniaturize the measurement circuit such that it can be embedded directly into the photosensor.

The research work has defined the steps involved in carrying out the frequency domain photocurrent measurement as outlined in Fig. 3-9. This is to make sure the results obtained are valid and similar to what have been reported in this report. In order to obtain the experimental results, a measurement circuit board has been designed and constructed as shown in Fig. 3-8 and modelled for simulation as shown in Fig. 4-1. The proposed measurement technique on photocurrent detection has been successfully applied to obtain

results as tabulated in Table 5-7 These accomplished the three research objectives as listed in section 1.3.

6.2 Future Work

The idea of mixing noise source with a sensing signal, detect and statistically quantify the spread of the output response as an indirect way of measuring the signal can be explored to other types of sensor, not limiting to only photosensor. This research only looks into the photosensor and its signal as photocurrent. The field can be widened to cover sensors which produce weak signals, and to determine if the noise coupling measurement technique can be easily exploited to gauge the strength of the signals produced by those sensors.

As shown in Table 5-7, the dominant frequency obtained from the frequency domain photoucurrent measurement vary with the medium of the photocurrent generation, output resistance R_m and capacitance C_m of the RC photodetector as well as the type of signal used for the excitation. More experimental works can be carried out in order to understand and establish the interaction between these measurement parameters so that the measurement technique can be fine-tuned in each separate case.

The proposed BLA measurement circuit can be built as an integrated part of a particular photosensor. This will provide a complete low-cost solution for light intensity detection, especially for application in “on/off” switch control of electrical appliances.

On the hardware implementation, a universal socket can be built to the measurement circuit board for the ease of mounting and unmounting of different types of photosensors. The RC photodetector can be made configurable by programming the switching array of resistances and capacitances to any required values with the use of a microcontroller. For ease of signal processing instead of porting the collected data from Labview to Matlab, analogue filter-banks can be designed to extract the relevant spectral information and to perform approximate FRF computation on the circuit board. Alternatively, a more elaborated Labview VI program can be developed to complete the whole suite of signal processing from signal generation to the display of FRF statistics on the virtual front panel.

REFERENCES

[1] Lasse Lensu, Michael Frydrych, Jussi Parkkinen, Sinikka Parkkinen, and Timo Jaaskelainen, "Color-Sensitive Biosensors for Imaging Applications," in *Smart Biosensor Technology*, CRCF Press, 2006, pp. 437-460.

[2] "PV Education," [Online]. Available: http://www.pveducation.org/pvcdrom/series-resistance.

[3] B. Mazhari, "An improved solar cell circuit model for organic solar cells," *Solar Energy Materials & Solar Cells,* vol. 90, pp. 1021-1033, 2006.

[4] Mohsen Taherbaneh, Gholamreza Farahani, and Karim Rahmani, Evaluation the Accuracy of One-Diode and Two-Diode Models for a Solar Panel Based Open-Air Climate Measurements, vol. Ch 10, P. L. A. Kosyachenko, Ed., In Tech, 2011, pp. 201-228.

[5] Oday Mohammed Abdulwahhab, "Improvement of the MATLAB/Simulink Photovoltaic System Simulator Based on a Two-Diode Model," *International Journal of Soft Computing and Engineering (IJSCE),* vol. 4, no. 1, pp. 117-122, March 2014.

[6] Atul Gupta and Venu Uppuluri Srinivasa, "Design, Simulation and Verification of Generalized Photovoltaic Cells Model Using First Principles Modeling," *ACEEE Int. J. on Control System and Instrumentation,* vol. 3, no. 1, pp. 102-108, February 2012.

[7] Ling Qin, Shaojun Xie, Chen Yang, and Jianjun Cao, "Dynamic Model and Dynamic Characteristics of Solar Cell," *IEEE ECCE Asia Downunder,* pp. 659-663, 2013.

[8] Maria Carmela Di Piazza, and Gianpaolo Vitale, "Photovoltaic Source Dynamic Modeling Issues," in *Photovoltaic Sources Modeling and Emulation*, Springer, 2012, pp. 131-169.

[9] D. Chenvidhya, K. Kirtikara, and C. Jivacate, "PV module dynamic impedance and its voltage and frequency dependencies," *Solar Energy Materials & Solar Cells,* no. 86, pp. 243-251, 2005.

[10] T. Chayavanich, C. Limsakul, N. Chayavanich, D. Chenvidhya, C. Jivacate, and K. Kirtikara, "Voltage and frequency dependent model for PV module dynamic impedance," in *17th International Photovoltaic Science & Engineering Conference*, 2007.

[11] Tsutomu Miysaka, and Koichi Koyama, "Image sensing and processing by a bacteriorhodopsin-based artificial photoreceptor," *Optical Society of America,* pp. 6371-6379, 1993.

[12] Wei Wei Wang, George K. Knopf, and Marjeet S. Bassi, "Time and frequency response characteristics of bacteriorhodopsin-based photodetectors," *Optical Engineering,* vol. 45, no. 8, pp. 084001-1 to 084001-9.

[13] Wei Wei Wang, George K. Knopf, and Amarjeet S. Bassi, "Photoelectric properties of a detector based on dried bacteriorhodopsin film," *Biosensors and Bioelectronics,* vol. 21, pp. 1309-1319, 2006.

[14] S. Takamatsu, K. Hoshino, K. Matsumoto, T. Miyasaka, and I. Shimoyama, "Biomolecular Image Sensor of Bacteriorhodopsin Patterned by Electrodeposition," in *18th IEEE International Conference on MEMS*, 2005.

[15] Wei Wei Wang, Georger K Knopf, and Marjeet S. Bassi, "Bioelectronic Imaging Array Based on Bacteriorhodopsin Film," *IEEE Transactions on NanoBioscience,* vol. 7, no. 4, pp. 249-256, December 2008.

[16] Jonhyun Shin, Pallab Bhattacharya, Hao-Chih Yuan, and Zhenqiang Ma, "Low-power bacteriorhodopsin-silicon n-channel metal-oxide field-effect transistor photoreceiver," *Optical Letters,* vol. 32, no. 5, pp. 500-502, Mar 2007.

[17] M. Solomou, C. Evans, D. Rees, and N. Chiras, "Frequency domain analysis of nonlinear systems driven by multiharmonic signals," in *Proceedings of the 19th IEEE Conference on Instrumentation and Measurement Technology*, 2002.

[18] R.V. Roy, and P.D. Spanos, "Power spectral densities of nonlinear system response: the recursion method," *Journal of Appl. Mech. Trans. ASME,* no. 60, pp. 358-365, 1993.

[19] W.J. Rugh, Nonlinear System Theory - The Volterra / Wiener Approach, Baltimore, London: The Johns Hopkins University Press, 1981.

[20] Volterra Vito, Theory of Functionals and of Integrals and Integro-Differential Equations, New York: Dover Publications, 1959.

[21] Z.Q. Lang, and S.A. Billings, "Output frequencies of nonlinear systems," *International Journal of Control,* vol. 57, no. 5, pp. 713-730, 1997.

[22] J.J. Bussgang, L. Ehrman, and J.W. Graham, "Analysis of nonlinear systems with multiple inputs," *Proc. IEEE,* vol. 62, no. 8, pp. 1088-1119, 1974.

[23] Wikipedia, "Nonlinear System Identification," [Online]. Available: https://en.wikipedia.org/wiki/Nonlinear_system_identification.

[24] Xing Jian Jing, Zi Qiang Lang, Stephen A. Billings, "Output frequency response function-based analysis for nonlinear Volterra systems," *Mechanical Systems and Signal Processing* , no. 22, pp. 102-120, 2008.

[25] Z.Q. Lang and S.A. Billings, "Energy transfer properties of non-linear systems in the frequency domain," *International Journal Control,* vol. 78, no. 5, pp. 345-362, 2005.

[26] M. Schetzen, The Volterra and Wiener Theories of Nonlinear Systems, New York: Wiley, 1980.

[27] Van De Wouw N, Nijmeijer H, and Van Campen DH, "A Volterra Series Approach to the Approximation of Stochastic Nonlinear Dynamics," *Nonlinear Dyn,* no. 27, pp. 397-409, 2002.

[28] D.A. George, "Continuous nonlinear systems," MIT Research Laboratory of Electronics, Cambridge, MA, July 1959.

[29] Edward Bedrosian, and Stephen O. Rice, "The Output Properties of Voltera Systems (Nonlinear Systems with Memory) Driven by Harmonic and Gaussian Inputs," *Proceedings of the IEEE,* vol. 59, no. 12, pp. 1688-1707, December 1971.

[30] S. A. Billings, "Identification of Nonlinear Systems - A Survey," *IEE Proceedings D - Control Theory and Applications,* vol. 127, no. 6, pp. 272-285, November 1980.

[31] Xing Jian Jing, Zi Qiang Lang, and Stephen A. Billings, "Output frequency properties of nonlinear systems," *International Journal of Non-Linear Mechanics,* no. 45, pp. 681-690, 2010.

[32] Xing Jian Jing, Zi Qiang Lang, and Stephen A. Billings, "The parametric characterisitics of frequency response functions for nonlinear system," *International Journal of Control,* vol. 79, no. 12, pp. 1552-1564, 2006.

[33] K. Vanhoenacker, J. Schoukens, J. Swevers, and D. Vaes, "Summary and comparing overview of techniques for the detection of non-linear distortions," in *ISMA,* 2002.

[34] Vanhoenacker K., and J. Schoukens, "Frequency Response Function Measurements in the presence of Nonlinear Distortions," in *Proceedings IEEE International Workshop on Intelligent Signal Processing,* Budapest (Hungary), September 1999.

[35] Vanhoenacker K., T. Dobrowiecki, and J. Schoukens, "Design of Multisine Excitations

to Characterize the Nonlinear Distortions During FRF-measurements," in *Proceedings IEEE Instrumentation and Measurement Technology Conference*, Baltimore (USA), May 2000.

[36] Rik Pintelon, Ebrahim Louarroudi, and John Lataire, "Nonparametric time-variant frequency response funcion estimates using arbitrary excitations," *Automatica,* no. 51, pp. 308-317, 2015.

[37] S. Narayanan, "Transistor Distortion Analysis Using Volterra Series Representation," *The Bell System Technical Journal,* pp. 991-1024, May-June 1967.

[38] Robert F. Pierret, Semiconductor device fundamentals, Addison-Wesley Publishing Company,Inc., 1996.

[39] John O. Attia, "Semiconductor Physics," in *Electronics and Circuit Analysis using MATLAB*, CRC Press, 1999, pp. 284-295.

[40] Paul Van Halen, "A New Semiconductor Junction Diode Space Charge Layer Capacitance Model," in *IEEE Bipolar Circuits & Technology Meeting*, 1988.

[41] J. Bendat, and A. G. Piersol, Engineering Applications of Correlations and Spectral Analysis, New York: Wiley, 1980.

[42] Johan Schoukens, Rik Pintelon, and Tadeusz Dobrowiecki, "Linear Modeling in the Presence of Nonlinear Distortions," *IEEE Transactions on Instrumentation and Measurement,* vol. 51, no. 4, pp. 786-792, Aug 2002.

[43] R. Pintelon and J. Schoukens, System Identification: A Frequency Domain Approach, Piscataway: IEEE Press, 2001.

[44] Johan Schoukens, and Tadeusz Dobrowiecki, "Design of broadband excitation signals with a user imposed power spectrum and amplitude distribution," in *15th IEEE Instrumentation and Measurement Technology Conference*, St Paul, 1998.

[45] Tadeusz Dobrowiecki, and Johan Schoukens, "Practical choices in the FRF measurement in presence of nonlinear distortions," in *16th IEEE Instrumentation and Measurement Techonlogy Conference*, Venice, 1999.

[46] Johan Schoukens, P. Guillaume, and Rik Pintelon, "Design of broadband excitation signals," in *Pertubation Signals for System Indentification,* 1993.

[47] J. Schoukens, J. Lataire, R. Pintelon, and G. Vandersteen, "Robustness issues of the best linear approximation of a nonlinear system," *IEEE Transactions on Instrumentation &*

Measurement, vol. 58, no. 5, pp. 1737-1745, May 2009.

[48] Lasse Lensu, Jussi Parkkinen, Sinikka Parkkinen, Michael Frydrych, and Timo Jaaskelainen, "Photoelectrical properties of protein-based optoelectronic sensor," *Optical Materials,* no. 21, pp. 783-788, 2003.

[49] ElectronicsTutorials, "Active Band Pass Filter," [Online]. Available: http://www.electronics-tutorials.ws/filter/filter_7.html.

[50] Rod Elliot (ESP), "Precision Rectifiers," [Online]. Available: http://sound.whsites.net/appnotes/an001.htm.

[51] Texas Instruments, "An-20 An Applications Guide for Op Amps," May 2013. [Online]. Available: http://www.ti.com/lit/an/snoa621c/snoa621c.pdf.

[52] J. F. Barrett, "The Use of Functionals in the Analysis of Nonlinear Physical Systems," Statistical Advisory Unit, Report No. 1/57, Ministry of Supply, Great Britain, 1957.

[53] J. S. Bendat and A. G. Piersol, Engineering Applications of Correlations and Spectral Analysis, New York: Wiley, 1980.

[54] John O. Attia, Electronics and Circuit Analysis Using Matlab, CRC Press LLC, 1999.

[55] Wei-Chih Wang, *Optical Detectors,* Department of Power Mechanical Engineering, National Tsing Hua University.

[56] A. S. Sedra, and K. C. Smith, Microelectronics Circuits, vol. 4th Ed., New York: Oxford University Press, 1998.

APPENDIX A FREQUENCY DOMAIN PHOTOCURRENT SIMULATION DATA

A.1 Random-Phase Multisine Excitation

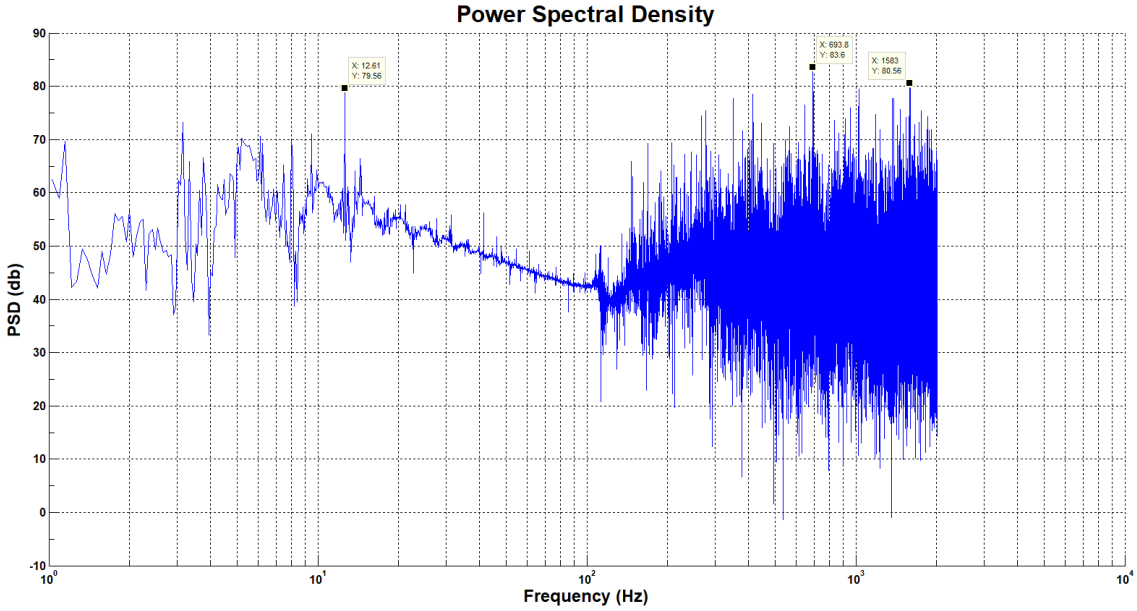

Fig. A-1. Simulated PSD plot of FRF standard deviations with random phase multisine excitation signal for photovoltaic cell ($R_m = 10\ k\Omega$ and $C_m = 1\ \mu F$)

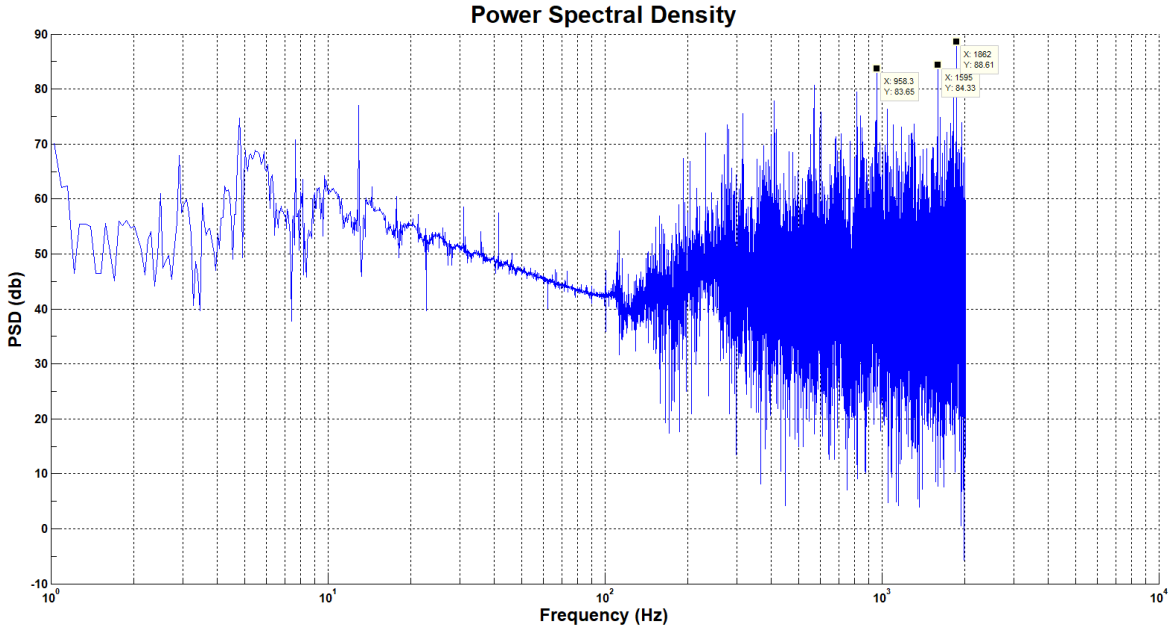

Fig. A-2. Simulated PSD plot of FRF standard deviations with random phase multisine excitation signal for photovoltaic cell ($R_m = 100\ k\Omega$ and $C_m = 1\ \mu F$)

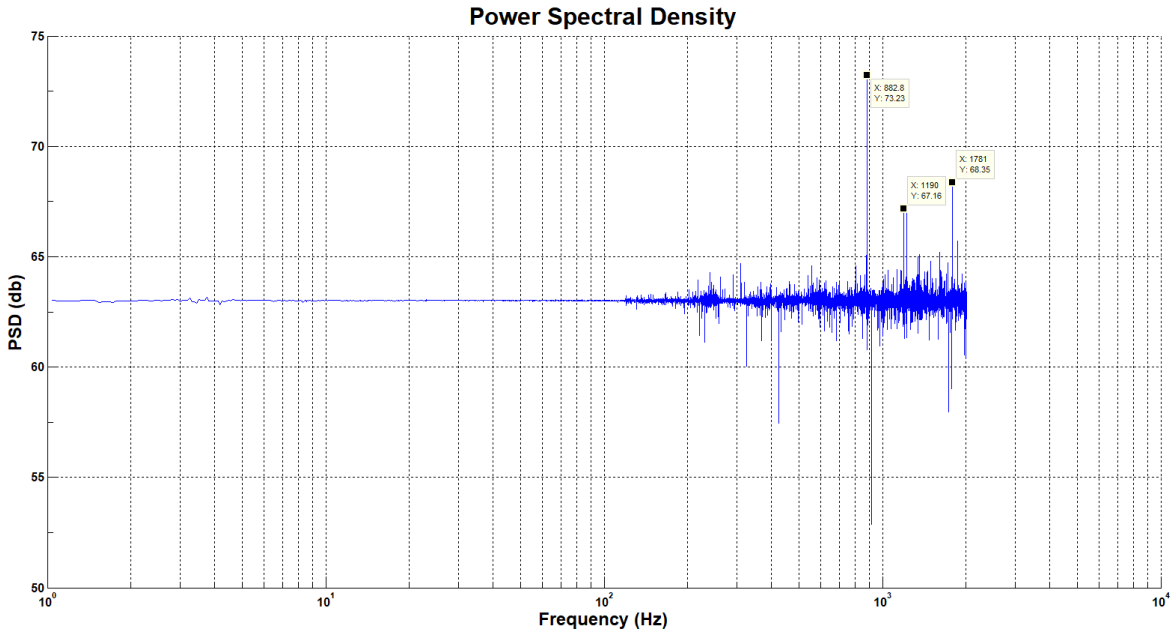

Fig. A-3. Simulated PSD plot of FRF standard deviations with random phase multisine excitation signal for photovoltaic cell ($R_m = 1\ k\Omega$ and $C_m = 1\ nF$)

A.2 Gaussian Noise Excitation with Miniature Inorganic Photovoltaic Cell

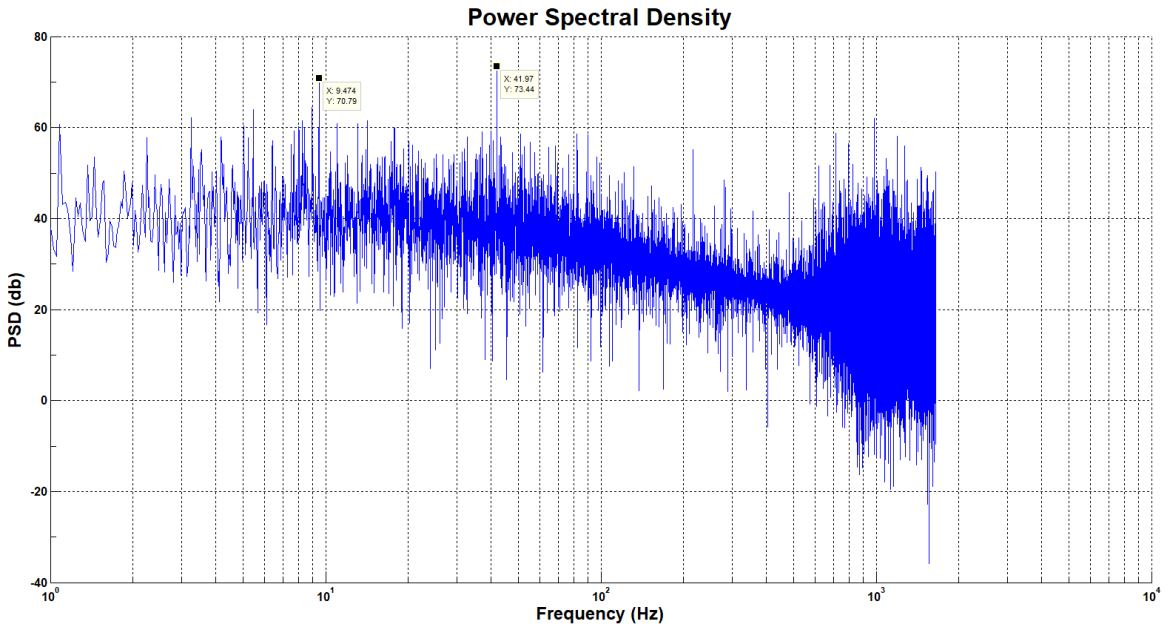

Fig. A-4. Simulated PSD plot of FRF standard deviations with Gaussian noise excitation signal for photovoltaic cell ($R_m = 10\ k\Omega$ and $C_m = 1\ \mu F$)

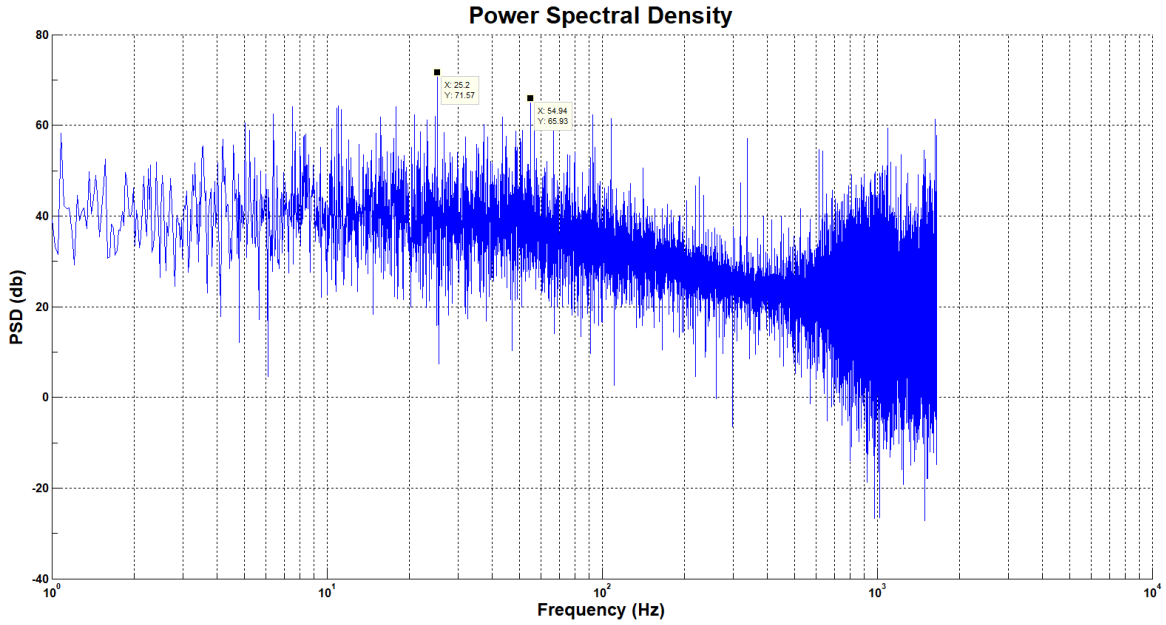

Fig. A-5. Simulated PSD plot of FRF standard deviations with Gaussian noise excitation signal for photovoltaic cell ($R_m = 100\ k\Omega$ and $C_m = 1\ \mu F$)

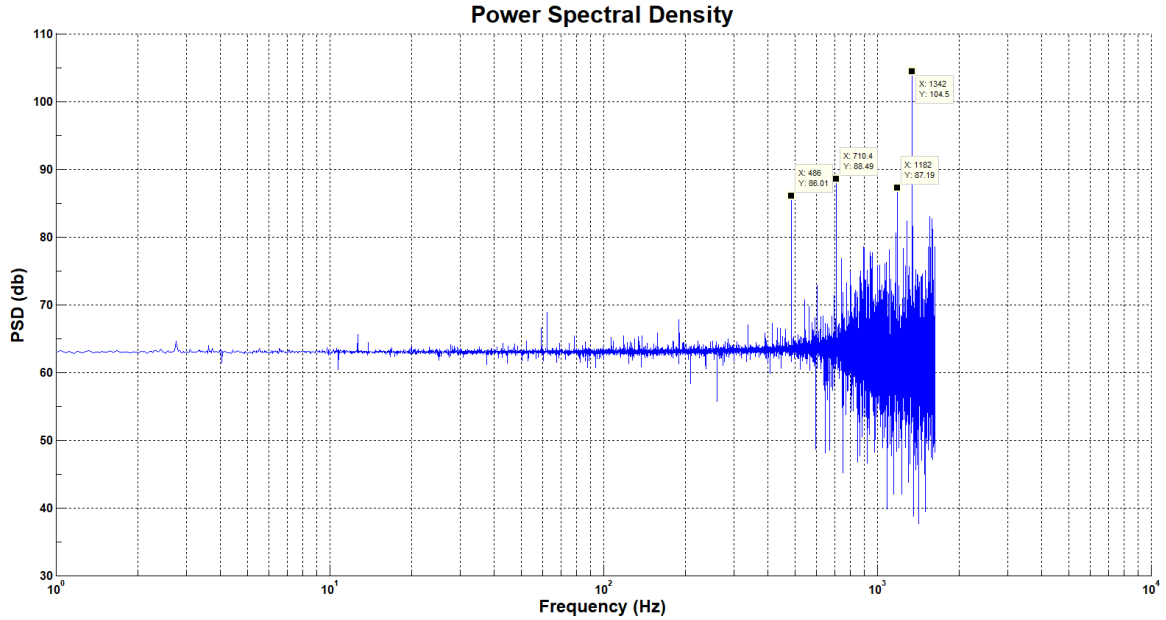

Fig. A-6. Simulated PSD plot of FRF standard deviations with Gaussian noise excitation signal for photovoltaic cell ($R_m = 1\ k\Omega$ and $C_m = 1\ nF$)

APPENDIX B FREQUENCY DOMAIN PHOTOCURRENT MEASUREMENT DATA

B.1 Random-Phase Multisine Excitation with Miniature Inorganic Photovoltaic Cell

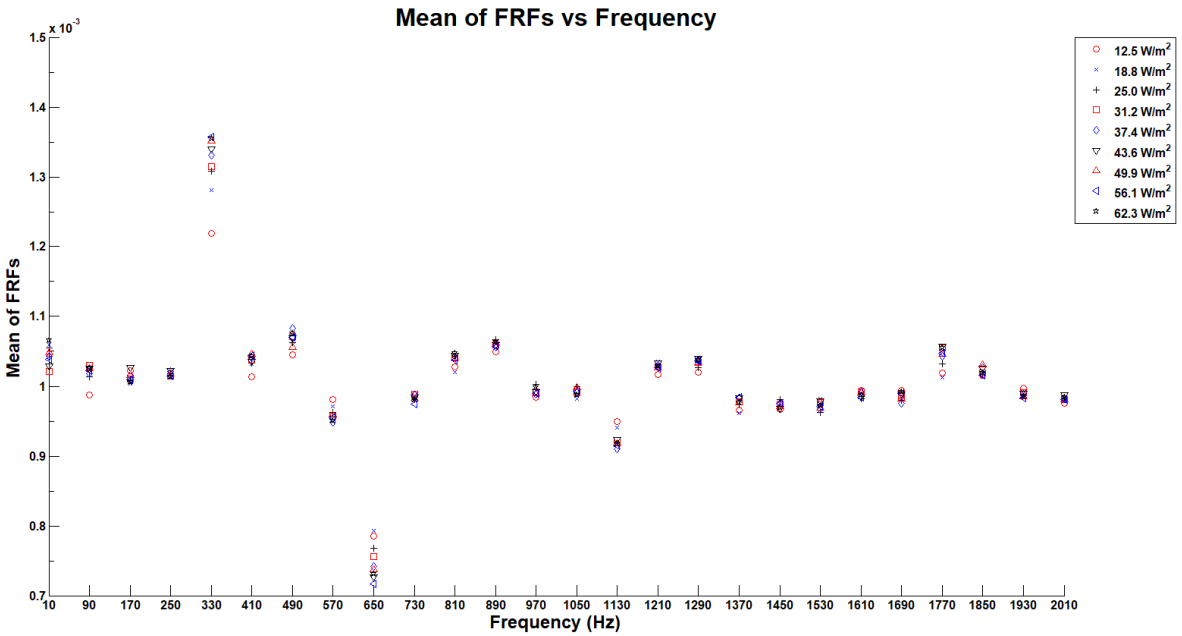

Fig. B-1. FRF mean plot with random phase multisine excitation signal for miniature inorganic photovoltaic cell ($R_m = 10\ k\Omega$ and $C_m = 1\ \mu F$)

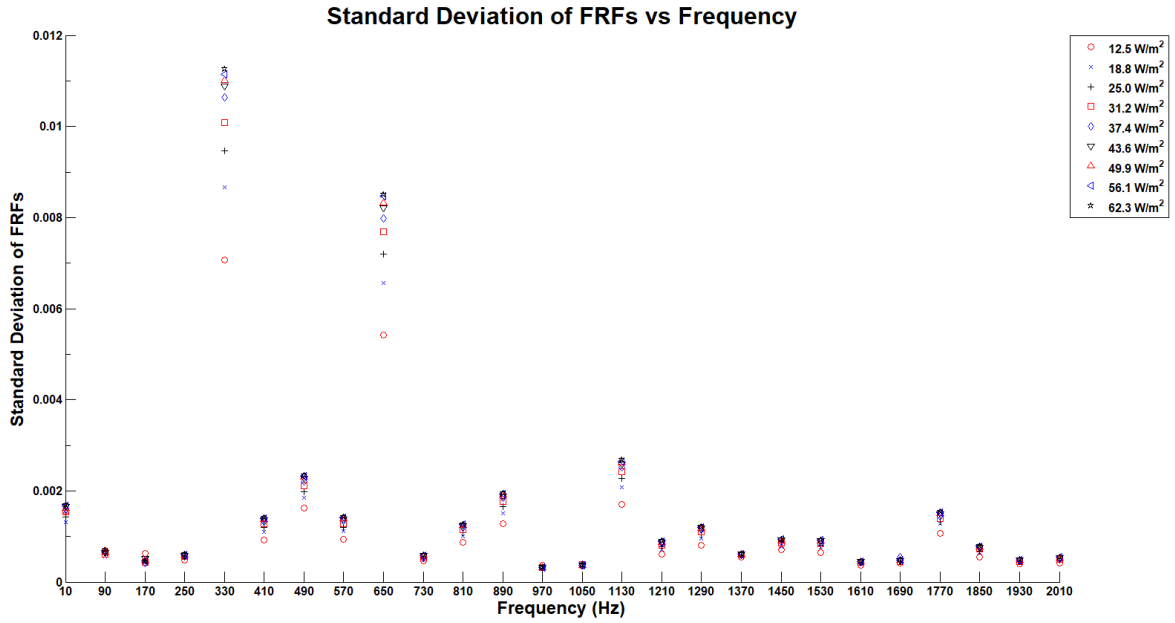

Fig. B-2. FRF standard deviation plot with random phase multisine excitation signal for miniature inorganic photovoltaic cell ($R_m = 10\ k\Omega$ and $C_m = 1\ \mu F$)

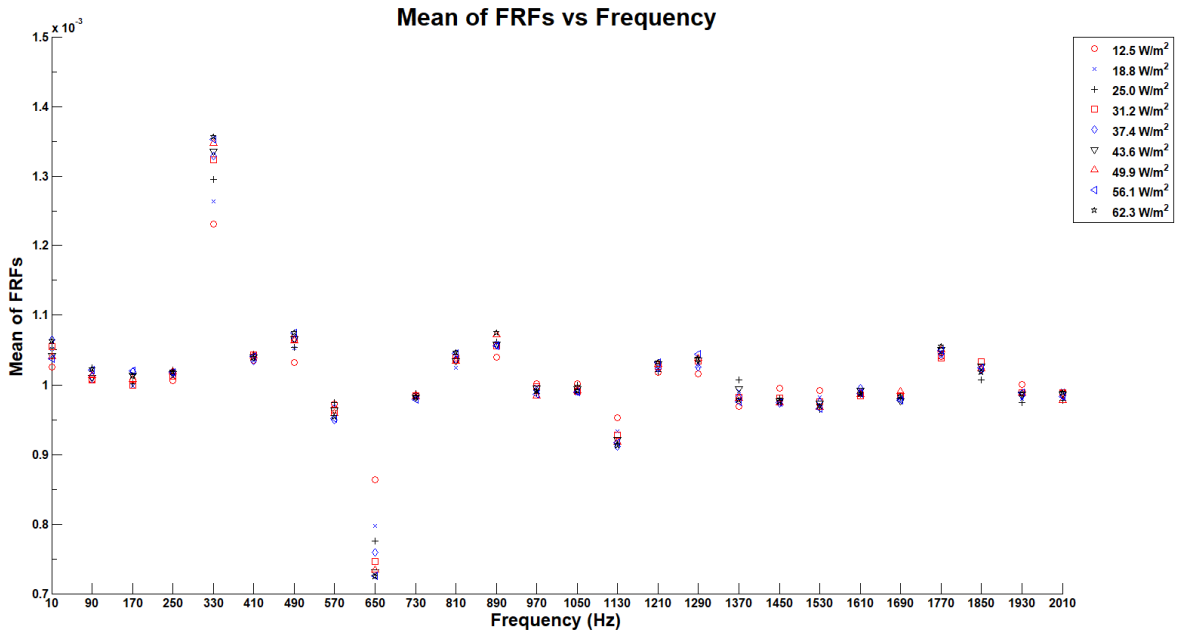

Fig. B-3. FRF mean plot with random phase multisine excitation signal for miniature inorganic photovoltaic cell ($R_m = 100\ k\Omega$ and $C_m = 1\ \mu F$)

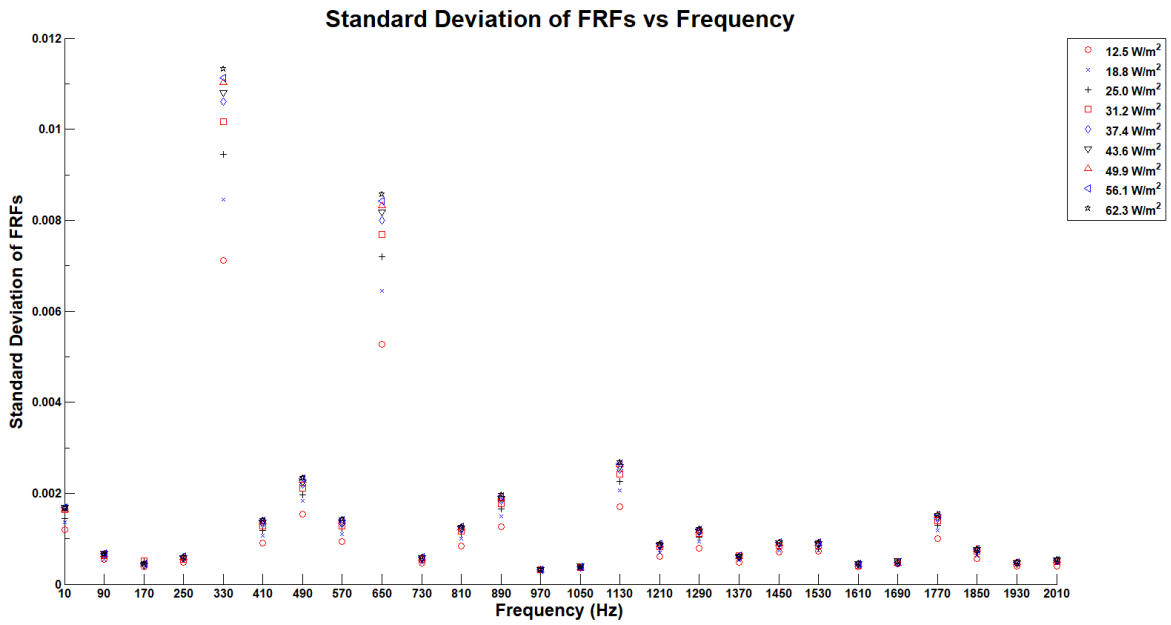

Fig. B-4. FRF standard deviation plot with random phase multisine excitation signal for miniature inorganic photovoltaic cell ($R_m = 100\ k\Omega$ and $C_m = 1\ \mu F$)

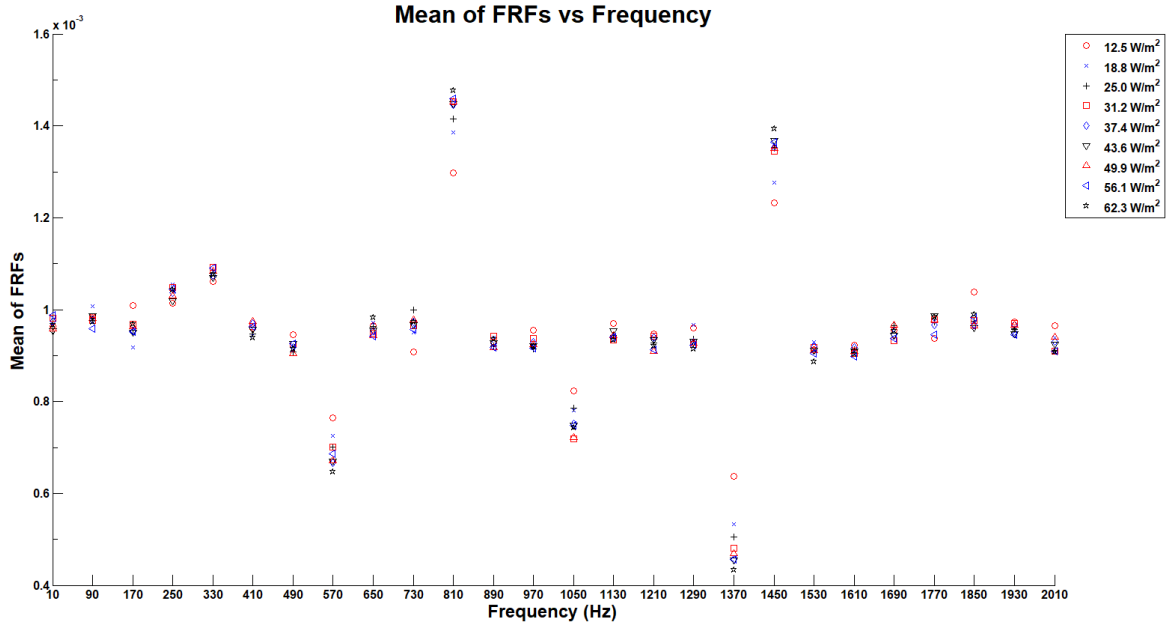

Fig. B-5. FRF mean plot with random phase multisine excitation signal for miniature inorganic photovoltaic cell ($R_m = 1\ k\Omega$ and $C_m = 1\ nF$)

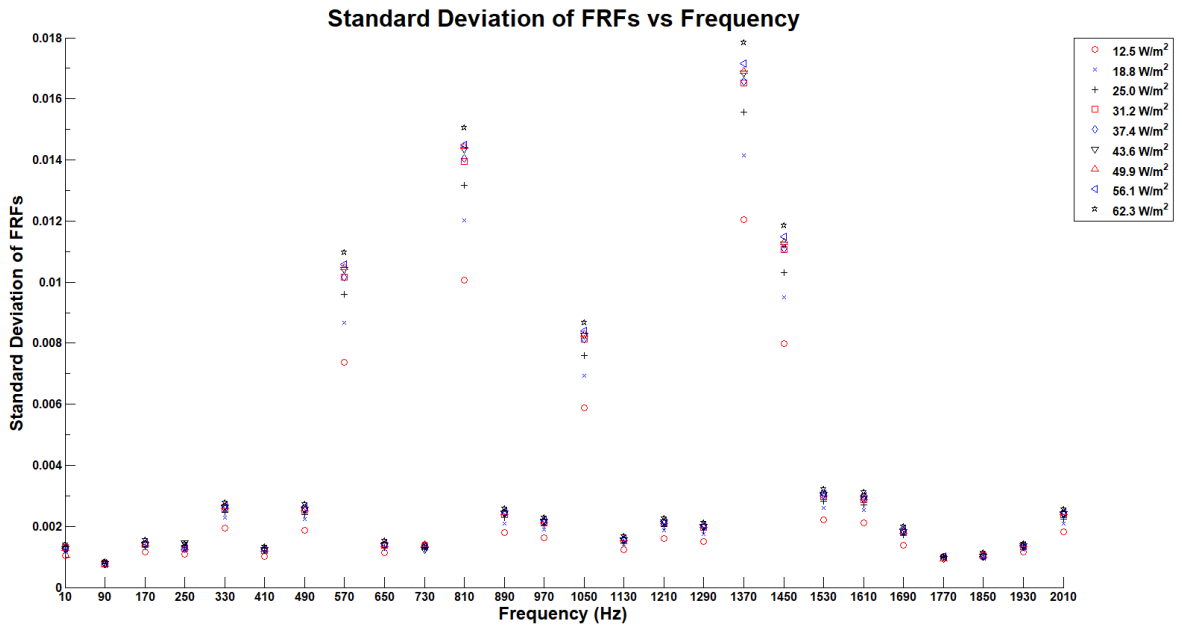

Fig. B-6. FRF standard deviation plot with random phase multisine excitation signal for miniature inorganic photovoltaic cell ($R_m = 1\ k\Omega$ and $C_m = 1\ nF$)

B.2 Gaussian Noise Excitation with Miniature Inorganic Photovoltaic Cell

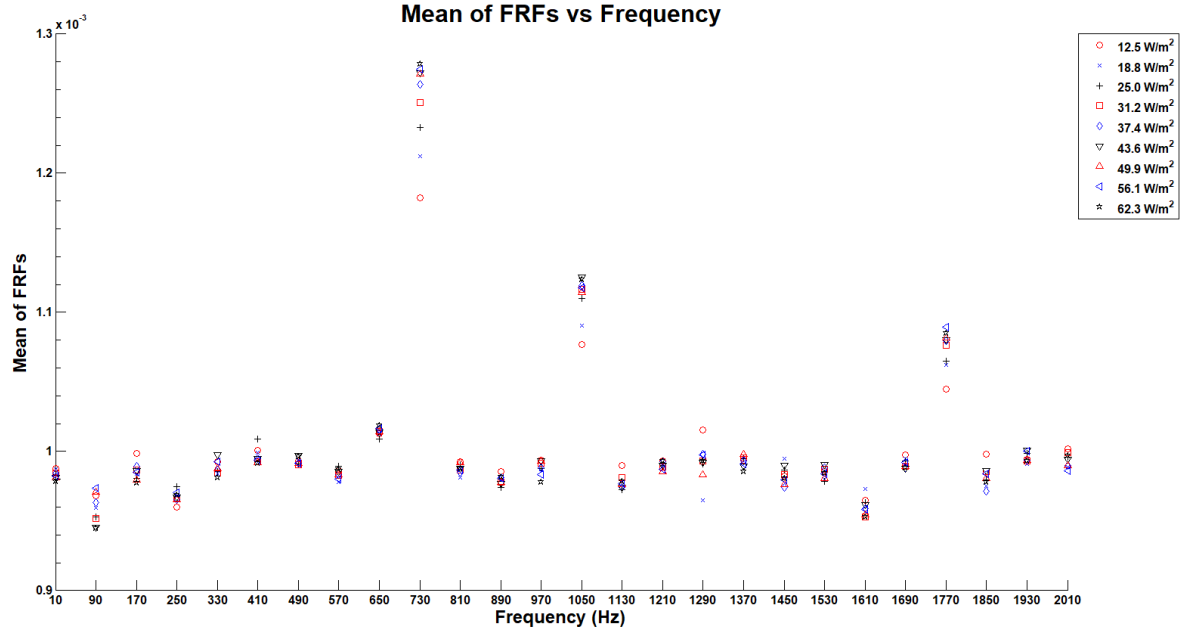

Fig. B-7. FRF mean plot with Gaussian noise excitation signal for miniature inorganic photovoltaic cell ($R_m = 10\ k\Omega$ and $C_m = 1\ \mu F$)

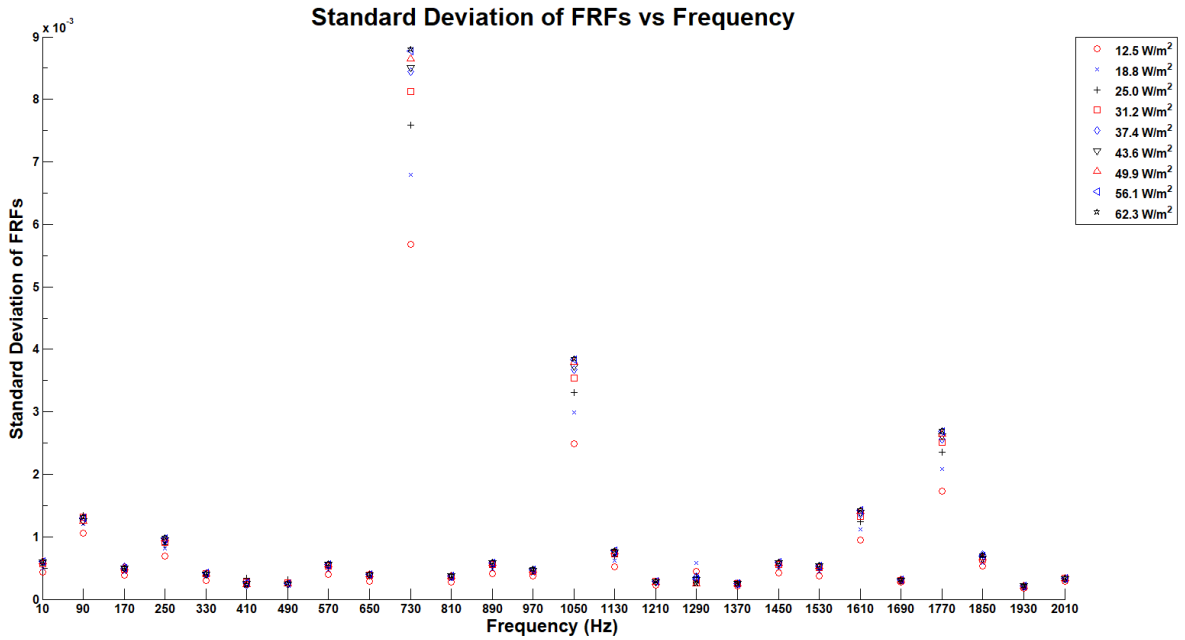

Fig. B-8. FRF standard deviation plot with Gaussian noise excitation signal for miniature inorganic photovoltaic cell ($R_m = 10\ k\Omega$ and $C_m = 1\ \mu F$)

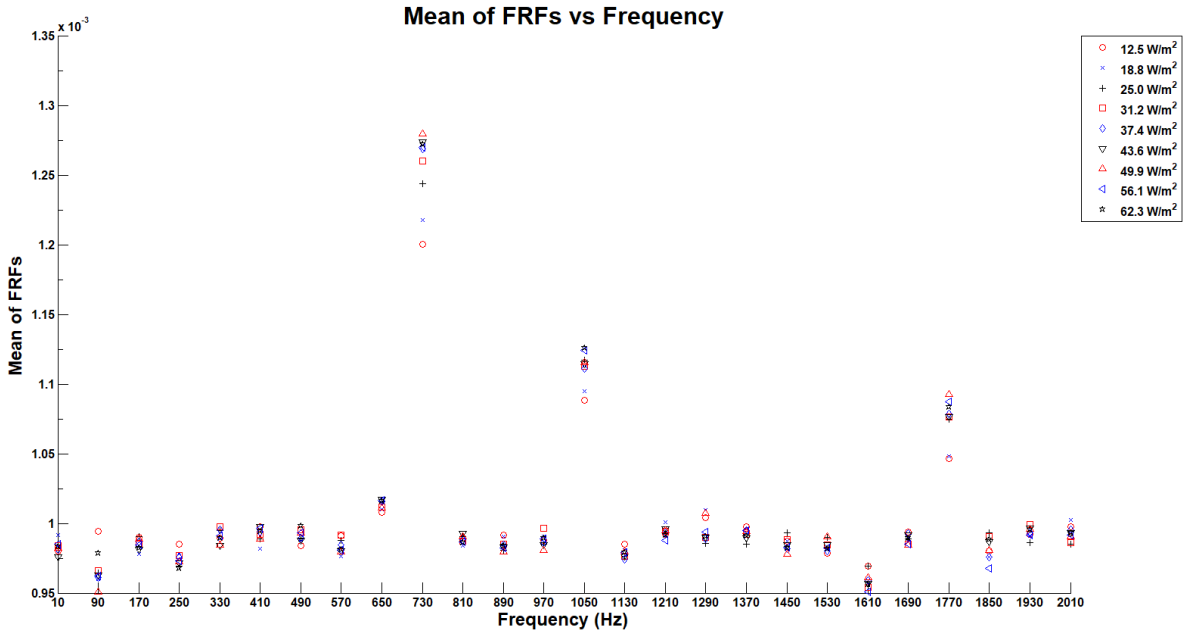

Fig. B-9. FRF mean plot with Gaussian noise excitation signal for miniature inorganic photovoltaic cell ($R_m = 100\ k\Omega$ and $C_m = 1\ \mu F$)

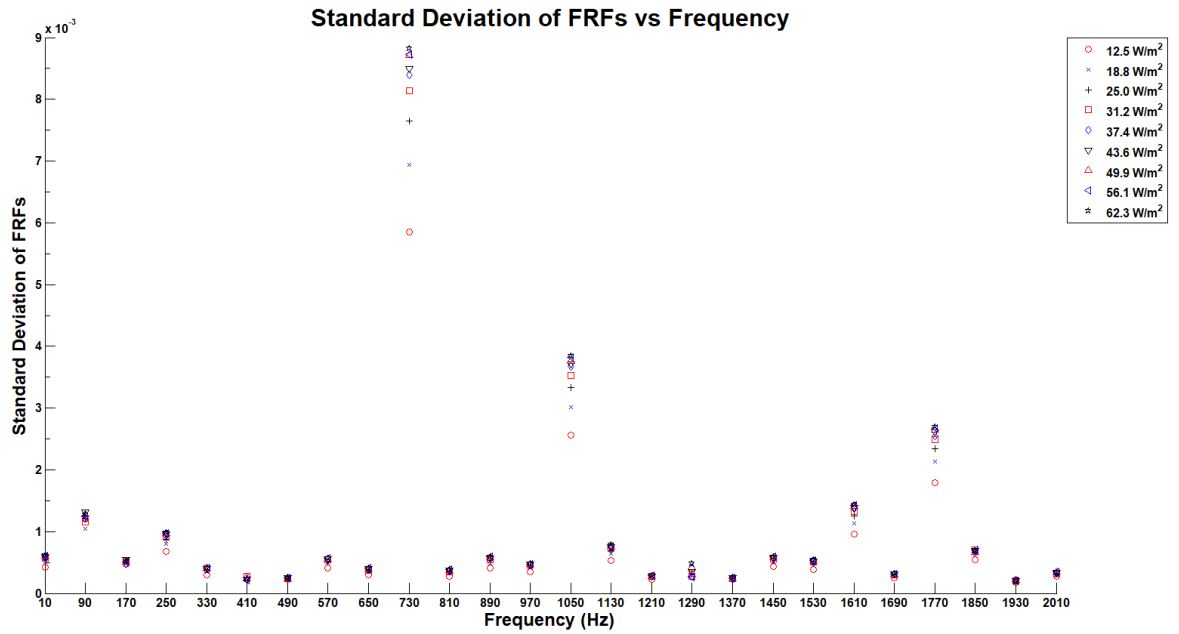

Fig. B-10. FRF standard deviation plot with Gaussian noise excitation signal for miniature inorganic photovoltaic cell ($R_m = 100\ k\Omega$ and $C_m = 1\ \mu F$)

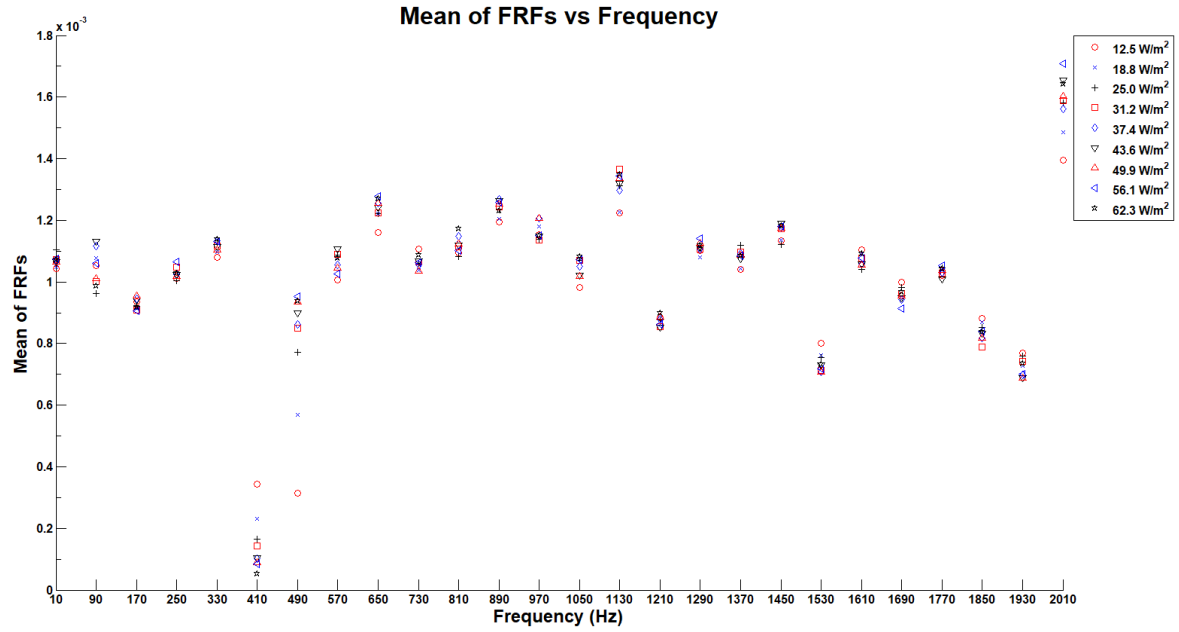

Fig. B-11. FRF mean plot with Gaussian noise excitation signal for miniature inorganic photovoltaic cell ($R_m = 1\ k\Omega$ and $C_m = 1\ nF$)

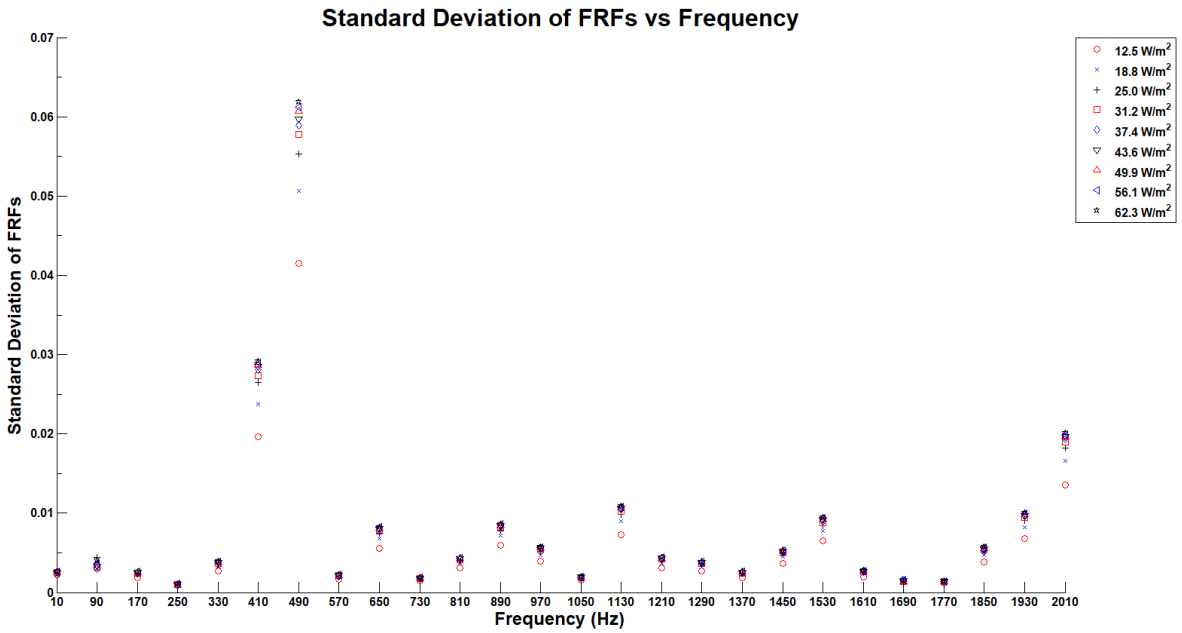

Fig. B-12. FRF standard deviation plot with Gaussian noise excitation signal for miniature inorganic photovoltaic cell ($R_m = 1\ k\Omega$ and $C_m = 1\ nF$)

B.3 Gaussian Noise Excitation with Organic Photovoltaic Cell

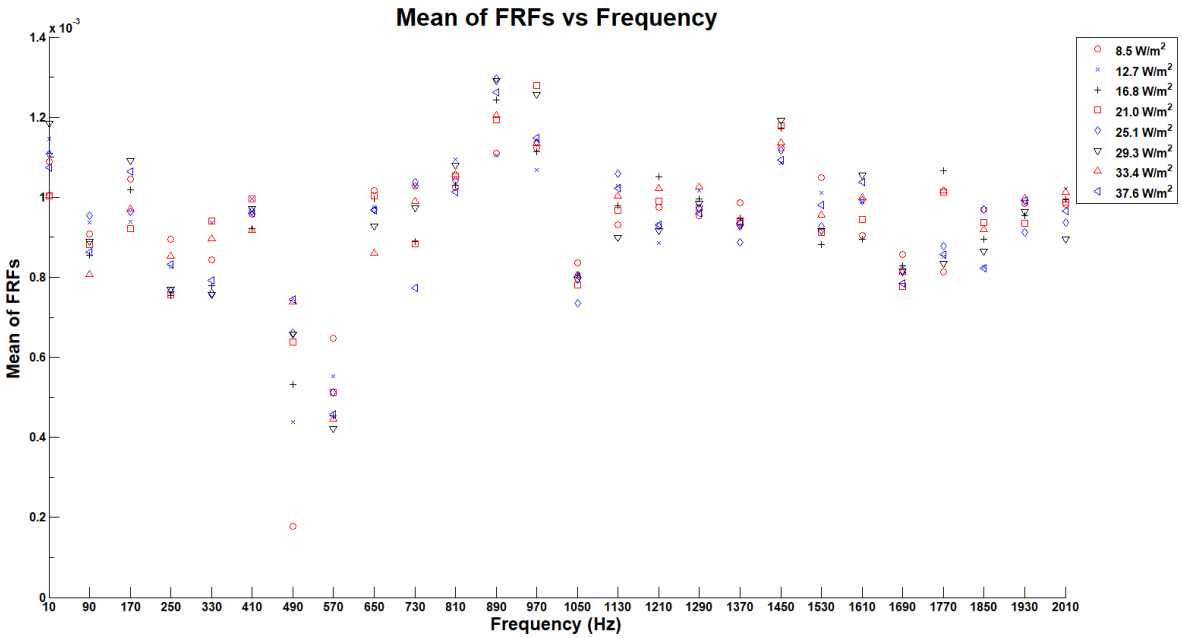

Fig. B-13. FRF mean plot with Gaussian noise excitation signal for OPV cell ($R_m = 100\ k\Omega$ and $C_m = 1\ \mu F$)

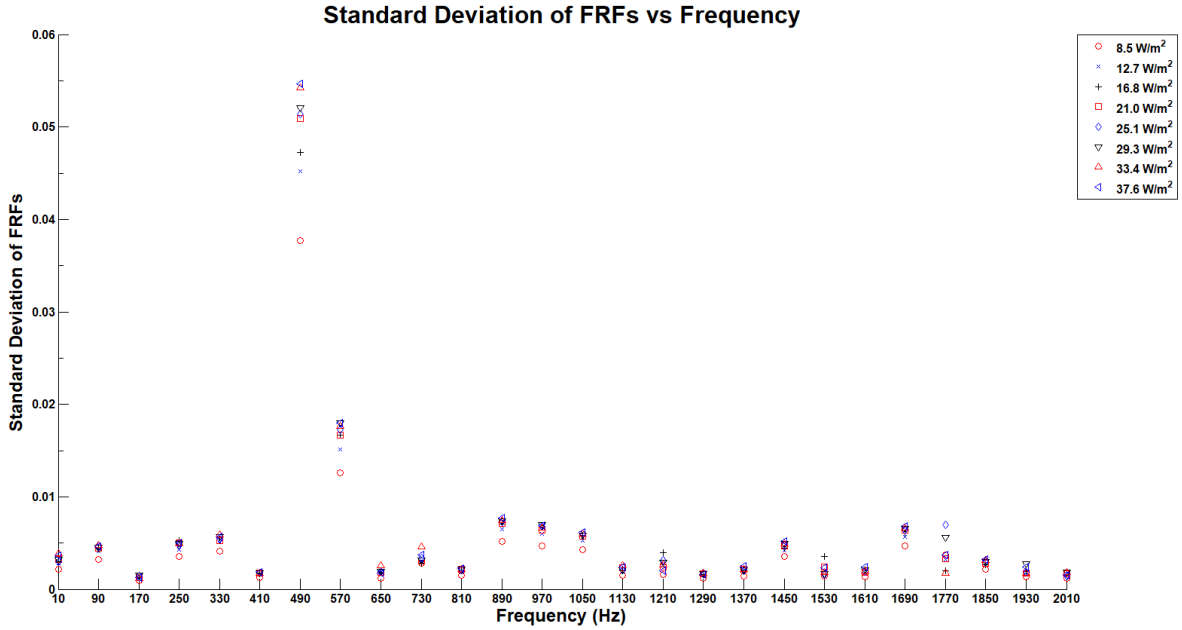

Fig. B-14. FRF standard deviation plot with Gaussian noise excitation signal for OPV cell ($R_m = 100\ k\Omega$ and $C_m = 1\ \mu F$)

APPENDIX C ORGANIC PHOTOVOLTAIC CELLS

The fabrication works were carried out by Ossila Ltd in their Kroto Innovation Centre at The University of Sheffield on 21/05/2014 after receiving the order for the required samples and composition of the organic materials for the organic photovoltaic (OPV) cells.

(click on the object to view the embedded pdf file)

Fabrication Routine

Substrate cleaning:

- 5 min sonication in hot 1% Hellmanex
- 2x hot DI water dump rinse + 1x DI dump rinse
- 5 min sonication in IPA
- 2x DI water dump rinse
- 5 min sonication in hot 10% NaOH
- 2x DI water dump rinse
- Stored in DI until next step
- N2 blow dry

PEDOT:PSS

- Spin coated at 5000 rpm for 30s
- Dynamic dispense of 30 ul
- DI water cathode strip wipe
- Baked at 150C until transfer to glovebox
- Thickness ~30 nm
- Films annealed to 150 C for ~40 mins inside glovebox

Active layer solution preparation

- Fresh stock solution of PCDTBT (chlorobenzene-fraction) prepared in N2
- Concentration of 4 mg/ml in chlorobenzene solvent
- Dissolved with stirbar for ~80 mins on hotplate at 80C
- Cooled for 10 mins
- Mixed with dry $PC_{70}BM$ in blend ratio of 1:4 for a total concentration of 20 mg/ml
- Dissolved with stirbar for ~16.5hrs on hotplate at 80C
- Cooled for ~1hr
- Filtered through 0.45 um PTFE filter

Active Layer

- Calculated thickness from Dektak measurement of 800 rpm film (~66 nm)
- Thicknesses of ~70 nm at 710 rpm, ~90 nm at 430 rpm
- Dynamic dispense of 25 ul for 30s
- 90 nm films experienced a subsequent step of 2000 rpm for 5s to remove excess material
- Methanol (MeOH) wash spun at 4000 rpm for 30s immediately after active layer
- Chlorobenzene cathode strip wipe

Cathode Deposition

- 2.5 nm Ca at 0.2-0.4 A/s
- 100 nm Al at 1.4-1.6 A/s
- Maximum deposition pressure of 4E-07

Annealing

- Annealed at 80C for 10 mins on hotplate after cathode deposition, quick cooldown

Encapsulation

- Ossila EE1 encapsulation with glass coverslip
- 30 mins curing using MEGA LV202E
-

Measurements

- JV sweeps taken with Keithley 237 source-meter
- Illumination by Newport Oriel 9225-1000 solar simulator with 100 mW/cm^2 AM1.5 output
- NREL certified silicon reference cell used to calibrate
- Lamp current: 7.9 A
- Solar output at start of testing: 1 suns at 24 C
- Solar output at end of testing: 1 suns at 25 C
- Air cooled substrates
- Calibrated aperature mask of size 0.256 mm^2

Glovebox values

- During active layer
  - H2O < 0.1 ppm
  - O2 ~ 4.6 ppm
- During annealing and encapsulation
  - H2O < 0.1 ppm
  - O2 ~ 11.6 ppm

APPENDIX D MATLAB SCRIPTS FOR EXCITATION SIGNAL GENERATION

D.1 Random Phase Multisine Signal Generation

Filename: .\Monash\Research\Test\Simulation\Matlab\multi_sine_rev_ss.m

```
%Mfile for random phase multi-sine generation

clear all;
close all;
clc;

Len     = 2^12;
T       = 1e-1;
fs      = Len/T;
Freq    = ([0:Len-1])*fs/Len;

ptFreq  = (1:8:201);
f0      = 1/T;
f       = ptFreq*f0;
A       = 0.3*ones(size(f));

Ts      = 1/fs;
t       = (0:Ts:T-Ts);

phi = pi-rand(size(f))*2*pi;
%phi = pi-rand(1,1)*2*pi;

vsupply = A*sin(2*pi*f'*t+repmat(phi',[1,Len]));

vsupply_norm = vsupply./sqrt(mean(vsupply.^2));

VS  = fft(vsupply_norm)/Len;

figure(1)
set(gcf,'color','w')
subplot(2,1,1)
plot(t,vsupply_norm,'.')
title('Random Phase Multi-Sine Plot', 'fontsize', 24, 'FontWeight', 'bold')
xlabel('Time (s)', 'fontsize', 18, 'FontWeight', 'bold')
ylabel('Amplitude', 'fontsize', 18, 'FontWeight', 'bold')
set(gca, 'box', 'off', 'FontSize', 12, 'FontWeight', 'bold', 'YMinorTick', 'on')
grid on

subplot(2,1,2)
%stem(Freq, abs(VS))  % Double sided spectrum
stem(Freq(1:Len/2), 2*abs(VS(1:Len/2)))  % Single sided spectrum
title('Random Phase Multi-Sine Spectrum', 'fontsize', 24, 'FontWeight', 'bold')
xlabel('Frequency (Hz)', 'fontsize', 18, 'FontWeight', 'bold')
ylabel('Intensity', 'fontsize', 18, 'FontWeight', 'bold')
set(gca, 'box', 'off', 'FontSize', 12, 'FontWeight', 'bold', 'YMinorTick', 'on')
grid on
ylim([0,0.3])

pathName = 'C:\Temp\Matlab Data Files';

multisine_fname    = 'multisine.csv';
multisine_f2w = strcat(pathName, '\', multisine_fname);

csvwrite(multisine_f2w, vsupply_norm);
```

D.2 Gaussian Noise Signal Generation

Filename: .\Monash\Research\Test\Simulation\Matlab\gaussian_noise_rev_ss.m

```
%Mfile for Gaussian noise generation

clear all;
close all;
clc;

Len     = 2^12;
T       = 1e-1;
fs      = Len/T;
Freq    = ([0:Len-1])*fs/Len;

ptFreq  = (1:8:201);
f0      = 1/T;
f       = ptFreq*f0;
A       = 1;
Offset  = 0;

Ts      = 1/fs;
t       = (0:Ts:T-Ts);

vsupply = Offset + A*randn(1,Len);

vsupply_norm = vsupply./sqrt(mean(vsupply.^2));

VS  = fft(vsupply_norm)/Len;

figure(1)
set(gcf,'color','w')
subplot(2,1,1)
plot(t,vsupply_norm,'.')
title('Gaussian Noise Plot', 'fontsize', 24, 'FontWeight', 'bold')
xlabel('Time (s)', 'fontsize', 18, 'FontWeight', 'bold')
ylabel('Amplitude', 'fontsize', 18, 'FontWeight', 'bold')
set(gca, 'box', 'off', 'FontSize', 12, 'FontWeight', 'bold', 'YMinorTick', 'on')
grid on

subplot(2,1,2)
%stem(Freq, abs(VS))  % Double sided spectrum
stem(Freq(1:Len/2), 2*abs(VS(1:Len/2)))  % Single sided spectrum
title('Gaussian Noise Spectrum', 'fontsize', 24, 'FontWeight', 'bold')
xlabel('Frequency (Hz)', 'fontsize', 18, 'FontWeight', 'bold')
ylabel('Intensity', 'fontsize', 18, 'FontWeight', 'bold')
set(gca, 'box', 'off', 'FontSize', 12, 'FontWeight', 'bold', 'YMinorTick', 'on')
grid on
ylim([0,0.2])

pathName = 'C:\Temp\Matlab Data Files';

gaussian_fname    = 'gaussian_noise.csv';
gaussian_f2w = strcat(pathName, '\', gaussian_fname);

csvwrite(gaussian_f2w, vsupply_norm);
```

APPENDIX E MATLAB / SIMULINK MODEL OF MEASUREMENT CIRCUIT

E.1 Custom Simscape Model for Diffusion Capacitance

Filename:

.\Documents\MATLAB\Simulink\+SimscapeCustomBlocks\+Electrical\diffusion_cap_new.sc

```
component diffusion_cap_new
% Diffusion Capacitance (New)
% Diffusion capacitance of a semiconductor pn-junction;
% Cd = Cd0 * exp(Vs/Vt-1)

nodes
   p = foundation.electrical.electrical; % +: left
   n = foundation.electrical.electrical; % -: right
end

parameters
   Kd = { 1000e-12, 'F' };            % Diffusion Capacitance at zero bias
   Is = { 0.1e-15, 'F' };             % Reverse saturation current or leakage current
   nd = 2;                            % Diode Ideality Factor
   k = { 1.3806503e-23, 'J/K' };      % Boltzman constant
   T  = { 300, 'K' };                 % Current Temperature
   q = { 1.602176e-19, 'A*s' };       % Electron charge

   r  = { 1e-6, 'Ohm' };          % Series resistance
   g  = { 0, '1/Ohm' };           % Parallel conductance
end

variables
   Cd  = { 0, 'F' };   % Capacitance
   Vs = { 0, 'V' };  % Capacitor voltage
   v = { 0, 'V' };
   i = { 0, 'A' };
end

function setup
   across(v, p.v, n.v);
   through(i, p.i, n.i);

   %if cd <= 0
      %pm_error('simscape:GreaterThanZero','Capacitance')
   %end
   if g < 0
      pm_error('simscape:GreaterThanOrEqualToZero','Parallel conductance')
   end
   if g == {inf, '1/Ohm'}
      pm_error('simscape:LessThan','Parallel conductance','inf')
   end
   if r < 0
      pm_error('simscape:GreaterThanOrEqualToZero','Series resistance')
   end
   if r == {inf, 'Ohm'}
      pm_error('simscape:LessThan','Series resistance','inf')
   end
end

equations
   Cd == Kd*exp(Vs/(nd*k*T/q)-1);
   v == i*r + Vs;
   i == Cd*Vs.der + g*Vs;
end

end
```

E.2 Custom Simscape Model for Depletion Capacitance

Filename:

.\Documents\MATLAB\Simulink\+SimscapeCustomBlocks\+Electrical\depletion_cap_new.ssc

```
component depletion_cap_new
% Depletion Capacitance (New)
% Depletion (a.k.a Transition) capacitance of a semiconductor pn-junction,
% Ct = Cj0 / (1 - Vs/Vbi)^m

nodes
   p = foundation.electrical.electrical; % +: left
   n = foundation.electrical.electrical; % -: right
end

parameters
   Cj0 = { 0.1e-15, 'F' };      % SCR Capacitance at zero bias
   Vbi = { 0.65, 'V' };          % SCR built-in potential
   m = 1/3;                      % Junction grading coefficient, ~ 0.33 - 0.5
   k = { 1.3806503e-23, 'J/K' };    % Boltzman constant
   T  = { 300, 'K' };                % Current Temperature
   q = { 1.602176e-19, 'A*s' };     % Electron charge

   r  = { 1e-6, 'Ohm' };        % Series resistance
   g  = { 0, '1/Ohm' };         % Parallel conductance
end

variables
   Ct  = { 0, 'F' };   % Capacitance
   Vs = { 0, 'V' };  % Capacitor voltage
   v = { 0, 'V' };
   i = { 0, 'A' };
end

function setup
   across(v, p.v, n.v);
   through(i, p.i, n.i);

   %if cj <= 0
      %pm_error('simscape:GreaterThanZero','Capacitance')
   %end
   if g < 0
      pm_error('simscape:GreaterThanOrEqualToZero','Parallel conductance')
   end
   if g == {inf, '1/Ohm'}
      pm_error('simscape:LessThan','Parallel conductance','inf')
   end
   if r < 0
      pm_error('simscape:GreaterThanOrEqualToZero','Series resistance')
   end
   if r == {inf, 'Ohm'}
      pm_error('simscape:LessThan','Series resistance','inf')
   end
end

equations
   Ct == Cj0/(1 - (Vs/Vbi) + (k*T/q)/(2*Vbi)*exp((Vs - Vbi)/(k*T/q)))^m;
   v == i*r + Vs;
   i == Ct*Vs.der + g*Vs;
end

end
```

E.3 Matlab Script for Set-up of Simulation Parameters

Filename:

.\Monash\Research\Test\Simulation\Matlab\Circuit Analysis\pv_nonlinearity_sim_setup.m

```
clear all;
close all;
clc;

set_param('rc_photodetector_vex_ind/Rsh', 'R', '10e+3');
set_param('rc_photodetector_vex_ind/Rs', 'R', '10');
set_param('rc_photodetector_vex_ind/Rp', 'R', '1');
set_param('rc_photodetector_vex_ind/Ri', 'R', '1');
set_param('rc_photodetector_vex_ind/Rm', 'R', '1e+3');
set_param('rc_photodetector_vex_ind/Cm', 'C', '1e-6');
set_param('rc_photodetector_vex_lcr_new/Ls', 'L', '90e-6');

set_param('rc_photodetector_vex_ind/Current Gain', 'K', '1/1e+5');

fs = 40.96e+3; % Sampling rate
set_param('rc_photodetector_vex_ind/Sample and Hold', 'Ts', '1/fs');

%Set the irradiance
G=200;
```

APPENDIX F LABVIEW VI PROGRAM DEVELOPMENT

F.1 Labview VI Program for Random Phase Multisine Generation

Filename:

.\Monash\Research\Test\Measurement\LabVIEW\multisine_waveform_generation_rev3.vi

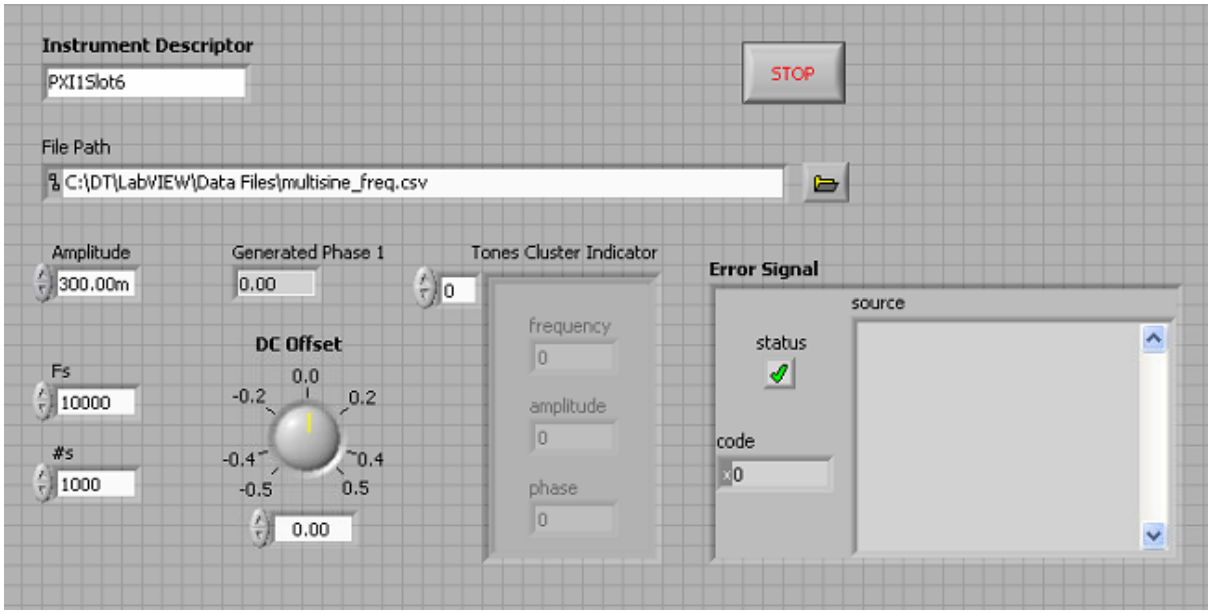

Fig. E-1. Front panel of random phase multisine generation

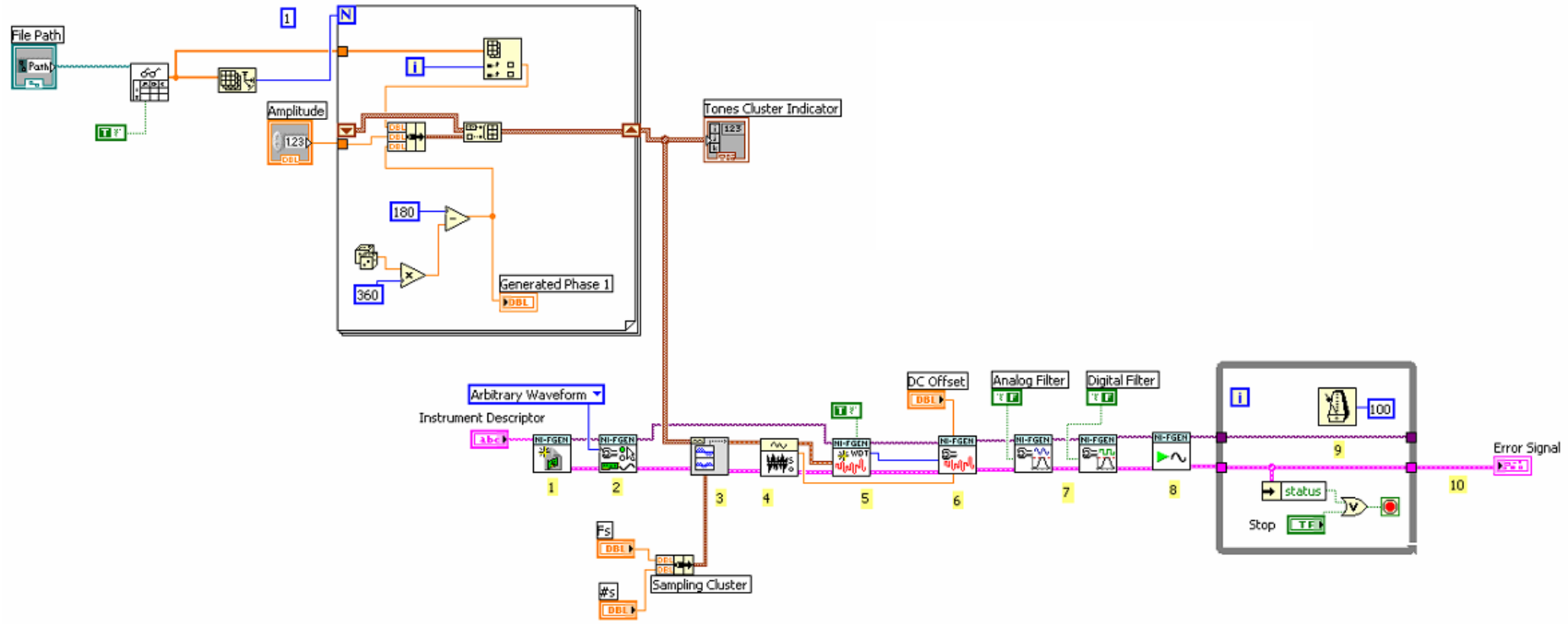

Fig. E-2. Block diagram of random phase multisine generation

F.2 LABVIEW VI Program for Gaussian Noise Generation

Filename:

.\Monash\Research\Test\Measurement\LabVIEW\niFgen_Create_Gaussian_Noise_From_Data.vi

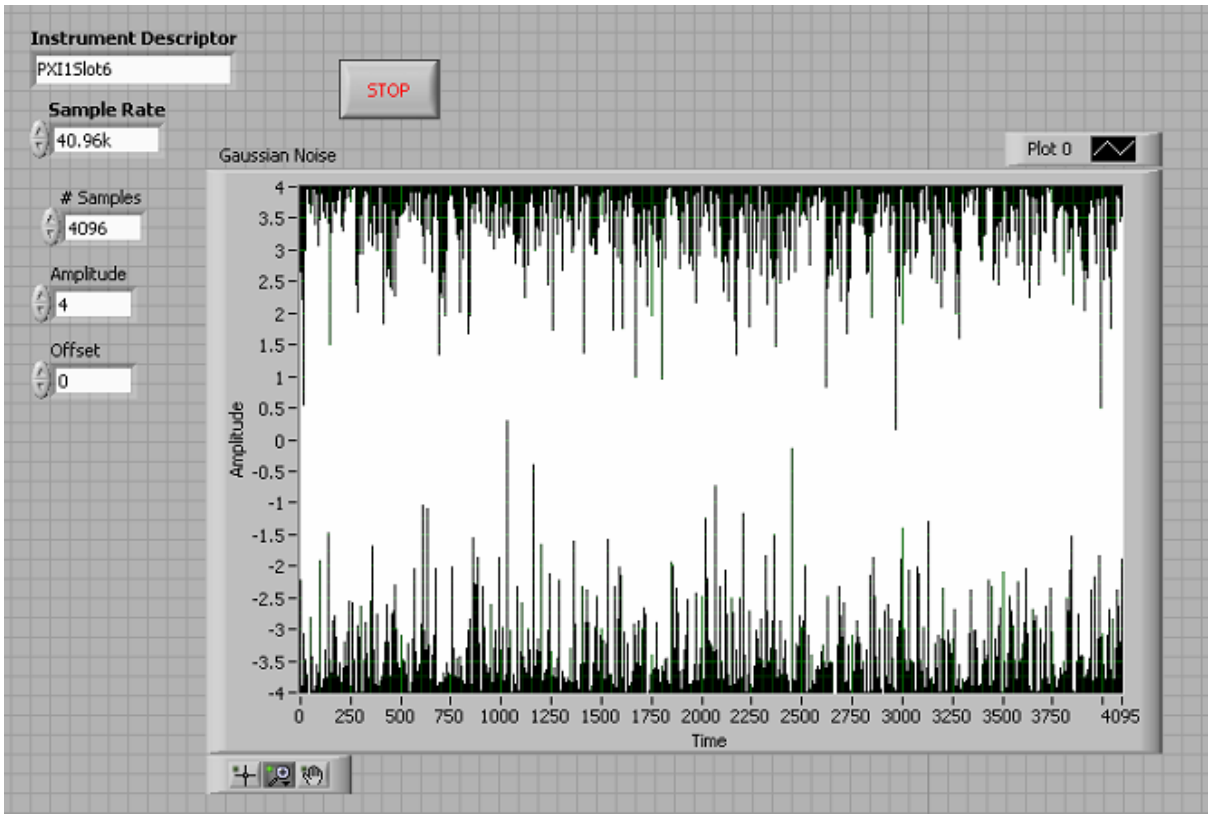

Fig. E-3. Front panel of Gaussian noise generation

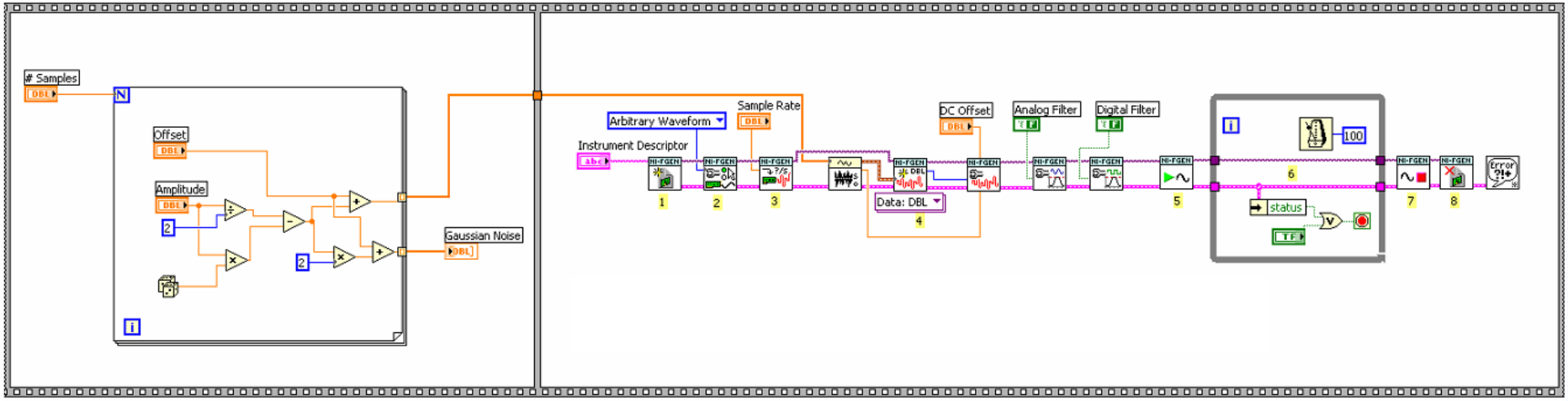

Fig. E-4. Block diagram of Gaussian noise generation

F.3 LABVIEW VI Program for Automated Measurement & Data Collection

Filename:

.\Monash\Research\Test\Measurement\LabVIEW\niScope EX Save to File with FFT_rev2.vi

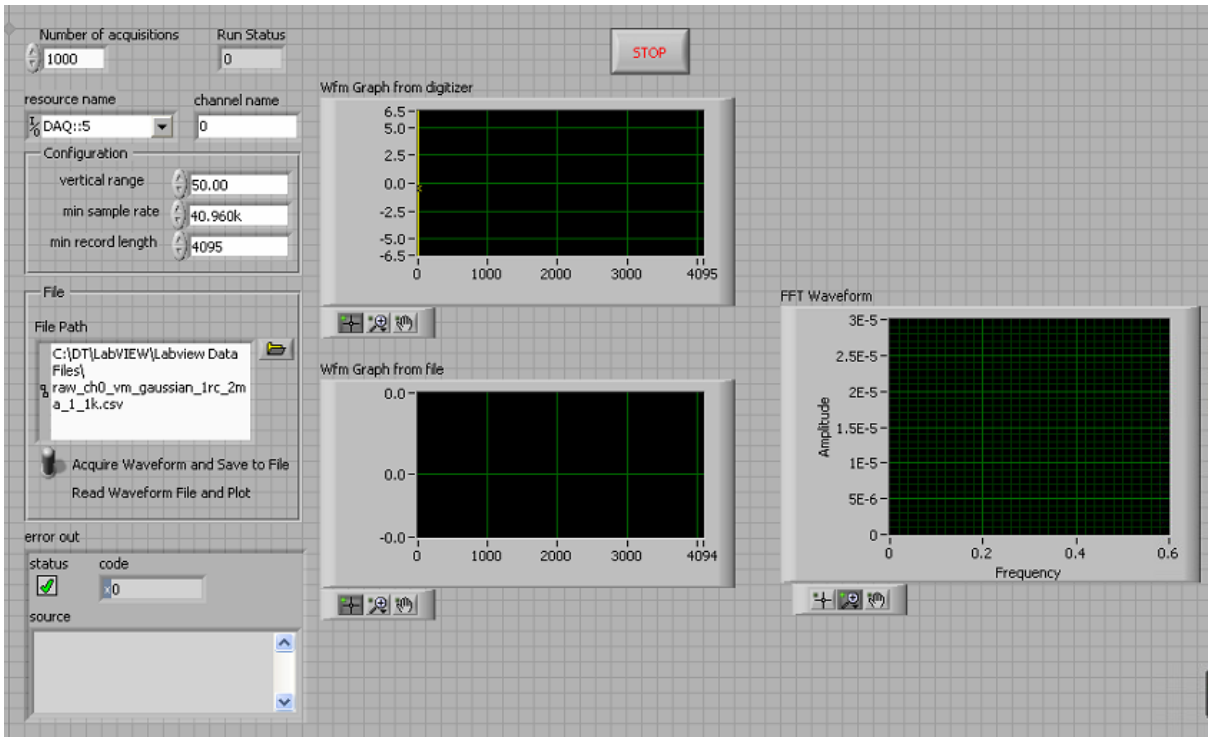

Fig. E-5. Front panel for automated measurement and data collection

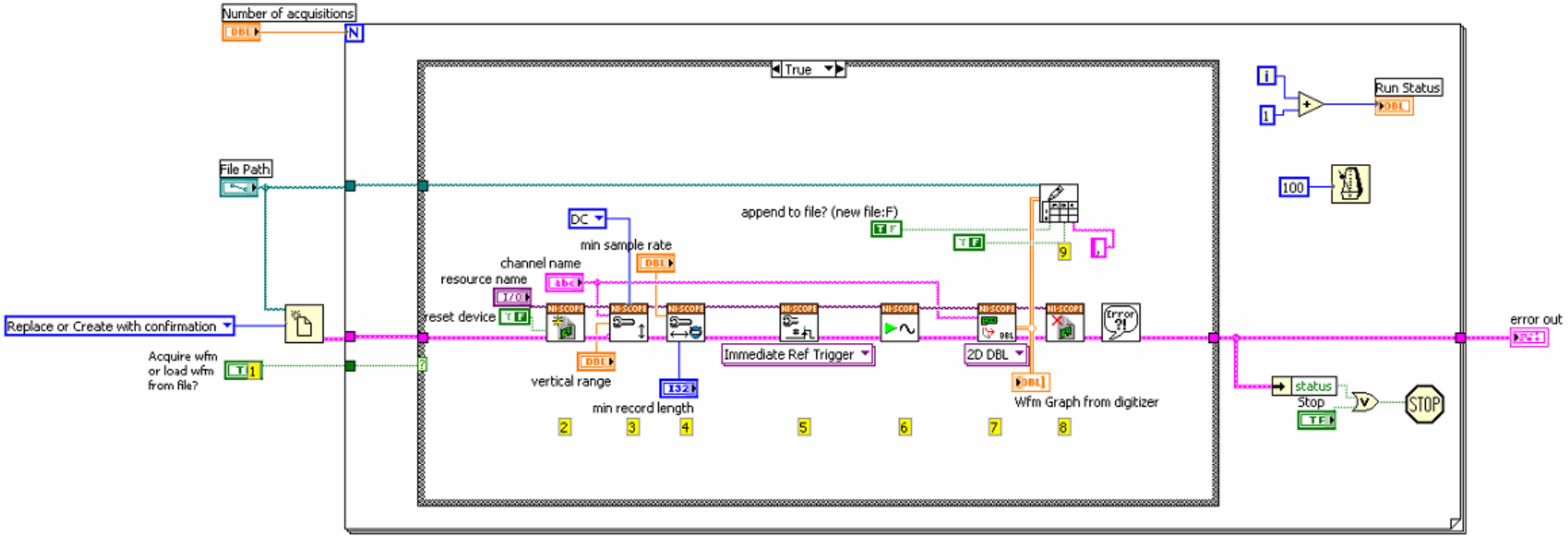

Fig. E-6. Block diagram of automated measurement and data collection

APPENDIX G MATLAB SCRIPTS TO PROCESS MEASUREMENT DATA

G.1 Script for statistical computation on measurement data with random phase multisine excitation signal

Filename: .\Monash\Research\Test\Simulation\Matlab\frf_xlsfile_loop_msine_1rc.m

```
clear all;
close all;
clc;

Len     = 2^12;
T       = 0.1;                  %Input Signal Period = 0.1s
f0      = 1/T;                  %Input Signal Frequency = 10Hz

ptFreq  = [1:8:201];
f       = ptFreq*f0;

fs      = Len/T;                %Sampling Frequency = 4096 x 10 = 40.96kHz

Freq    = ([0:Len-1])/Len*fs;

Ri      = 1e+3;
Rs      = 1;

NumLoop = 1000;

IphList = [2 3 4 5 6 7 8 9 10];  %Photocurrent; set number of runs

%%%%%%%%%%%%%%%%%%%%%%%%%%%%%%%%%%%%%%%%%%%%%%%%%%%%%%%%%%%%%%%
%%%%%%%%%%%%
%File I/O
pathName = 'C:\Temp\Labview\Labview Data Files 1k';
%pathName = 'C:\Temp\Labview\Labview Data Files 10k';
%pathName = 'C:\Temp\Labview\Labview Data Files 100k';

fileList_vm      = dir(fullfile(pathName, 'raw_ch0_vm_msine_1rc_*.csv'));

mean_fname    = 'mean_frf_msine_1rc_1k.csv';
mean_f2w = strcat(pathName, '\', mean_fname);

std_fname     = 'std_frf_msine_1rc_1k.csv';
std_f2w = strcat(pathName, '\', std_fname);

%%%%%%%%%%%%%%%%%%%%%%%%%%%%%%%%%%%%%%%%%%%%%%%%%%%%%%%%%%%%%%%
%%%%%%%%%%%%

vsupply_f2r = strcat(pathName, '\', 'raw_ch1_vsupply_msine.csv');
vsupply_data = csvread(vsupply_f2r);

for index = 1 : length(IphList)
    Iph = IphList(index);

    vm_f2r = fullfile(pathName, fileList_vm(index).name);
    vm_data = csvread(vm_f2r);

    isupply = (vsupply_data - vm_data)/Ri;

    ISUPPLY = fft(isupply)/Len;

    VSUPPLY = fft(vsupply_data)/Len;

    for loop = 1 : NumLoop
        I_BLA(loop,:) = ISUPPLY(loop,ptFreq+1)./VSUPPLY(loop,ptFreq+1);
    end

    I_BLA_Mean(index,:) = mean(I_BLA,1);
    I_BLA_Std(index,:) = std(I_BLA,0,1);
```

```
  format short;
  legendInfo{index} = ['Iph = ' sprintf('%0.3e',Iph)];

  m = {'+','o','*','.','x','s','d','^','v','>','<','p','h'};
  set_marker_order = @() set(gca(), ...
  'LineStyleOrder',m, 'ColorOrder',[0 0 0], ...
  'NextPlot','replacechildren');

  figure(1);
  stem(Freq(ptFreq+1),abs(I_BLA_Mean)');
  xlabel('Frequency(Hz)');
  ylabel('Mean of FRFs');
  title('Mean of FRFs vs Frequency');
  n=get(gca,'Ytick');
  set(gca,'Yticklabel',sprintf('%0.5e |',n));
  legend(legendInfo,'location','NorthEastOutside');
  grid on;

  figure(2);
  stem(Freq(ptFreq+1),abs(I_BLA_Std)');
  xlabel('Frequency(Hz)');
  ylabel('Standard Deviation of FRFs');
  title('Standard Deviation of FRFs vs Frequency');
  n=get(gca,'Ytick');
  set(gca,'Yticklabel',sprintf('%0.5e |',n));
  legend(legendInfo,'location','NorthEastOutside');
  grid on;

  drawnow;
end

m_I_BLA_Mean = [Freq(ptFreq+1);abs(I_BLA_Mean)]';
m_I_BLA_Std = [Freq(ptFreq+1);abs(I_BLA_Std)]';

csvwrite(mean_f2w, m_I_BLA_Mean);
csvwrite(std_f2w, m_I_BLA_Std);
```

G.2 Script for statistical computation on measurement data with Gaussian noise excitation signal

Filename: .\Monash\Research\Test\Simulation\Matlab\frf_xlsfile_loop_gaussian_1rc.m

```
clear all;
close all;
clc;

Len     = 2^12;
T       = 0.1;                %Input Signal Period = 0.1s
f0      = 1/T;                %Input Signal Frequency = 10Hz

ptFreq  = [1:2:201];
f       = ptFreq*f0;

fs      = Len/T;               %Sampling Frequency = 4096 x 10 = 40.96kHz

Freq    = ([0:Len-1])/Len*fs;

Ri      = 1e+3;
Rs      = 1;

NumLoop = 1000;

IphList = [2 3 4 5 6 7 8 9 10];  %Photocurrent; set number of runs

%%%%%%%%%%%%%%%%%%%%%%%%%%%%%%%%%%%%%%%%%%%%%%%%%%%%%%%%%%%%%%%%%%%%%%%%%%%%%%%%%%%
%%%%%%%%%%%%%%%
%File I/O
pathName = 'C:\Temp\Labview\Labview Data Files 1k';
%pathName = 'C:\Temp\Labview\Labview Data Files 10k';
%pathName = 'C:\Temp\Labview\Labview Data Files 100k';
```

```
fileList_vm     = dir(fullfile(pathName, 'raw_ch0_vm_gaussian_1rc_*.csv'));

mean_fname    = 'mean_frf_gaussian_1rc_1k.csv';
mean_f2w = strcat(pathName, '\', mean_fname);

std_fname     = 'std_frf_gaussian_1rc_1k.csv';
std_f2w = strcat(pathName, '\', std_fname);

%%%%%%%%%%%%%%%%%%%%%%%%%%%%%%%%%%%%%%%%%%%%%%%%%%%%%%%%%%%%%%%%%%%%%%%%
%%%%%%%%%%%%%%

vsupply_f2r = strcat(pathName, '\', 'raw_ch1_vsupply_gaussian.csv');
vsupply_data = csvread(vsupply_f2r);

for index = 1 : length(IphList)
    Iph = IphList(index);

    vm_f2r = fullfile(pathName, fileList_vm(index).name);
    vm_data = csvread(vm_f2r);

    isupply = (vsupply_data - vm_data)/Ri;

    ISUPPLY = fft(isupply)/Len;

    VSUPPLY = fft(vsupply_data)/Len;

    for loop = 1 : NumLoop
        I_BLA(loop,:) = ISUPPLY(loop,ptFreq+1)./VSUPPLY(loop,ptFreq+1);
    end

    I_BLA_Mean(index,:) = mean(I_BLA,1);
    I_BLA_Std(index,:) = std(I_BLA,0,1);

    format short;
    legendInfo{index} = ['Iph = ' sprintf('%0.3e',Iph)];

    m = {'+','o','*','.','x','s','d','^','v','>','<','p','h'};
    set_marker_order = @() set(gca(), ...
    'LineStyleOrder',m, 'ColorOrder',[0 0 0], ...
    'NextPlot','replacechildren');

    figure(1);
    stem(Freq(ptFreq+1),abs(I_BLA_Mean)');
    xlabel('Frequency(Hz)');
    ylabel('Mean of FRFs');
    title('Mean of FRFs vs Frequency');
    n=get(gca,'Ytick');
    set(gca,'Yticklabel',sprintf('%0.5e |',n));
    legend(legendInfo,'location','NorthEastOutside');
    grid on;

    figure(2);
    stem(Freq(ptFreq+1),abs(I_BLA_Std)');
    xlabel('Frequency(Hz)');
    ylabel('Standard Deviation of FRFs');
    title('Standard Deviation of FRFs vs Frequency');
    n=get(gca,'Ytick');
    set(gca,'Yticklabel',sprintf('%0.5e |',n));
    legend(legendInfo,'location','NorthEastOutside');
    grid on;

    drawnow;
end

m_I_BLA_Mean = [Freq(ptFreq+1);abs(I_BLA_Mean)]';
m_I_BLA_Std = [Freq(ptFreq+1);abs(I_BLA_Std)]';

csvwrite(mean_f2w, m_I_BLA_Mean);
csvwrite(std_f2w, m_I_BLA_Std);
```

G.3 Formatting of FRF Mean Plots

Filename: .\Monash\Research\Test\Simulation\Matlab\mean_multicolPlot_ma_rev.m

```
clear all;
close all;
clc;

%pathName = 'C:\Temp\Labview\Labview Data Files 1k';
%pathName = 'C:\Temp\Labview\Labview Data Files 10k';
pathName = 'C:\Temp\Labview\Labview Data Files 100k';

%mean_fname    = 'mean_frf_msine_1rc_1k.txt';
%mean_fname    = 'mean_frf_msine_1rc_10k.txt';
%mean_fname    = 'mean_frf_msine_1rc_100k.txt';

%mean_fname    = 'mean_frf_gaussian_1rc_1k.txt';
%mean_fname    = 'mean_frf_gaussian_1rc_10k.txt';
mean_fname    = 'mean_frf_gaussian_1rc_100k.txt';

mean_f2r = strcat(pathName, '\', mean_fname);

[labels,freq,m] = readColData(mean_f2r,10,0);

figure(1);
set(gcf,'color','w');
plot(freq,m(:,1),'ro',freq,m(:,2),'bx',freq,m(:,3),'k+',freq,m(:,4),'rs',freq,m(:,5),'bd',freq,m(:,6),'kv',freq,m(:,7),'r^',freq,m(:,8),'b<',freq,
m(:,9),'kp');
xlim([10 2010]);

xtick_label = csvread('multisine_freq.csv');
set(gca, 'xtick', xtick_label', 'box', 'off', 'FontSize', 12, 'FontWeight', 'bold', 'YMinorTick', 'on');

xlab = strcat(labels(1,:),' (Hz)');
xlabel(xlab, 'fontsize', 18, 'FontWeight', 'bold');                    % add axis labels and plot title
ylabel('Mean of FRFs', 'fontsize', 18, 'FontWeight', 'bold');
title('Mean of FRFs vs Frequency', 'fontsize', 24, 'FontWeight', 'bold');

leg1 = '12.5 W/m^2';
leg2 = '18.8 W/m^2';
leg3 = '25.0 W/m^2';
leg4 = '31.2 W/m^2';
leg5 = '37.4 W/m^2';
leg6 = '43.6 W/m^2';
leg7 = '49.9 W/m^2';
leg8 = '56.1 W/m^2';
leg9 = '62.3 W/m^2';

legend(leg1, leg2, leg3, leg4, leg5, leg6, leg7, leg8, leg9, 'fontsize', 18, 'FontWeight', 'bold', 'location', 'NorthEastOutside');
```

G.4 Formatting of FRF Standard Deviation Plots

Filename: .\Monash\Research\Test\Simulation\Matlab\std_multicolPlot_ma_rev.m

```
clear all;
close all;
clc;

%pathName = 'C:\Temp\Labview\Labview Data Files 1k';
%pathName = 'C:\Temp\Labview\Labview Data Files 10k';
pathName = 'C:\Temp\Labview\Labview Data Files 100k';

%std_fname    = 'std_frf_msine_1rc_1k.txt';
%std_fname    = 'std_frf_msine_1rc_10k.txt';
%std_fname    = 'std_frf_msine_1rc_100k.txt';

%std_fname    = 'std_frf_gaussian_1rc_1k.txt';
%std_fname    = 'std_frf_gaussian_1rc_10k.txt';
std_fname    = 'std_frf_gaussian_1rc_100k.txt';

std_f2r = strcat(pathName, '\', std_fname);
```

```
[labels,freq,m] = readColData(std_f2r,10,0);

figure(2);
set(gcf,'color','w');
plot(freq,m(:,1),'ro',freq,m(:,2),'bx',freq,m(:,3),'k+',freq,m(:,4),'rs',freq,m(:,5),'bd',freq,m(:,6),'kv',freq,m(:,7),'r^',freq,m(:,8),'b<',freq,
m(:,9),'kp');
xlim([10 2010]);

xtick_label = csvread('multisine_freq.csv');
set(gca, 'xtick', xtick_label', 'box', 'off', 'FontSize', 12, 'FontWeight', 'bold', 'YMinorTick', 'on');

xlab = strcat(labels(1,:),' (Hz)');
xlabel(xlab, 'fontsize', 18, 'FontWeight', 'bold');                    % add axis labels and plot title
ylabel('Standard Deviation of FRFs', 'fontsize', 18, 'FontWeight', 'bold');
title('Standard Deviation of FRFs vs Frequency', 'fontsize', 24, 'FontWeight', 'bold');

leg1 = '12.5 W/m^2';
leg2 = '18.8 W/m^2';
leg3 = '25.0 W/m^2';
leg4 = '31.2 W/m^2';
leg5 = '37.4 W/m^2';
leg6 = '43.6 W/m^2';
leg7 = '49.9 W/m^2';
leg8 = '56.1 W/m^2';
leg9 = '62.3 W/m^2';

legend(leg1, leg2, leg3, leg4, leg5, leg6, leg7, leg8, leg9, 'fontsize', 18, 'FontWeight', 'bold', 'location','NorthEastOutside');
```

APPENDIX H SIMULINK MODEL / MATLAB SCRIPTS FOR DATA ANALYSIS

H.1 Matlab Script for Frequency Plots of Discrete Low Pass Filters

Filename: .\Monash\Research\Test\Simulation\Matlab\discrete_filter_comparison.m

```
clear all;
close all;
clc;

% Moving Averager
L=1000;
bm=ones(1,L)/L;
am=[1];
[hm, wm] = freqz(bm, am);

f = 2.01e3;  % Cut-off frequency
fs = 40.96e3;  % Sampling frequency

% Butterworth - 5th order
[bb, ab] = butter(5, 2*(f/fs));
[hb, wb] = freqz(bb, ab);

% Chebyshev Type 1 - 5th order, 30dB passband ripple
[bc1, ac1] = cheby1(5, 30, 2*(f/fs));
[hc1, wc1] = freqz(bc1, ac1);

% Chebyshev Type 2 - 5th order, 30dB stopband attenuation
[bc2, ac2] = cheby2(5, 30, 2*(f/fs));
[hc2, wc2] = freqz(bc2, ac2);

% Elliptic - 5th order, 30dB passband ripple, 35dB stopband attenuation
[be, ae] = ellip(5, 30, 35, 2*(f/fs));
[he, we] = freqz(be, ae);

% Plotting
figure(1)
set(gcf, 'color', 'w')
plot(fs*wm/(1e3*2*pi), mag2db(abs(hm)), 'ro')
hold on
plot(fs*wb/(1e3*2*pi), mag2db(abs(hb)), 'kx')
hold on
plot(fs*wc1/(1e3*2*pi), mag2db(abs(hc1)), 'b+')
hold on
plot(fs*wc2/(1e3*2*pi), mag2db(abs(hc2)), 'ks')
hold on
plot(fs*we/(1e3*2*pi), mag2db(abs(he)), 'md')
axis([0 4 -90 0])
grid
title('Comparison of Different Types of Low Pass Filter', 'fontsize', 24, 'FontWeight', 'bold')
xlabel('Frequency (kHz)', 'fontsize', 18, 'FontWeight', 'bold')
ylabel('Attenuation (dB)', 'fontsize', 18, 'FontWeight', 'bold')
set(gca, 'box', 'off',  'fontsize', 12, 'FontWeight', 'bold', 'YMinorTick', 'on', 'XMinorTick', 'on')
legend('Moving Averager (1000point)', 'Butterworth', 'Chebyshev Type 1', 'Chebyshev Type 2', 'Elliptic')
```

H.2 Matlab Script for Power Spectral Density Plot

Filename:

.\Monash\Research\Test\Simulation\Matlab\Circuit Analysis\fft_rc_photodetector.m

```
close all;
clear all;
clc;

% This is a good example on power spectral analysis of signal
cstring='rgbcm'; % color string
```

```
fs = 40960;  % Sampling frequency

load('Vout_20ma_multisine_1k_1u.mat')
%load('Vout_20ma_multisine_10k_1u.mat')
%load('Vout_20ma_multisine_100k_1u.mat')
%load('Vout_20ma_multisine_1k_1n.mat')

%load('Vout_20ma_gaussian_1k_1u.mat')
%load('Vout_20ma_gaussian_10k_1u.mat')
%load('Vout_20ma_gaussian_100k_1u.mat')
%load('Vout_20ma_gaussian_1k_1n.mat')

vout = Vout.signals.values(:,1);

% Windowing
nfft_vout = length(vout)-1;
w1 = hanning(length(vout), 'periodic');
w_vout = w1.*vout;
V = fft(w_vout, nfft_vout)/nfft_vout;

load('Iout_20ma_multisine_1k_1u.mat')
%load('Iout_20ma_multisine_10k_1u.mat')
%load('Iout_20ma_multisine_100k_1u.mat')
%load('Iout_20ma_multisine_1k_1n.mat')

%load('Iout_20ma_gaussian_1k_1u.mat')
%load('Iout_20ma_gaussian_10k_1u.mat')
%load('Iout_20ma_gaussian_100k_1u.mat')
%load('Iout_20ma_gaussian_1k_1n.mat')

imod = Iout.signals.values(:,1);

% Windowing
nfft_imod = length(imod)-1;
w2 = hanning(length(imod), 'periodic');
w_imod = w2.*imod;
I = fft(w_imod, nfft_imod)/nfft_imod;

Y = V./I;

% Compute power spectral density
Pyy = Y.*conj(Y);

nfft = length(Y)-1;

% Calculate the number of unique points
NumUniquePts = ceil(nfft/2);

f = (0:NumUniquePts-1)*fs/nfft;
psd = 10*log10(2*Pyy(1:end/2));
mag = 20*log10(2*Y_mag(1:end/2));

figure(1)
set(gcf,'color','w');
semilogx(f, psd)
title('Power Spectral Density', 'fontsize', 24, 'FontWeight', 'bold')
xlabel('Frequency (Hz)', 'fontsize', 18, 'FontWeight', 'bold')
ylabel('PSD (db)', 'fontsize', 18, 'FontWeight', 'bold')
set(gca, 'box', 'off', 'FontSize', 12, 'FontWeight', 'bold', 'YMinorTick', 'on')
grid on
```

H.3 Script for Irradiance versus Short-Circuit Current Plot

Filename:

.\Monash\Research\Test\Simulation\Matlab\Circuit Analysis\interpolation_irradiance.m

```
clear all;
close all;
clc;
```

```
load mpvc_irradiance;

iph = 2 : 0.05 : 7;

iph_mpvc_irradiance = mpvc_irradiance(:,1);
irrad_mpvc_irradiance = mpvc_irradiance(:,2);

int_irrad_mpvc_irradiance = interp1(iph_mpvc_irradiance, irrad_mpvc_irradiance, iph, 'spline');

int_irrad_mpvc_2ma = interp1(iph_mpvc_irradiance, irrad_mpvc_irradiance, 2, 'spline');
int_irrad_mpvc_3ma = interp1(iph_mpvc_irradiance, irrad_mpvc_irradiance, 3, 'spline');
int_irrad_mpvc_4ma = interp1(iph_mpvc_irradiance, irrad_mpvc_irradiance, 4, 'spline');
int_irrad_mpvc_5ma = interp1(iph_mpvc_irradiance, irrad_mpvc_irradiance, 5, 'spline');
int_irrad_mpvc_6ma = interp1(iph_mpvc_irradiance, irrad_mpvc_irradiance, 6, 'spline');
int_irrad_mpvc_7ma = interp1(iph_mpvc_irradiance, irrad_mpvc_irradiance, 7, 'spline');
int_irrad_mpvc_8ma = interp1(iph_mpvc_irradiance, irrad_mpvc_irradiance, 8, 'spline');
int_irrad_mpvc_9ma = interp1(iph_mpvc_irradiance, irrad_mpvc_irradiance, 9, 'spline');
int_irrad_mpvc_10ma = interp1(iph_mpvc_irradiance, irrad_mpvc_irradiance, 10, 'spline');

% Polynomial fit
p1 = polyfit(iph, int_irrad_mpvc_irradiance, 1);
pfit1 = polyval(p1, iph);

figure(1)
set(gcf,'color','w')
plot(iph, int_irrad_mpvc_irradiance, 'ro', iph, pfit1, 'k-')
set(gca, 'box', 'off', 'FontSize', 12, 'FontWeight', 'bold', 'XMinorTick', 'on', 'YMinorTick', 'on')
title('Irradiance versus Short-circuit Photocurrent (mA)', 'fontsize', 24, 'FontWeight', 'bold')
xlabel('Short-Circuit Current, Iph (mA)', 'fontsize', 18, 'FontWeight', 'bold')
ylabel('Irradiance, Ir (W/m^2)', 'fontsize', 18, 'FontWeight', 'bold')
ylim = get(gca, 'YLim');
xlim = get(gca, 'XLim');
text((xlim(1) + (xlim(2)-xlim(1))/8), (ylim(1) + (ylim(2) - ylim(1))*3/5), sprintf('Ir = %0.4f*Iph + %0.4f W/m^2', p1(1), p1(2)),
'fontsize', 18, 'FontWeight', 'bold')

load mpd_irradiance;

iph2 = 40 : 0.05 : 100;

iph_mpd_irradiance = mpd_irradiance(:,1);
irrad_mpd_irradiance = mpd_irradiance(:,2);

int_irrad_mpd_irradiance = interp1(iph_mpd_irradiance, irrad_mpd_irradiance, iph2, 'spline');

% Polynomial fit
p2 = polyfit(iph2, int_irrad_mpd_irradiance, 1);
pfit2 = polyval(p2, iph2);

figure(2)
set(gcf,'color','w')
plot(iph2, int_irrad_mpd_irradiance, 'ro', iph2, pfit2, 'k-')
set(gca, 'box', 'off', 'FontSize', 12, 'FontWeight', 'bold', 'XMinorTick', 'on', 'YMinorTick', 'on')
title('Irradiance versus Short-circuit Photocurrent (\muA)', 'fontsize', 24, 'FontWeight', 'bold')
xlabel('Short-Circuit Current, Iph (\muA)', 'fontsize', 18, 'FontWeight', 'bold')
ylabel('Irradiance, Ir (W/m^2)', 'fontsize', 18, 'FontWeight', 'bold')
ylim2 = get(gca, 'YLim');
xlim2 = get(gca, 'XLim');
text((xlim2(1) + (xlim2(2)-xlim2(1))/8), (ylim2(1) + (ylim2(2) - ylim2(1))*3/5), sprintf('Ir = %0.4f*Iph + %0.4f W/m^2', p2(1), p2(2)),
'fontsize', 18, 'FontWeight', 'bold')
```

H.4 Script for I-V Interpolation Plot

Filename: .\Monash\Research\Test\Simulation\Matlab\Circuit Analysis\interpolation_iv.m

```
clear all;
close all;
clc;

load mpvc_iv_2ma;
load mpvc_iv_5ma;
load mpvc_iv_10ma;
```

```
vi = -5 : 0.001 : 2;

v_mpvc_2ma = mpvc_iv_2ma(:,1);
i_mpvc_2ma = mpvc_iv_2ma(:,2);

v_mpvc_5ma = mpvc_iv_5ma(:,1);
i_mpvc_5ma = mpvc_iv_5ma(:,2);

v_mpvc_10ma = mpvc_iv_10ma(:,1);
i_mpvc_10ma = mpvc_iv_10ma(:,2);

ii_mpvc_2ma = interp1(v_mpvc_2ma, i_mpvc_2ma, vi, 'spline');
ii_mpvc_5ma = interp1(v_mpvc_5ma, i_mpvc_5ma, vi, 'spline');
ii_mpvc_10ma = interp1(v_mpvc_10ma, i_mpvc_10ma, vi, 'spline');

figure(1)
set(gcf,'color','w')
plot(vi, ii_mpvc_2ma, 'ro', vi, ii_mpvc_5ma, 'bx', vi, ii_mpvc_10ma, 'ks')
set(gca, 'box', 'off', 'FontSize', 12, 'FontWeight', 'bold', 'XMinorTick', 'on', 'YMinorTick', 'on')
title('I-V Curve of Miniature Inorganic Photovoltaic Cell', 'fontsize', 24, 'FontWeight', 'bold')
xlabel('Bias Voltage (V)', 'fontsize', 18, 'FontWeight', 'bold')
ylabel('Photocurrent (mA)', 'fontsize', 18, 'FontWeight', 'bold')
%legend('2 mA', '5 mA', '10 mA', 'location', 'NorthEastOutside');
legend('12.5 W/m^2', '31.2 W/m^2', '62.3 W/m^2', 'location', 'NorthEastOutside');
```

H.5 Script for Regression Analysis

Filename: .\Monash\Research\Test\Simulation\Matlab\linear_regression_analysis_k_new.m

```
clear all;
close all;
clc;

% Multisine Excitation
%pathName = 'C:\Temp\Labview\Labview Data Files 1k';
%pathName = 'C:\Temp\Labview\Data Files MPVC_2';

%reg_fname    = 'reg_msine_1rc_1k_330hz.csv';
%reg_fname    = 'reg_msine_mpvc2_1370hz.csv';

% Gaussian Noise Excitation
%pathName = 'C:\Temp\Labview\Labview Data Files 1k';
pathName = 'C:\Temp\Labview\Labview Data Files 10k (opv2)';
%pathName = 'C:\Temp\Labview\Data Files MPVC_G_1';

%reg_fname    = 'reg_gaussian_1rc_1k_730hz.csv';
reg_fname    = 'reg_gaussian_1rc_10k_opv_2010hz.csv';
%reg_fname    = 'reg_gaussian_mpvc_490hz.csv';

reg_f2r = strcat(pathName, '\', reg_fname);
reg_data = csvread(reg_f2r);

% Read in data
i = reg_data(:,1);
s = reg_data(:,2);

% Polynomial fit
p1 = polyfit(s, i, 1);
pfit1 = polyval(p1, s);

p2 = polyfit(s, i, 2);
pfit2 = polyval(p2, s);

p3 = polyfit(s, i, 3);
pfit3 = polyval(p3, s);

modelfun = @(p,x) p(1)*(exp(p(2)*x));
[coeff, R, ~, ~, MSE] = nlinfit(s, i, modelfun, [0,0.1])
pfit4 = coeff(1)*(exp(coeff(2)*s)-1);

n = length(i);  % Number of observations
d1 = length(p1); % Degree of polynomial; d = 1 for linear fit; d = 2 for quadratic fit; d = 3 for cubic fit
```

```
d2 = length(p2);
d3 = length(p3);

SStotal = (n - 1)*var(i);

yresid1 = i - pfit1;
SSresid1 = sum(yresid1.^2);
rsq1 = 1 - SSresid1/SStotal;
rsq1_adj = 1 - (SSresid1/SStotal)*(n - 1)/(n - d1);

yresid2 = i - pfit2;
SSresid2 = sum(yresid2.^2);
rsq2 = 1 - SSresid2/SStotal;
rsq2_adj = 1 - (SSresid2/SStotal)*(n - 1)/(n - d2);

yresid3 = i - pfit3;
SSresid3 = sum(yresid3.^2);
rsq3 = 1 - SSresid3/SStotal;
rsq3_adj = 1 - (SSresid3/SStotal)*(n - 1)/(n - d3);

yresid4 = i - pfit4;
SSresid4 = sum(yresid4.^2);
rsq4 = 1 - SSresid4/SStotal;

figure(1)
set(gcf,'color','w')
subplot(2, 2, 1), plot(s, i, 'ko'), hold on, plot(s, pfit1, 'k--'),grid off, title('1st Order Fit', 'fontsize', 24, 'FontWeight', 'bold')
set(gca, 'box', 'off', 'FontSize', 12, 'FontWeight', 'bold', 'YMinorTick', 'on')
xlabel('Standard Deviation of FRFs', 'fontsize', 18, 'FontWeight', 'bold')
%ylabel('Photocurrent (mA)', 'fontsize', 18, 'FontWeight', 'bold')
ylabel('Photocurrent (\muA)', 'fontsize', 18, 'FontWeight', 'bold')
ylim = get(gca, 'YLim');
xlim = get(gca, 'XLim');
%text((xlim(1) + (xlim(2)-xlim(1))*1/3), (ylim(1) + (ylim(2) - ylim(1))*4/5), sprintf('I = %0.2f\\sigma + %0.2f mA', p1(1), p1(2)),
'fontsize', 16, 'FontWeight', 'bold')
text((xlim(1) + (xlim(2)-xlim(1))*1/3), (ylim(1) + (ylim(2) - ylim(1))*4/5), sprintf('I = %0.2f\\sigma + %0.2f \\muA', p1(1), p1(2)),
'fontsize', 16, 'FontWeight', 'bold')

subplot(2, 2, 2), plot(s, i, 'ko'), hold on, plot(s, pfit2, 'k--'), grid off, title('2nd Order Fit', 'fontsize', 24, 'FontWeight', 'bold')
set(gca, 'box', 'off', 'FontSize', 12, 'FontWeight', 'bold', 'YMinorTick', 'on')
xlabel('Standard Deviation of FRFs', 'fontsize', 18, 'FontWeight', 'bold')
%ylabel('Photocurrent (mA)', 'fontsize', 18, 'FontWeight', 'bold')
ylabel('Photocurrent (\muA)', 'fontsize', 18, 'FontWeight', 'bold')
ylim = get(gca, 'YLim');
xlim = get(gca, 'XLim');
%text((xlim(1) + (xlim(2)-xlim(1))*1/3), (ylim(1) + (ylim(2) - ylim(1))*4/5), sprintf('I = %0.2f\\sigma^2 + %0.2f\\sigma + %0.2f mA',
p2(1), p2(2), p2(3)), 'fontsize', 16, 'FontWeight', 'bold')
text((xlim(1) + (xlim(2)-xlim(1))*1/4), (ylim(1) + (ylim(2) - ylim(1))*4/5), sprintf('I = %0.2f\\sigma^2 + %0.2f\\sigma + %0.2f \\muA',
p2(1), p2(2), p2(3)), 'fontsize', 16, 'FontWeight', 'bold')

subplot(2, 2, 3), plot(s, i, 'ko'), hold on, plot(s, pfit3, 'k--'), grid off, title('3rd Order Fit', 'fontsize', 24, 'FontWeight', 'bold')
set(gca, 'box', 'off', 'FontSize', 12, 'FontWeight', 'bold', 'YMinorTick', 'on')
xlabel('Standard Deviation of FRFs', 'fontsize', 18, 'FontWeight', 'bold')
%ylabel('Photocurrent (mA)', 'fontsize', 18, 'FontWeight', 'bold')
ylabel('Photocurrent (\muA)', 'fontsize', 18, 'FontWeight', 'bold')
ylim = get(gca, 'YLim');
xlim = get(gca, 'XLim');
%text((xlim(1) + (xlim(2)-xlim(1))*1/3), (ylim(1) + (ylim(2) - ylim(1))*1/6), sprintf('I = %0.2f\\sigma^3 + %0.2f\\sigma^2 +
%0.2f\\sigma + %0.2f mA', p3(1), p3(2), p3(3), p3(4)), 'fontsize', 16, 'FontWeight', 'bold')
text((xlim(1) + (xlim(2)-xlim(1))*1/3), (ylim(1) + (ylim(2) - ylim(1))*1/5), sprintf('I = %0.2f\\sigma^3 + %0.2f\\sigma^2 +
%0.2f\\sigma + %0.2f \\muA', p3(1), p3(2), p3(3), p3(4)), 'fontsize', 16, 'FontWeight', 'bold')

subplot(2, 2, 4), plot(s, i, 'ko'), hold on, plot(s, pfit4, 'k--'), grid off, title('Logarithmic Fit', 'fontsize', 24, 'FontWeight', 'bold')
set(gca, 'box', 'off', 'FontSize', 12, 'FontWeight', 'bold', 'YMinorTick', 'on')
xlabel('Standard Deviation of FRFs', 'fontsize', 18, 'FontWeight', 'bold')
%ylabel('Photocurrent (mA)', 'fontsize', 18, 'FontWeight', 'bold')
ylabel('Photocurrent (\muA)', 'fontsize', 18, 'FontWeight', 'bold')
ylim = get(gca, 'YLim')
xlim = get(gca, 'XLim')
%text((xlim(1) + (xlim(2)-xlim(1))*1/3), (ylim(1) + (ylim(2) - ylim(1))*4/5), sprintf('I = %0.2f(e^{%0.2f\\sigma}-1) mA', coeff(1),
coeff(2)), 'fontsize', 16, 'FontWeight', 'bold')
text((xlim(1) + (xlim(2)-xlim(1))*1/3), (ylim(1) + (ylim(2) - ylim(1))*4/5), sprintf('I = %0.2f(e^{%0.2f\\sigma}-1) \\muA', coeff(1),
coeff(2)), 'fontsize', 16, 'FontWeight', 'bold')

figure(2)
```

```
set(gcf,'color','w')
subplot(2, 2, 1), plot(s, yresid1, 'k*'), grid on, title('1st Order Residuals', 'fontsize', 24, 'FontWeight', 'bold')
set(gca, 'box', 'off', 'FontSize', 12, 'FontWeight', 'bold', 'YMinorTick', 'on')
xlabel('Standard Deviation of FRFs', 'fontsize', 18, 'FontWeight', 'bold')
ylabel('Residuals', 'fontsize', 18, 'FontWeight', 'bold')

subplot(2, 2, 2), plot(s, yresid2, 'k*'), grid on, title('2nd Order Residuals', 'fontsize', 24, 'FontWeight', 'bold')
set(gca, 'box', 'off', 'FontSize', 12, 'FontWeight', 'bold', 'YMinorTick', 'on')
xlabel('Standard Deviation of FRFs', 'fontsize', 18, 'FontWeight', 'bold')
ylabel('Residuals', 'fontsize', 18, 'FontWeight', 'bold')

subplot(2, 2, 3), plot(s, yresid3, 'k*'), grid on, title('3rd Order Residuals', 'fontsize', 24, 'FontWeight', 'bold')
set(gca, 'box', 'off', 'FontSize', 12, 'FontWeight', 'bold', 'YMinorTick', 'on')
xlabel('Standard Deviation of FRFs', 'fontsize', 18, 'FontWeight', 'bold')
ylabel('Residuals', 'fontsize', 18, 'FontWeight', 'bold')

subplot(2, 2, 4), plot(s, yresid4, 'k*'), grid on, title('Logarithmic Residuals', 'fontsize', 24, 'FontWeight', 'bold')
set(gca, 'box', 'off', 'FontSize', 12, 'FontWeight', 'bold', 'YMinorTick', 'on')
xlabel('Standard Deviation of FRFs', 'fontsize', 18, 'FontWeight', 'bold')
ylabel('Residuals', 'fontsize', 18, 'FontWeight', 'bold')
```

H.6 Script for Correlation Test

Filename: .\Monash\Research\Test\Simulation\Matlab\correlation_analysis.m

```
clear all;
close all;
clc;

% Multisine Excitation
pathName1 = 'C:\Temp\Labview\Labview Data Files 1k';
reg_fname1    = 'reg_msine_1rc_1k_330hz.csv';

% Gaussian Noise Excitation
pathName2 = 'C:\Temp\Labview\Labview Data Files 1k';
pathName3 = 'C:\Temp\Labview\Labview Data Files 10k (opv2)';

reg_fname2    = 'reg_gaussian_1rc_1k_730hz.csv';
reg_fname3    = 'reg_gaussian_1rc_10k_opv_2010hz.csv';

reg_f2r1 = strcat(pathName1, '\', reg_fname1);
reg_data1 = csvread(reg_f2r1);

reg_f2r2 = strcat(pathName2, '\', reg_fname2);
reg_data2 = csvread(reg_f2r2);

reg_f2r3 = strcat(pathName3, '\', reg_fname3);
reg_data3 = csvread(reg_f2r3);

% Read in data
i1 = reg_data1(:,1);  % Multisine MPV
s1 = reg_data1(:,2);  % Multisine MPV

i2 = reg_data2(:,1);  % Gaussian MPV
s2 = reg_data2(:,2);  % Gaussian MPV

i3 = reg_data3(:,1);  % Gaussian OPV
s3 = reg_data3(:,2);  % Gaussian OPV

% Pearson's Correlation Test
[rho1, pval1] = corrcoef(reg_data1);  % Multisine MPV
[rho2, pval2] = corrcoef(reg_data2);  % Gaussian MPV
[rho3, pval3] = corrcoef(reg_data3);  % Gaussian OPV

skew1 = skewness(reg_data1);  % Multisine MPV
skew2 = skewness(reg_data2);  % Gaussian MPV
skew3 = skewness(reg_data3);  % Gaussian OPV

kurt1 = kurtosis(reg_data1);  % Multisine MPV
kurt2 = kurtosis(reg_data2);  % Gaussian MPV
kurt3 = kurtosis(reg_data3);  % Gaussian OPV
```

```
% Kendall's Correlation Test
[rho1k, pval1k] = corr(i1, s1, 'type', 'Kendall');  % Multisine MPV - Calculating Kendall's tau
[rho2k, pval2k] = corr(i2, s2, 'type', 'Kendall');  % Gaussian MPV - Calculating Kendall's tau
[rho3k, pval3k] = corr(i3, s3, 'type', 'Kendall');  % Gaussian OPV - Calculating Kendall's tau
```